Magnetic force microscopy
application to magnetic nanostructures

de Loos, B.

Award date:
2006

TU/e technische universiteit eindhoven

Eindhoven University of Technology
Department of Applied Physics
Group Physics of Nanostructures

Magnetic Force Microscopy: application to magnetic nanostructures

B. de Loos

June 2006

Report of a graduation project, carried out at the Eindhoven University of Technology in the group Physics of Nanostructures.

Supervisors:	dr. O. Kurnosikov
	prof. dr. ir. H.J.M. Swagten
Group leader:	prof. dr. B. Koopmans

Abstract

Magnetic force microscopy (MFM) is a tool to investigate the local magnetization of magnetic samples, especially for laterally confined structures in the field of nanomagnetism and spintronics. In this thesis an additional stage is developed for the Solver P47H scanning force microscope, to perform MFM measurements in the presence of an applied magnetic field. Apart from that, experiments have been performed on magnetic nanostructured devices to image magnetic properties on a sub-micrometer scale.

For testing of the feasibility of magnetic read only memory (MROM), a magnetic data carrier is measured. The data carrier consist of structured bits of 5×1 μm, on a substrate coated with a continuous magnetic 200 nm CoFe film. A small, but detectable magnetic field is measured in the remanent state of the bits. A large scan area reveals an oscillating signal corresponding to the pitch of the bits. In the presence of a magnetic field, the magnetization of individual bits is qualitatively determined. The switch field of individual bits is found to be in the range of 0–10 mT. This is in agreement with the measurement of the magnetization with a SQUID magnetometer of the full layer.

In magnetic random access memory (MRAM), a magnetic tunnel junction is used to store binary data. Structured magnetic multilayers used for the development of MRAM, with a lateral size of 1×1 μm, are investigated by MFM. At remanence, the magnetization of the individual bits has a random orientation, and the magnetic state of the bits is easily influenced by the stray field of the magnetic tip. At a non-zero applied field (30 mT) the structures are found to be almost uniformly in-plane magnetized.

Spin injection into semiconductors needs control of the magnetization direction of two ferromagnetic (CoFe) strip-like electrodes deposited on top of a semiconductor structure. With MFM, the magnetic switch field of structured magnetic strips is determined as a function of the width of the strips, and is typically in the range of 10–20 mT. Whereas single domain models are not able to correctly describe these fields, a quantitative agreement is found with micromagnetic simulations (OOMMF).

Contents

Chapter 1

General Introduction

The goal of this thesis is to demonstrate the application of magnetic force microscopy (MFM) imaging on magnetic nanostructures, and the implementation of an external magnetic field.

The interest in nanotechnology is motivated by the future prospects of novel applications for society. At present, there is increasing research interest in the field of "magneto electronics", where nanostructures are integrated in novel devices such as magnetic random access memories (MRAM). For the study of magnetic nanodevices, imaging of magnetic domains is indispensable in most cases and should be combined with other techniques for characterizations of structure, morphology, and magnetic properties.

Particularly significant for the ability to characterize nanostructures was the invention of scanning probe microscopy. Atomic force microscopes offer depth resolution and can be used as mechanical microprobes. Scanning tunneling microscopes can even provide imaging and manipulation at the atomic scale. Magnetic force microscopes open new possibilities to explore the ordering of magnetic structures on a microscopic level.

In this chapter a general introduction is presented. First, section 1.1 presents an introduction to the importance of miniaturization. Some technologically important nanostructures are treated in section 1.2. Next, in section 1.3 magnetic characterization techniques used for investigations of individual nanostructures are discussed. In section 1.4, the importance of MFM as a characterization technique for the development of magnetic nanostructures is treated. Finally, in section 1.5 the motivation and outlook for this thesis are presented.

1.1 Miniaturization

There are may reasons why the quest for smaller objects, machines and computers continues. Miniaturization means better use of materials, less waist and lower power consumption and thus lower costs, but it can also lead to new application area's and even to new material properties. Fig. 1.1 gives an overview of the scale of miniaturization.

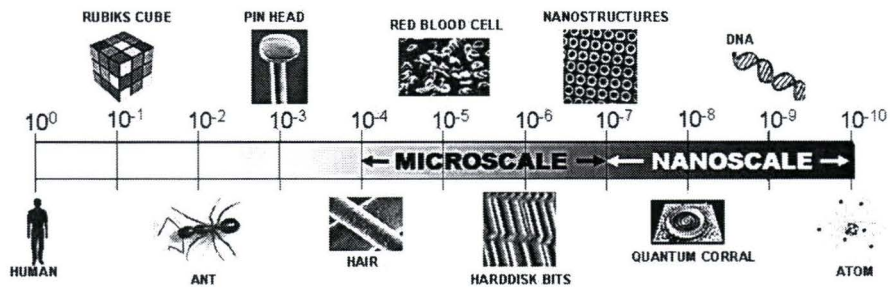

Figure 1.1: *Miniaturization: From the length of men to the size of atoms.*

Macroscopic material properties can change dramatically by the down scaling of size. Examples of such changes are: change in conductance in metals, change in magnetic coercivity, and change in mechanical properties. In 1959 Richard Feynman gave some remarkable statements in his talk titled: *"There is plenty of room at the bottom; an invitation to enter a new field of physics"*[1]. He stated: *"The magnetic properties on a very small scale are not the same as on a large scale; there is the "domain" problem involved. A big magnet made of millions of domains can only be made on a small scale with one domain"*. This relates to the problems that arise by miniaturization of magnetic devices, magnetic domains can change the behavior of the macroscopic properties. the magnetic properties may change as the dimensions are scaled down to some magnetic characteristic length scale. He also mentioned that the analysis of physical, chemical and biological structures is made easy when *"all one would have to do would be to look at it and see where the atoms are"*. Thus imaging techniques make investigation of, for example magnetic domain structure, relative simple if the domains can be seen.

[1]The transcript of the talk Richard Feynman gave on in 1959 at the annual meeting of the American Physical Society at the California Institute of Technology (Caltech) was first published in the February 1960 issue of Caltech's Engineering and Science, which owns the copyright. It has been made available on the web at http://www.zyvex.com/nanotech/feynman.html

1.2 Technology overview

The ongoing miniaturization in layered metallic thin films of nanometer thickness has led to the discovery in 1986 of antiferromagnetic exchange coupling in magnetic multilayer structures [1, 2], and the discovery of the giant magnetoresistance (GMR) effect [3, 4, 5] in 1988. Since then, the interest in nanostructured magnetic materials has increased enormously.

A GMR device consists of two ferromagnetic layers, separated by an thin non-magnetic layer. The GMR effect is the change in resistance of a device when the magnetization of the layers is switched from a parallel to an anti-parallel alignment (see Fig. 1.2). The resistance is minimal when the two magnetic layers have parallel magnetization, and if the magnetization is anti-parallel the resistance is maximal.

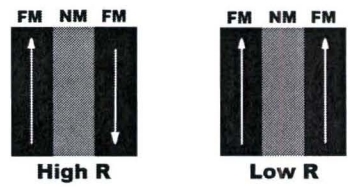

Figure 1.2: *A GMR device consists of a non-magnetic layer (NM), sandwiched between two ferromagnetic layers (FM). The resistance (R) of a GMR device depends on the relative magnetization (indicated with the arrows) of the ferromagnetic layers.*

Magnetic tunnel junctions (MTJ's) [6, 7] are another important development, discovered in 1995. A MTJ consists of two ferromagnetic layers separated by a thin insulator. When a bias voltage is applied over the MTJ, a tunnel current flows through the insulator. This current is spin dependent. This means the current is dependent on the relative orientation of the magnetization of the ferromagnetic layers, resulting in a (high) low resistance when the layers are (anti)parallel aligned as can be seen in Fig. 1.3. This is known as the tunnel magnetoresistance (TMR) effect. The large change in resistance in GMR and MTJ structures has increased the ability to use such structures for applications as magnetic sensors [8]. GMR structures have already found their way into commercially available read-heads for hard disks [9].

Especially MTJ's are extremely attractive for application as magnetic random access memory (MRAM) [10, 11]. A typical MRAM cell consists of a MTJ sandwiched between two electrodes, the so called "word" and "bit" lines. In Fig. 1.4 an array of MRAM cells can be seen. Each MTJ can

Figure 1.3: *Schematic overview of a magnetic tunnel junction (MTJ). A thin insulator is sandwiched between two ferromagnetic (FM) layers which are connected to two electrodes. The arrows in the (FM) layers indicate the magnetization direction. The tunnel current of a MTJ-device is dependent on the orientation of the magnetization. When applying a bias voltage across the structure, an anti-parallel orientation (left) leads to a high resistive state, and thus a low current (I_{AP}) while a parallel orientation (right) results in a low resistance, and high current (I_P).*

have two states: parallel or anti-parallel. These two states correspond to the binary states (1 and 0) of the memory. To read out the memory cell, the orientation of the two magnetic layers has to be determined. This is done by sending a small electric current directly through the memory cell. When the orientation of the layers is parallel, the resistance of the memory cell is smaller than when they are not parallel. To write a memory cell, current is send through the corresponding word and bit lines. This current generates a magnetic field, which is used to change the direction of the magnetization.

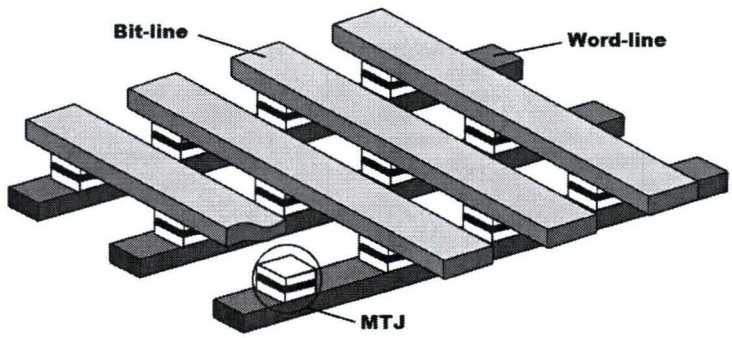

Figure 1.4: *A simplified MRAM structure made of MTJ-elements. A MTJ is sandwiched between the word and bit lines used to read and write the cell.*

Making use of the magnetic hysteresis of the MTJ, information can be retained even without electric power. This makes slow boot times of computers part of history. MRAM combines several properties of different memory types. It has the non-volatility of Flash, without the high voltage requirement and with a much higher read speed and storage density [12]. The

lifetime of MRAM is much longer than Flash. The read and write speeds are comparable to SRAM and the density to DRAM. The first MRAM's are demonstrated already [10], and will be ready for production in a few years.

Ordered arrays of magnetic nanostructures are particularly interesting to study because both the individual and collective behavior of the elements can be observed. In arrays, the individual elements may still have small differences, either due to the fabrication process or different grain structures, resulting in different edge roughness or other kinds of random defects. The interaction between the individual elements can also play an important role. Technologically, they are important for development of applications as MRAM, patterned recording media, magnetic switches, etc. Development of MRAM with higher bit densities need several issues related to fabrication, structure and functionality to be addressed. Scaling of MTJ's below lateral sizes of 100 nm requires sufficient control of the thickness and uniformity of the layers. As the lateral dimensions decrease the current density to switch the element will increase, while the thermal stability decreases. Thus, good control over the magnetic switching field is required and will stimulate new fundamental research on these issues.

1.3 Characterization techniques

It is important from a fundamental as well as an application point of view to understand and control the magnetic behavior (e.g. the magnetic switching field) of small magnetic elements. This requires techniques to characterize the magnetic properties. The magnetic properties such as the hysteresis loop can be characterized by standard techniques. However, it is more important to characterize the individual behavior of the nanostructures.

Generally, the magnetic behavior of magnetic specimens can be characterized by techniques like vibration sample magnetometery (VSM), superconducting quantum interference device magnetometers (SQUID), and magneto-optical Kerr effect (MOKE). However, these techniques lack nanometer resolution. As an example the magnetic moment of a 100×100 nm Co dot of 10 nm thickness is $1.4 \cdot 10^{-16}$ Am^2, which is far below the sensitivity of 10^{-8}–10^{-10} Am^2 from a typical SQUID magnetometer. There are, however, some techniques which allow the investigation of the magnetic properties of individual elements. These techniques include:

- Electron based microscopies (EM), like scanning electron microscopy with polarization analysis (SEMPA) and Lorentz microscopy (LM),

- Magneto-optical microscopies, as MOKE microscopy,
- Scanning probe microscopies, like spin polarized scanning tunneling microscopy (SP-STM), and magnetic force microscopy (MFM).

SEMPA SEMPA collects the spin polarized secondary electrons emitted by a magnetic sample [13]. The secondary electrons have magnetic moments which are parallel to the magnetization direction at the point of their origin (the magnetization of the sample). A magnetic image can be generated by measurement of the spin polarization at each point as a focused electron beam is scanned over the sample. SEMPA has a high spatial resolution (10 nm) which is determined by the beam width and it directly detects the sample magnetization. The major limitation of using SEMPA is sample preparation, as the experiment must be performed in ultra high vacuum conditions on a clean conducting surface to avoid loss of the secondary electron polarization by scattering.

Lorentz microscopy In Lorentz microscopy (LM), a high-energy electron beam is incident on a thin magnetic sample. The magnetic contrast is derived from the deflection of the electrons due to the Lorentz force ($F_L = q_e \boldsymbol{v} \times \boldsymbol{B}$) upon passing through the magnetization in the sample. The unique features of LM are high resolution (10-20 nm), high contrast, and a direct measurement of the magnetization vector. However, the disadvantages of this technique are that it requires very special sample preparation (very flat and transparent for electrons), and it is difficult to apply magnetic fields to the sample as this changes the electron beam trajectory.

Magneto-optical microscopy Magneto-optical microscopy is based on the rotation of the plane of polarization of linearly polarized light upon reflection from (Kerr), or transmission through (Faraday) a magnetic sample. The contrast in the image is directly related to the magnitude and direction of the magnetization. Typically magneto-optical images can be generated by conventional optics, or by scanning a focused laser spot across the sample. MO-microscopes use light for imaging and are thus limited in resolution to the wavelength of the light used (for visible light this is a few hundred nanometers), or in the case of a focused laser spot, on the size of the spot. The small penetration depth of light, and topographic sensitivity of the Kerr imaging mode requires samples that have optically flat, damage free surfaces.

Scanning probe microscopy The third class of magnetic microscopes include the scanning probe techniques. They are highly attractive because they inherently allow for simultaneous recording of sample topography and magnetic-domain images with high lateral resolution. Highest lateral resolutions in magnetic microscopy is currently obtained with spin-polarized STM [14]. Like all other techniques, spin-polarized STM has its limitations too. Problems are working in UHV, the need for a clean sample surface, and the superposition of magnetic and topography effects in the STM images cannot easily be differentiated [15]. Among magnetic scanning near-field microscopies, magnetic force microscopy (MFM)[16] is the most widely used. MFM records the magnetostatic force or force gradient between a magnetic sample and a magnetic tip. The principle of MFM will be presented later. The advantage of this technique is that it does not need special sample preparation, and can work in ambient conditions with a spatial resolution down to 10 nm. However, it is not easy to separate the magnetic contrast from other background forces. The interpretation of the observed magnetic contrast is not straightforward since MFM does not directly measure the magnetization distribution but rather the stray field.

1.4 Magnetic force microscopy

Magnetic force microscope (MFM) has recently become one of the most used methods in the research and development of magnetic nanodevices. The main strength of MFM in comparison with other magnetic imaging methods is that the measurements can, in principle, be performed under ambient conditions with no surface preparation necessary. It is possible to apply external magnetic fields during the measurement, so the field dependence of domain structures and magnetic reversal processes can be observed. A useful feature of MFM is that the magnetic structure can be seen even through relative thick non-magnetic insulating capping layers, because it detects the stray field of the sample rather than the magnetization. A major drawback of the MFM is that the complicated interaction between the magnetic probe and the sample makes quantitative interpretation of the MFM images difficult.

In magnetic force microscopy (MFM) a magnetic tip, attached to a flexible cantilever, is scanned above the sample surface as is displayed in Figure 1.5. The interaction between the sample and the tip is detected. The magnetic interaction provides information about the magnetization of the sample. The interaction range of the magnetic force is much larger than the interaction range of the atomic forces, so the interaction of the magnetic stray

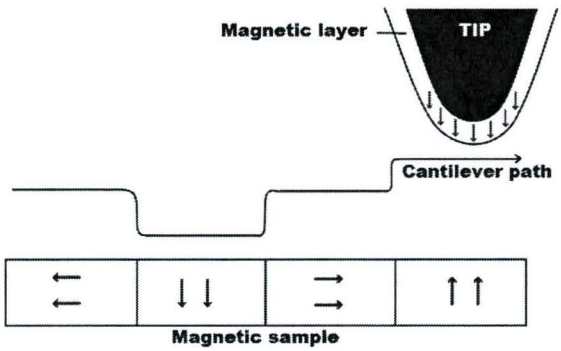

Figure 1.5: *Principle operation of MFM. A small tip, coated with magnetic material, is scanned over a sample. The tip is deflected by the sample magnetization. The deflection depends on the relative orientation of the tip and sample magnetization.*

field is measured at greater distance from the sample. The stray field and magnetization are, in general, related in a complex way. One problem that MFM must address is the separation of topographic and magnetic image contrast. To solve this, magnetic force microscopy is usually performed in "lift mode", in which a topographic image and a magnetic image (at a constant tip-sample distance) are acquired over the same area. Lift mode is not an analytical mode, but a measurement approach that allows imaging of long range interactions while minimizing the influence of topography. Measurements are taken in two passes across each scan line. In the first pass, topographical data is taken. The tip is then raised to the lift scan height and a second scan is performed, while maintaining a constant separation between tip and local surface topography (see Figure 1.6). Long range (magnetic) interactions are detected during this second pass. Using lift mode, topographical features are virtually absent from the image with the long range forces.

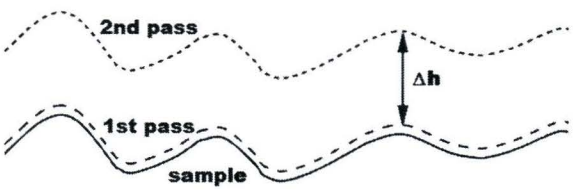

Figure 1.6: *Principle of the two pass method. The magnetic interaction is separated from the topography by making two passes. In the first pass the topography is detected, and the second pass is performed at a constant height Δh, above the sample.*

1.5 Motivation and thesis outlook

In the physics of nanostructures group[2] a Solver P47H AFM/MFM of NT-MDT [3] is acquired. With this microscope it is possible to perform magnetic force microscopy experiments. Implementation of an external magnetic field was necessary, because with the standard setup it was not possible to perform in-field measurements. In this thesis, not only the implementation of the magnetic field is discussed, but also focuses on a number of MFM measurements on nanostructured magnetic materials.

The report is divided into the following chapters. Chapter 2 will focus on the theory behind atomic force microscopy and magnetic force microscopy in particular. Chapter 3 describes the apparatus used. The components of an AFM/MFM will be discussed and some key features will be highlighted. Additionally, the implementation of an external magnetic field is explained, and some first results of in-field MFM measurements are presented. In chapter 4, magnetic force microscopy is used to study nanostructured magnetic devices. First, structured samples used in the development of magnetic read only memory (MROM) are investigated. These samples consist of a patterned substrate covered with a full magnetic (CoFe) layer. The magnetic stray field of this layer is detected and influenced with an external applied field. It will be shown that the stray field of individual bits can be detected with MFM. The magnetic state of the bits at non-zero applied magnetic fields seems to follow an easy and hard axis behavior, depending on the direction of the applied field. Next, multilayer structures intended for MRAM implementation are investigated. The magnetization of the individual bits is visualized, and it is seen that a non-uniform orientation is obtained for low fields, whereas the bit uniformly magnetizes for larger fields. In many cases the MFM tip influences the magnetization of the bits. For the research of all electrical spin-injection into semiconductors the magnetic switching field of small magnetic (CoFe) strips is determined as a function of the width of the strips. It found that the magnetic switch field of the strips is inversely proportional to the square of the width. Finally in chapter 5 the main conclusions of this work are presented.

[2]The Physics of nanostructures group is a research group of the department of applied physics at the Eindhoven Unversity of Technology

[3]Website: http://www.ntmdt.com

Chapter 2

Magnetic force microscopy

In this chapter the theory of magnetic force microscopy (MFM) is described. Magnetic force microscopy is a special mode of operation of the scanning force microscope (SFM). This special mode is realized by employing suitable (magnetic) probes and utilizing their specific properties. In MFM, a magnetic probe is brought close to a sample and interacts with the magnetic stray field near the surface.

First, in section 2.1 a general introduction to scanning force microscopy (SFM) is presented. The forces present in SFM are explained in section 2.1.1 and several operating modes are introduced in section 2.1.2. Next, magnetic force microscopy (MFM) is treated in section 2.2. In section 2.2.1 the general tip-sample interaction is explained, and in section 2.2.2 the response of a simplified tip model is presented. Finally, the resolution of SFM and MFM is discussed in section 2.3.

2.1 Scanning Force Microscopy

The discovery of the scanning tunneling microscope (STM) [17] has led to the development of a variety of other scanning probe microscopes. All scanning probe microscopes are based on the same technique: raster scanning a tip over a surface. One of the most successful microscopes is the scanning force microscope [18].

The principle of the operation of a scanning force microscope is schematically shown in Fig. 2.1. A sharp tip mounted on a flexible cantilever is scanned

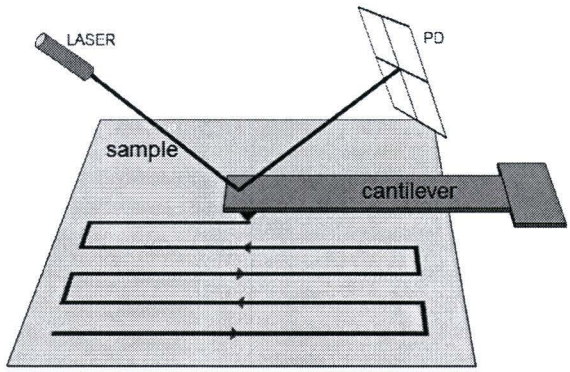

Figure 2.1: *Schematic representation of a scanning force microscope (SFM). Note that the sizes of the tip and the cantilever are strongly enlarged with respect to other sizes. A sharp tip mounted on a flexible cantilever scans the sample, thereby mapping the interaction between tip and sample. The tip-sample interaction bends the cantilever, and results in a displacement of the laser beam on the photodetector (PD).*

over a sample. The interaction force acting on the tip cause a measurable change in the state of the cantilever, such as a deflection. To form an image, the interaction is mapped as a function of position. All kind of forces between cantilever and surface can be measured, like the van der Waals force [19], the magnetic force and the electrostatic force [20, 21, 22]. Because of the vast number of SFM techniques, only the relevant part of SFM is presented. For a more detailed discussion on SFM it is advised to read other literature [23].

2.1.1 Interaction Forces

In general, the interaction between the force sensor and the sample is the sum of the capillary, van der Waals, electric and magnetic forces, which are compensated by elasticity forces resulting from the cantilever bending. These forces have different distance dependencies [24], which is indicated in Fig. 2.2. In vacuum, there are short-range quantum mechanical forces (acting on a sub-nm scale), and van der Waals, electrostatic, and magnetic forces with a longer range (up to 1 μm). In ambient conditions, meniscus forces formed by water layers on tip and sample can also be present. These forces will be treated here in some detail since some of them can influence the MFM measurements.

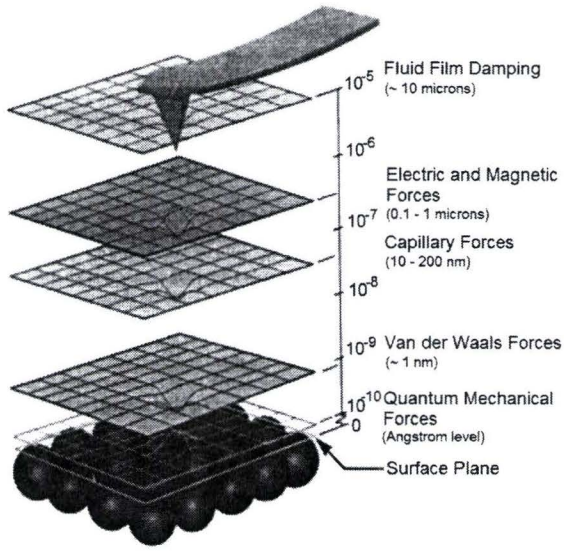

Figure 2.2: *Different forces acting on a tip and the distance region where they dominate the signal. Adapted from [25].*

Film Damping

Film damping is only encountered by oscillating cantilevers. A damping film is developed when the oscillating cantilever approaches the surface within 10 microns. At this distance air is compressed between the probe and the surface in each "down stroke" of the cantilever. The opposite happens in the "up stroke", a partial vacuum is formed. This pumping effect dampens the cantilever oscillation, and may lead to false identification of the surface. If the boundary is passed, this damping disappears.

Electrostatic forces

Next to magnetic forces, which will be treated later, electrostatic forces are the most important influence on the tip above 10 nm distance. When the tip and the sample are both conductive and have an electrostatic potential difference ($V \neq 0$), electrostatic forces are important. If the distance d between a flat surface and a spherical tip with radius R, is small compared to R, the electrostatic force [26] is approximately given by:

$$F_{\mathrm{el}} = -\frac{\pi \epsilon_0 R V^2}{d}, \tag{2.1}$$

where ϵ_0 is the permittivity of free space and V is the voltage between tip and sample. Electrostatic forces can be avoided by taking appropriate measures for grounding.

Capillary forces

Under ambient conditions, a film of several nanometer thickness, containing mostly water, covers all surfaces. This film is attracted by the tip due to van der Waals forces. If the water film is thick enough, molecules will migrate under the tip, reducing the effective tip to sample separation. When the tip penetrates the water a meniscus will be formed, as can be seen in Fig. 2.3. The tip is strongly pulled towards the sample surface by capillary forces. This force can lead to destruction of the tip or the sample surface. Operating in vacuum or in dry air conditions can prevent this problem.

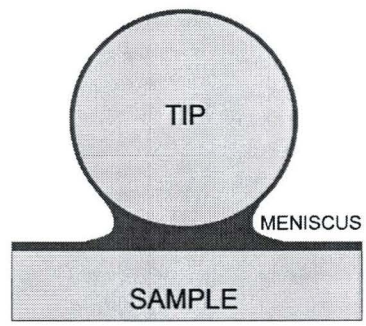

Figure 2.3: *The capillary force. The water layer on the sample wets the cantilever surface (represented as a sphere) because the water-cantilever contact is energetically advantageous as compared to the water-air contact.*

Van der Waals force

Below 10nm tip-sample distance the influence of the van der Waals force increases. The van der Waals force arises from fluctuations in the electric dipole moment of atoms and their mutual polarization. Although van der Waals forces between atoms act on a short range (the van der Waals force at short distances decays as $F \propto z^{-7}$), summation of the individual force of each atom of the tip with each atom of the sample results in a long-range tip-sample interaction. The van der Waals force strongly depends on the shape of the interacting bodies. In a simple approximation for a geometry (sphere-plane) that resembles the tip-surface interface, that is, a sphere of

radius R at a distance z from a surface, the force dependence [27] is:

$$F \cong -\frac{HR}{6z^2}. \tag{2.2}$$

When the distance z is small compared to the radius R. H is the material-dependent Hamaker constant. For a spherical tip the force decays quadratically with distance.

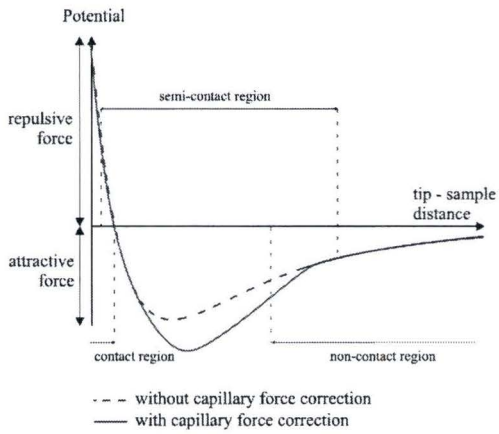

Figure 2.4: *A typical force-distance curve. The tip-sample interaction as a function of tip-sample distance. The regions of the scanning modes can be seen. Also the correction for the capillary forces is shown.*

Fig. 2.4 shows a typical force-distance curve. Upon approach of the tip towards the sample, the negative attractive forces, for example, the van der Waals forces, increase until a maximum is reached. From this point the repulsive forces, caused by the coulomb repulsion, will start to dominate upon further approach.

Two regions are labeled in Fig. 2.4: 1) the contact region; and 2) the non-contact region. In the contact region, the cantilever is held less than a few angstroms from the sample surface, and the interatomic force between the cantilever and the sample is repulsive. In the non-contact regime, the cantilever is held several nanometers from the sample surface and the interatomic force between the cantilever and sample is attractive (largely a result of the long-range Van der Waals interactions).

Quantum mechanical forces

Quantum mechanical forces become important in a region below 1 nm distance. Their short decay length causes only a few atoms at the very end of

the tip to contribute to the interaction. There is also a quantum mechanical force which might be interesting for magnetic imaging: the exchange force. Detecting it would give the possibility of true atomic resolution in magnetic force imaging. It obviously requires ultra clean and ultra flat surfaces under UHV conditions, which means that the study of technologically attractive materials like magnetic recording media will be more complicated.

2.1.2 Operating modes

There are two principal operating modes for an AFM: constant-interaction mode and variable-interaction mode. In variable-interaction mode, the scan-

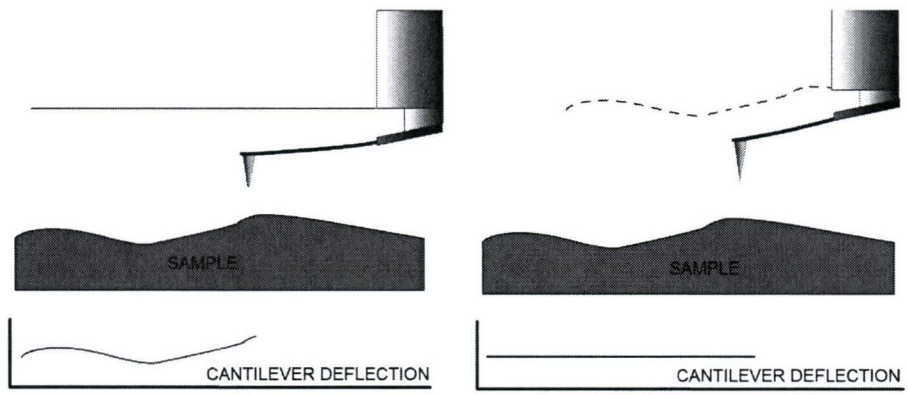

Figure 2.5: *The main operating mode of a SFM:(Left) Variable-interaction mode. The scanner is kept at a constant height during scanning. Therefore, the deflection (proportional to the interaction force) changes with lateral position. (Right) Constant-interaction mode. The scanner height is changed to keep the interaction (and deflection) constant.*

ner travels in a horizontal plane above the sample and the deflection changes with the variation in interaction force, depending on the topography and other local properties (see Fig. 2.5). The force measured at each location constitutes the data set, i.e., the topographic image. This mode is fast because the scanner does not have to move up and down. However, only smooth surfaces can be imaged where there is no risk of collisions. In constant-interaction mode (see Fig. 2.5), the AFM uses a feedback loop to keep the deflection, and thus the interaction force, constant by adjusting the height of the scanner at each point. In this case the vertical motion of the scanner constitutes the data set. Most surface measurements in AFM are performed in constant-interaction mode: irregular surfaces can be imaged with high precision, but the measurement takes a longer time than in variable-interaction mode, because the response time of the feedback system

determines the maximum scan rate.

The constant-interaction mode can be further divided in two distinct modes: static (DC) and dynamic (AC) modes.

Static mode

In static mode the vertical displacement of the scanner is used as the imaging signal. The force acting on the tip is measured through the static deflection of the cantilever. According to Hookes law the displacement Δz (see Fig. 2.6) of the cantilever is proportional to the exerted force F:

$$F = k \cdot \Delta z, \tag{2.3}$$

where k is the spring constant of the cantilever. The detected force component F_d is given by:

$$F_d = \hat{\boldsymbol{n}} \cdot \boldsymbol{F}, \tag{2.4}$$

where $\hat{\boldsymbol{n}}$ is the unit vector normal to the plane of the cantilever.

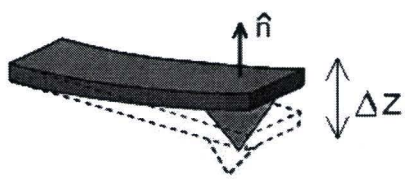

Figure 2.6: *representation of the deflection of a cantilever by Δz. The unit vector normal to the plane of the cantilever is indicated by $\hat{\boldsymbol{n}}$.*

The deflection is monitored during the measurement, and any change is instantly followed by a vertical adjustment of the scanner in order to maintain a preset deflection value. The resulting image is a map of constant interaction, which should represent the surface topography.

Static mode measurements can take place in vacuum, ambient or liquid environments. In ambient conditions a thin film of water is present on the sample, and a meniscus will form (section 2.1.1). The meniscus implies an attractive force that shows a dependence with distance. All the attractive forces combined create a frictional force as the tip scans the sample. Frictional forces may distort image features, and even blunt the tip or cause damage to the sample. Therefore, careful control is necessary and the static mode is most suitable to image hard surfaces.

Dynamic mode

In dynamic mode the cantilever is mounted on a piezo-electric element that vibrates at a fixed frequency (Ω) close to the resonance frequency ($\Omega \approx \omega_0$) of the cantilever. The resonance frequency is given by:

$$\omega_0 = \sqrt{\frac{k}{m}} \tag{2.5}$$

where m is the effective mass of the spring. When the tip approaches the sample, tip-sample interactions cause a change in the resonance frequency (and consequently also in the amplitude and phase) of the cantilever. AC detection methods are used to measure these changes, thus providing a feedback signal that allows the tip-sample interaction to be held constant. A schematic overview of the dynamic mode setup is displayed in Fig. 2.7.

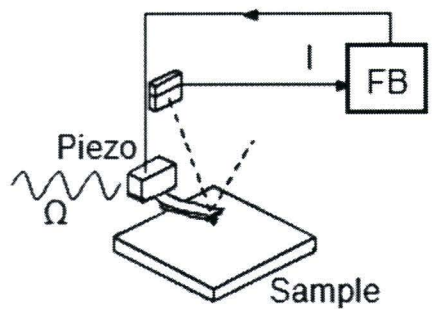

Figure 2.7: *Overview of the system. The cantilever is attached to a piezo-electric element vibrating at a frequency Ω. A feedback system keeps the interaction constant.*

AC detection mode was initially meant to be a non-contact mode [19, 28]. In this case the tip keeps a distance of about 5-15 nm above the sample surface, in order to stay separated from the liquid layer. Topographic information is obtained from the weaker van der Waals forces (and other long range forces) acting between the tip and the sample. The magnitude of the long-range forces are normally substantially lower than the short-range forces, as can be seen in Figure 2.4.

Later, AC detection mode was used very successfully at a closer distance range in ambient conditions involving repulsive tip-sample interactions. This so-called "tapping mode" is a method to achieve high resolution without inducing destructive frictional forces. The oscillation amplitude is typically larger than 20 nm in free air. The oscillating tip is lowered towards the sample surface until an intermittent contact is established, where the tip

only touches the surface at the bottom of the oscillation. When the tip passes over a hill in the surface, the cantilever has less room to oscillate and the amplitude of oscillation decreases. Conversely, when the tip passes over a valley, the cantilever has more room to oscillate. Tapping mode prevents the tip from sticking to the surface and causing damage, because when the tip contacts the surface it has sufficient oscillation amplitude to overcome the tip-sample adhesion forces.

The cantilever can be represented as a mass-spring system, as can be seen in Fig. 2.8. If a cantilever is excited sinusoidally at its clamped end, with

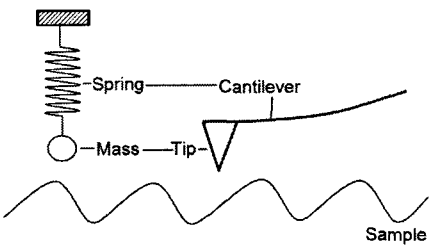

Figure 2.8: *Similarity between a mass spring system (left) and a cantilever (right). Both consists of a mass (tip) on a spring (cantilever).*

frequency Ω and amplitude A_0, the tip will oscillate with a certain amplitude A, exhibiting a phase shift ϕ with respect to the driving signal. The equation of motion for this cantilever is:

$$m\ddot{z} + \frac{m\omega_0}{Q}\dot{z} + kz = A_0 k\cos(\Omega t), \tag{2.6}$$

where z is the cantilever deflection, $\dot{z} = dz/dt$, $\ddot{z} = d^2z/dt^2$, and m the mass of the cantilever. The quality factor Q is determined by the resonance frequency (ω_0) from equation (2.5) and the damping factor (γ) according to:

$$Q = \frac{m\omega_0}{\gamma}. \tag{2.7}$$

The quality factor ranges from below 100 for liquids, air or other gasses to more than 10^5 in UHV conditions. Equation (2.6) gives the steady state solution:

$$z(t) = A\cos(\Omega t + \phi), \tag{2.8a}$$

$$A = \frac{A_0\omega_0^2}{\sqrt{(\omega_0^2 - \Omega^2)^2 + \frac{\omega_0^2\Omega^2}{Q^2}}}, \tag{2.8b}$$

$$\phi = \arctan\frac{\omega_0\Omega}{Q(\Omega^2 - \omega_0^2)}, \tag{2.8c}$$

where ϕ is the phase lag with respect to the driving force. A consequence

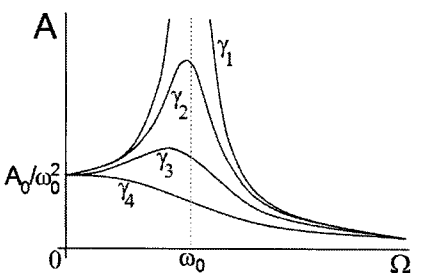

Figure 2.9: *Amplitude curve for different values of damping factor:* γ_1/ω_0=0, $\gamma_2/\omega_0 = 0.2$, $\gamma_3/\omega_0 = 0.4$, $\gamma_4/\omega_0 = 0.8$.

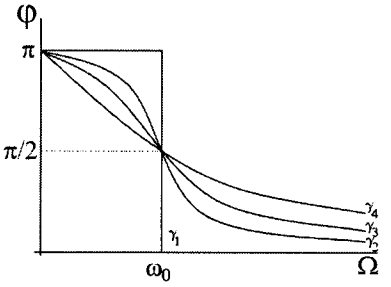

Figure 2.10: *Phase shift ϕ between driving force and oscillations depending on driving frequency.*

of damping is the qualitative change in the resonance curve shape. Figures (2.9) and (2.10) show the amplitude and phase shift for some characteristic values of damping.

The above result is derived for free oscillations. Under the influence of a tip-surface interaction an extra force $F_{\text{int}}(z)$ affects the motion of the cantilever. The total force F on the cantilever includes the driving force ($A_0\cos(\Omega t)$) and an extra interaction force $F_{\text{int}}(z)$. The interaction force can be approximated by a Taylor series:

$$F_{\text{int}} = F(z_0) + \left.\frac{\partial F}{\partial z}\right|_{z_0} (z - z_0) + O(z^2) \tag{2.9}$$

around the oscillator equilibrium position z_0, which can be determined from Hooke's law 2.3 by:

$$z_0 = \frac{F_{\text{int}}}{k}. \tag{2.10}$$

Substituting $\tilde{z}(t) = z(t) - z_0$, and taking (2.10) into account, the new equation of motion becomes:

$$m\ddot{\tilde{z}} + \frac{m\omega_0}{Q}\dot{\tilde{z}} + \left(k - \frac{\partial F}{\partial \tilde{z}}\right)\tilde{z} = A_0\cos(\Omega t). \tag{2.11}$$

Under the influence of a force gradient, the cantilever behaves like it has a modified spring constant:

$$k_{\text{eff}} = k - \frac{\partial F}{\partial z}, \tag{2.12}$$

where k is the natural spring constant and $\partial F/\partial z$ is the derivative of the interaction force relative to the perpendicular coordinate z. This change in

effective spring constant also changes the resonant frequency of the tip by

$$\omega = \sqrt{\frac{k_{\text{eff}}}{m}} = \sqrt{\frac{k - \partial F/\partial z}{m}} = \sqrt{\frac{k}{m}}\sqrt{1 - \frac{\partial F/\partial z}{k}} = \omega_0\sqrt{1 - \frac{\partial F/\partial z}{k}}, \tag{2.13}$$

where ω_0 is the resonant frequency in the absence of a force gradient. An attractive interaction with $\partial F/\partial z > 0$ will effectively make the cantilever spring softer, so that its resonance frequency will decrease. If $\partial F/\partial z$ is small relative to k the change in resonant frequency becomes:

$$\Delta\omega = \omega - \omega_0 \approx -\frac{\omega_0}{2k}\frac{\partial F}{\partial z}. \tag{2.14}$$

A shift in resonant frequency ($\Delta\omega$) will result in a change in oscillation amplitude (A) and phase shift (ϕ) according to (2.8). If the cantilever is oscillated at its resonant frequency $\Omega = \omega_0$, the phase shift is $\alpha = \pi/2$. In case there is a force gradient present, the new phase shift is obtained by substitution of (2.13) in (2.8c) and becomes:

$$\tilde{\phi} = \arctan\frac{k}{Q\frac{\partial F}{\partial z}}. \tag{2.15}$$

A Taylor expansion of (2.15) gives

$$\tilde{\phi} \approx \frac{\pi}{2} - \frac{Q}{k}\frac{\partial F}{\partial z}. \tag{2.16}$$

The additional phase shift due to a force gradient $\partial F/\partial z$ can be expressed as:

$$\Delta\phi = \tilde{\phi} - \frac{\pi}{2} \cong -\frac{Q}{k}\frac{\partial F}{\partial z}. \tag{2.17}$$

In Figure 2.11 the phase shift ($\Delta\phi$) due to a resonant frequency shift ($\Delta\omega$)

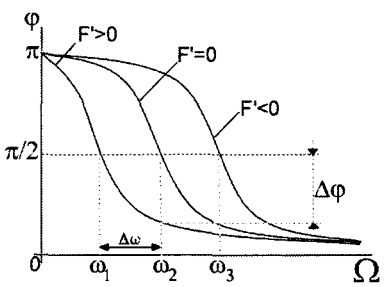

Figure 2.11: *Phase shift ($\Delta\phi$) due to a resonant frequency shift ($\Delta\omega$), for different values of force gradient $F' = \partial F/\partial z$.*

is shown. Note that an attractive interaction ($\partial F/\partial z > 0$) leads to a negative phase shift (dark contrast in the image), while a repulsive interaction ($\partial F/\partial z < 0$) gives a positive phase shift (bright contrast).

2.2 Magnetic force microscopy

Scanning force microscopy on magnetic samples with a magnetic tip is known as magnetic force microscopy (MFM). One of the first magnetic force microscopy (MFM) images were measurements of forces from a magnetic recording head [29]. Thereafter images were made of structures in magnetic materials, which were believed to be domain walls [30, 31]. Soon, images of thermomagnetically written domains [32] followed. This proved that MFM was able to image technologically important data storage materials. Recently, the use of MFM has grown rapidly, because it is the only technique that is able to produce high resolution images without special sample preparation or special measurement conditions. Images can even be made when the sample is protected by a special capping layer.

To gain insight in the magnitude of forces involved in MFM, the force between two magnetic particles can be calculated. One particle (with dipole moment $\boldsymbol{m_1}$) represents the tip, the other ($\boldsymbol{m_2}$) the sample. The force between the two dipole particles separated a distance $r = |\boldsymbol{r_1} - \boldsymbol{r_2}|$ is [30]:

$$\boldsymbol{F} = \frac{\mu_0}{4\pi} \nabla \left(\frac{3(\boldsymbol{m_1} \cdot \boldsymbol{r})(\boldsymbol{m_2} \cdot \boldsymbol{r})}{r^5} - \frac{\boldsymbol{m_1} \cdot \boldsymbol{m_2}}{r^3} \right). \tag{2.18}$$

If the dipoles point in the z-direction and $\boldsymbol{r}$ is also in the z-direction, the force F can be expressed as

$$F_z = -\frac{3\mu_0 m_1 m_2}{2\pi z^4}, \tag{2.19}$$

and the force derivative $\partial F/\partial z$ is:

$$\frac{\partial F}{\partial z} = \frac{6\mu_0 m_1 m_2}{\pi z^5}. \tag{2.20}$$

For two cobalt particles with a diameter of 10 nm and corresponding magnetic moment $m = 7.6 \cdot 10^{-19}\mathrm{Am}^2$, separated 10 nm (center to center), the resulting force is $F = 3.4 \cdot 10^{-11}$ N and the force gradient $\partial F/\partial z = 1.4 \cdot 10^{-2}$ Nm^{-1}. From section 2.3 it follows that these magnitudes are easily detected by MFM.

The interpretation of images acquired with magnetic force microscopy requires knowledge about the magnetostatic interaction between tip and sample. In the following section a more detailed description of the magnetic interactions measured with MFM is presented. This will provide a basis for interpreting the images obtained. In section 2.2.1 the general theory describing the magnetostatic interaction between an arbitrary tip and sample is presented. Because of the complexity of the general theory, simplifications are usually made. In section 2.2.2 the tip magnetization is replaced by a simple model, and some representative patterns are presented.

2.2.1 Magnetic Interaction

The principle of operation of magnetic force microscopy is the same as scanning force microscopy in section 2.1. Both static and dynamic detection modes can be applied, but mainly the dynamic mode is used due to the better sensitivity. The force derivative $\partial F/\partial z$ from equation (2.12) can originate from a wide range of sources, including van der Waals forces, damping, capillary forces, or electrostatic tip-sample interactions (section 2.1.1). However, MFM is based on the forces that arise from the magnetostatic coupling between tip and sample. This coupling depends on the internal magnetic structure of the tip, which greatly complicates the mechanism of contrast formation. In this section the force gradient from equation (2.17) is related to the magnetic stray field of the sample.

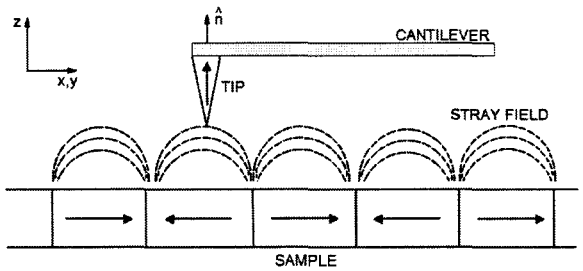

Figure 2.12: *Basic concept of magnetic force microscopy. A magnetic tip attached to a flexible cantilever is used to detect the magnetic stray field of a sample.*

Figure 2.12 illustrates the basic concept of magnetic force microscopy. A magnetic tip with magnetization $\boldsymbol{M}_{tip}$ interacts with a magnetic stray field ($\boldsymbol{H}_{sample}$) emanating from a sample. The energy of the tip exposed to this stray field is (see also [24]):

$$E = -\mu_0 \int_{tip} \boldsymbol{M}_{tip} \cdot \boldsymbol{H}_{sample} dV. \tag{2.21}$$

The force acting on the tip is given by the gradient of the energy:

$$\boldsymbol{F} = -\nabla E = \mu_0 \int_{tip} \nabla(\boldsymbol{M}_{tip} \cdot \boldsymbol{H}_{sample}) dV. \tag{2.22}$$

The integration is performed over the whole magnetic volume of the tip. Simplified models for the tip geometry and its magnetic structure are often used in order to make such calculations feasible.

The sample stray field $\boldsymbol{H}_{sample}$ is given by the gradient of a magnetostatic potential [33]:

$$\boldsymbol{H}_{sample}(\boldsymbol{r}) = -\nabla \phi_s(\boldsymbol{r}), \tag{2.23}$$

where the magnetostatic potential $\phi_s(\boldsymbol{r})$ created by a ferromagnetic sample with magnetization vector field $\boldsymbol{M}_s(\boldsymbol{r}')$ is [34]:

$$\phi_s(\boldsymbol{r}) = \frac{1}{4\pi}\left(\int_{S_s} \frac{\boldsymbol{M}_s(\boldsymbol{r}')\cdot d^2\boldsymbol{s}'}{|\boldsymbol{r}-\boldsymbol{r}'|} + \int_{V_s} \frac{\nabla\cdot\boldsymbol{M}_s(\boldsymbol{r}')}{|\boldsymbol{r}-\boldsymbol{r}'|} d^3r'\right), \tag{2.24}$$

with $\boldsymbol{s}'$ an outward normal vector from the sample surface. The first integral is the integral over the sample surface S_s. This covers all surface charges created by magnetization components perpendicular to the surface. The second integral covers all volume charges in the sample volume V_s.

The sample stray field (equation (2.23)) can be substituted in equation (2.22) to calculate the interaction force $\boldsymbol{F}$. In dynamic mode (section 2.1.2), the tip is oscillated at its resonance frequency with an amplitude small compared to the tip-sample distance, and the force derivative is detected. The force gradient in the direction normal to the plane of the cantilever (see Fig. 2.6) can be written as:

$$\frac{\partial F}{\partial n} = \hat{\boldsymbol{n}}\cdot\nabla\left(\hat{\boldsymbol{n}}\cdot\boldsymbol{F}\right) \tag{2.25}$$

Similar to AFM(see section 2.1.2), the detected force gradient (2.25) gives rise to a phase shift (Eq. 2.17). Fig. 2.13 shows an MFM image from a phase shift measurement obtained with our MFM. The sample is a standard hard disk sample that is used to check that the microscope is correctly configurated to image magnetic materials. The topography (a) is relative flat, and a small magnetic signal can be observed in the topography. In the MFM image (b) magnetic bits can be identified by the black/white contrast. The bits are arranged in tracks, separated by regions without magnetic contrast.

2.2.2 Modelling tip response

Equation (2.21) and (2.22) are valid for arbitrary tip magnetization ($\boldsymbol{M}_{tip}$). Unfortunately, the magnetization of the tip is generally unknown. Therefore, simplified models are used to replace the real tip magnetization with an appropriate approximation. The most used model is the point-probe approximation (Figure 2.14). This model assumes that the effective monopole (q) and dipole ($\boldsymbol{m}$) moments resulting from a multipole expansion [33] of equation (2.21) are projected in a fictitious tip of infinitesimal size. The unknown magnetic moments ($q, \boldsymbol{m}$) as well as the effective tip-sample separation (h) are treated as free parameters to be fitted to the experimental data. The force on the tip in the sample stray field (in the absence of

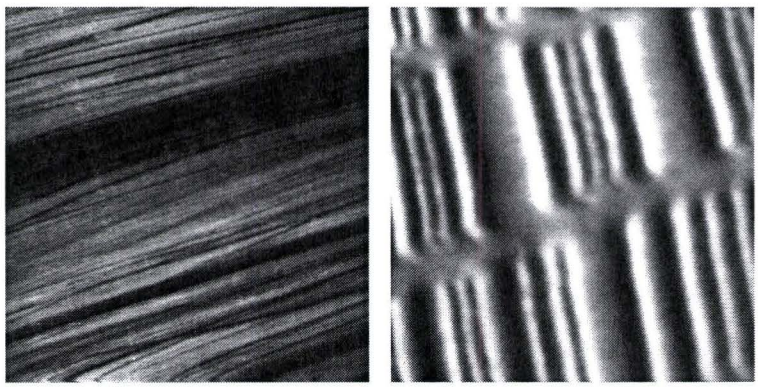

(a) (b)

Figure 2.13: *MFM scan of a hard disk sample. Scan size is 10×10 μm. (a) The topography. The magnetic signal emanating from the bits can also be seen. (b) Tracks of magnetic bits can be seen indicated by the black and white contrast. Regions without magnetic contrast separate the tracks.*

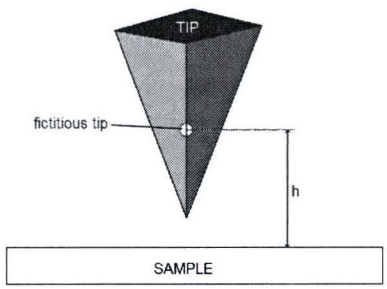

Figure 2.14: *Representation of the point-probe model. The MFM tip is replaced by a fictitious tip of infinitesimal size, with an effective monopole q and dipole* $\boldsymbol{m}$ *at height h above the sample.*

currents ($\nabla \times \boldsymbol{H} = 0$)) is given by:

$$\boldsymbol{F} = \mu_0(q + \boldsymbol{m} \cdot \nabla)\boldsymbol{H}. \tag{2.26}$$

From Hooke's law (Eq 2.3), the resulting deflection can be described by:

$$\Delta z = \frac{\mu_0}{k} \sum_{i=1}^{3} n_i \left(qH_i + \sum_{j=1}^{3} m_j \frac{\partial H_j}{\partial x_i} \right) \tag{2.27}$$

where the summation over i and j is taken over the spatial coordinates x,y,z.

The phase shift according to equation (2.17) then becomes:

$$\Delta\phi = \frac{\mu_0 Q}{k} \sum_{i=1}^{3}\sum_{j=1}^{3} n_i n_j \left[\left(\frac{\partial q}{\partial x_i} + q\frac{\partial}{\partial x_i} \right) H_j(\boldsymbol{r}) + \sum_{k=1}^{3} \left(\frac{\partial m_k}{\partial x_i}\frac{\partial}{\partial x_j} + m_k \frac{\partial^2}{\partial x_i \partial y_i} \right) H_k(\boldsymbol{r}) \right]. \quad (2.28)$$

From equation 2.28 it becomes clear that the signal is not only proportional to the second derivative of the stray field, but also to the first derivatives and to the field components themselves.

By considering some special cases, equations (2.27) and (2.28) can be considerably simplified. For example, if it is assumed that the cantilever is parallel to the sample (in Fig. 2.12: $\hat{\boldsymbol{n}} = \hat{\boldsymbol{z}}$), then:

$$\Delta z = \frac{\mu_0}{k}\left(m_x \frac{\partial H_x}{\partial z} + m_y \frac{\partial H_y}{\partial z} + m_z \frac{\partial H_z}{\partial z}\right) \quad (2.29)$$

$$\Delta\phi = \frac{\mu_0 Q}{k}\left(m_x \frac{\partial^2 H_x}{\partial z^2} + m_y \frac{\partial^2 H_y}{\partial z^2} + m_z \frac{\partial^2 H_z}{\partial z^2}\right) \quad (2.30)$$

This shows that the component of the stray field which is measured depends on the orientation of the tip moment (e.g. m_z couples to H_z). In Fig. 2.15 the typical stray field (H_z) and second derivative ($\partial^2 H_z/\partial z^2$) can be seen for perpendicular and in-plane magnetization patterns.

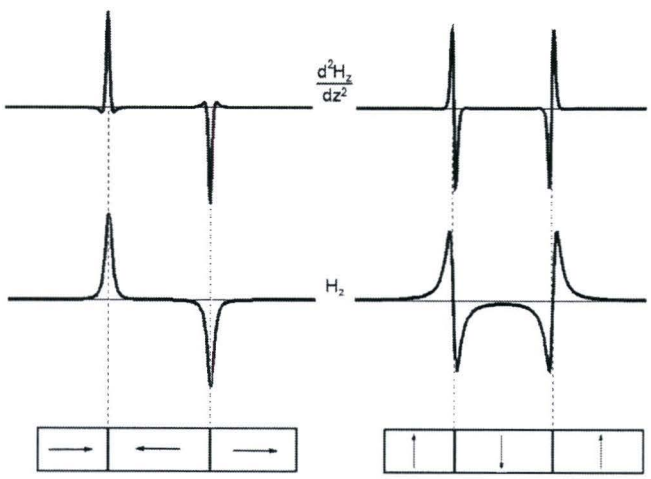

Figure 2.15: *The magnetic stray field (H_z) and second derivative ($\partial^2 H_z/\partial z^2$) above perpendicular and in-plane magnetized patterns.*

The point-probe approximation gives satisfactory results in many cases, but a more realistic approach can be achieved with extended charge models. An example is the pseudodomain model [34], in which the unknown magnetization vector field near the tip apex is modeled by a homogeneously magnetized prolate spheroid of suitable dimensions. The magnitude and dimensions of the magnetization of the ellipsoidal domain are both completely rigid. The magnetic response of the probe outside this hypothetical domain is neglected. This model allows interpretation of most results obtained with bulk probes.

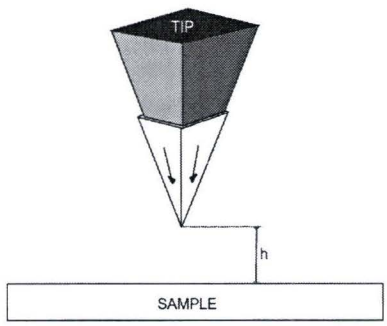

Figure 2.16: *Extended charge model. The MFM tip is approximated by a pyramid with different magnetization vectors on different facets.*

For probes with different geometry, for example those where the magnetic region is confined to a thin layer (Fig. 2.16), other models have been developed. As a practical situation consider longitudinal magnetic recording media, where the magnetization is parallel to the sample surface. MFM detects the magnetic stray field produced by such a magnetized medium. Fig. 2.17 shows an MFM measurement (a) and the calculated MFM response (b) of 5 μm long bits [35]. In this particular case, the tip was modeled as a uniformly magnetized truncated cone with a spherical end. The magnetic transition geometry and the stray field configuration (H_x and H_z) are shown in (c).

These special cases treated above are only approximations which are not completely valid for actual tips. A realistic simulation generally requires the integration over the entire tip volume as in equation 2.22. A limitation in the use of MFM is that the magnetic configuration of the tip is rarely known in detail. The general theory of contrast formation still holds, but MFM can generally not be performed in a quantitative way, in the sense that a stray field would be detected in absolute units. Furthermore, because MFM is sensitive to the strength and polarity of near-surface stray fields (according to equation 2.28) produced by ferromagnetic samples, rather than to the magnetization itself, the magnetization cannot be determined uniquely, since

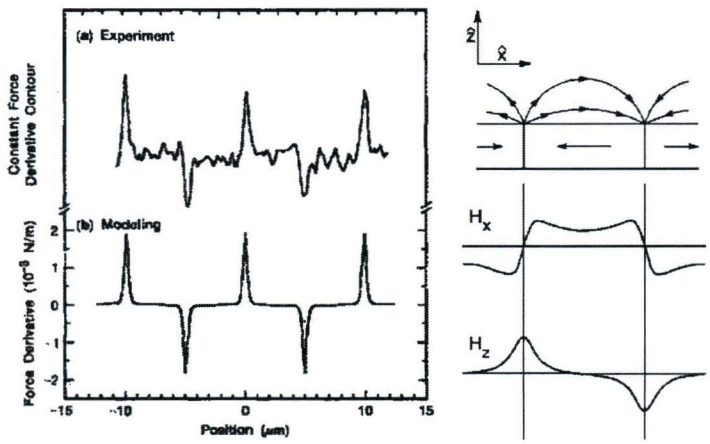

(a) and (b) (c)

Figure 2.17: *(a) Constant force derivative contour, measured on a 5 – μm bit sample. (b) Corresponding model of magnetic force derivative. (c) Typical variation of H_x and H_z above the medium. Adapted from [35]*

there may be an infinite number of magnetization patterns yielding the same stray field [36]. MFM can supply information which, when combined with other techniques, may in principle allow a complete determination of the magnetization [37].

2.3 Resolution

A SFM generates three-dimensional images, therefore two types of resolution need to be distinguished: lateral and vertical. This will be discussed in some detail below.

Vertical resolution

For DC detection methods, the minimum force that can be detected depends on the sensitivity of the detection system and on the spring constant. The sensitivity of the detection system is usually in the order of 10^{-2} nm [16]. The spring constant k is in the order of 1 Nm^{-1}. According to Hooke's law (2.3), this leads to a minimum detectable force of $F_{\mathrm{min}} = 10^{-11}$ N.

In AC detection methods, vertical resolution is limited both by noise from the detection system and by thermal fluctuations of the cantilever. Damping systems can be employed to minimize mechanical vibrations, which leaves thermal noise as the main source. For cantilevers with a spring constant k, the RMS amplitude can be derived from the equipartition theorem [38]:

$$\frac{1}{2}k\left\langle(\Delta z)^2\right\rangle = \frac{1}{2}k_BT \tag{2.31a}$$

$$\text{or :} \qquad \sqrt{\langle(\Delta z)^2\rangle} = \sqrt{\frac{k_BT}{k}} \tag{2.31b}$$

where T is the temperature and k_B the Boltzmann constant. Therefore, at room temperature the thermal vibration amplitude for a typical spring constant of $k = 1$ Nm^{-1} is 0.6 Å. The minimal detectable force gradient at room temperature is in the order of $10^{-4} - 10^{-5}$ Nm^{-1} [19].

It is instructive to compare the minimum detectable force gradient of the AC technique to the minimum detectable force measured with the DC technique. Assuming a inverse square force law ($F \sim -z^{-2}$) from equation (2.2), the force and force gradient are related by:

$$|F(z)| = \frac{z}{2}\frac{\partial F}{\partial z} \tag{2.32}$$

For a typical tip separation of $10 - 100$ nm and a force gradient of $10^{-4} - 10^{-5}$ Nm^{-1}, the minimal detectable force is $5 \cdot 10^{-13}$ N. This force would deflect a static cantilever with a spring constant of 1 Nm^{-1} by $5 \cdot 10^{-4}$ nm, which is usually not detectable by the detection system. So AC detection techniques offer a significant advantage in detection sensitivity for long-range forces.

Lateral resolution of AFM

Lateral resolution in AFM depends on tip size and shape, tip-surface separation, and interaction force. Besides that, distinction has to be made between the resolution of periodic structures and of single objects. High resolution usually means that the system is capable of separating two closely spaced objects. Detecting one single small object has to do with sensitivity. Resolution can therefore be defined as the minimum spacing between two objects that can still be observed. Two-dimensional crystals have been observed [39] with atomic resolution as can be seen in Fig. 2.18, but atomic defects or single atoms are rarely imaged with the AFM. When it comes to resolving single objects, the tip radius is the limiting factor. The finite tip size is responsible for the often observed broadening effects in SFM images, where

lateral dimensions of single objects tend to be overestimated. In constant interaction mode atomic scale resolution can be resolved [40]. For other materials it was only possible to show the unit-cell periodicity. Demonstration of atomic scale resolution is shown by the observation of surface defects.

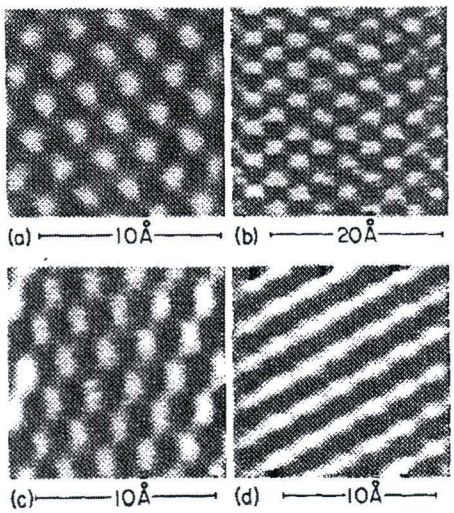

Figure 2.18: *Atomic resolution of different samples: (a)graphite, (b) molybdenum disulfite, and (c) boron nitride. (d)Boron nitride imaged with a bad tip, showing a distorted image. Adapted from [39].*

Lateral resolution of MFM

The theoretical lateral resolution limit for MFM measurements in ambient conditions is around $5 - 10$ nm [41]. There are some publications of MFM studies approaching this limit [42, 43], but standard MFM resolution is typically in the order of $50 - 100$ nm [35]. The lateral resolution achieved with MFM, depends on the properties of the tip as well as on the properties of the stray field distribution. For a point dipole tip, and a point dipole object on the sample, the width of the measured signal will be finite and in the order of the tip-surface separation [35]. High spatial resolution is thus obtained by operating the tip close to the sample surface. The minimal tip-sample separation is determined by several experimental limitations:

- For dynamic detection modes, a minimum oscillation amplitude in the range of $1 - 10$ nm is typically required. The tip-sample distance has

to be larger than this amplitude.

- If the force derivative becomes too large at small tip-sample distances, the system can become unstable. Stiffer cantilevers allow operation at smaller distances, at the cost of reduced sensitivity (eq. 2.17 and eq. 2.28).
- The stray field of the tip can disturb the sample magnetization, especially when the distance becomes small, preventing non-destructive MFM operation. An example of this phenomenon can be seen in paragraph 4.3.

Chapter 3

Setup

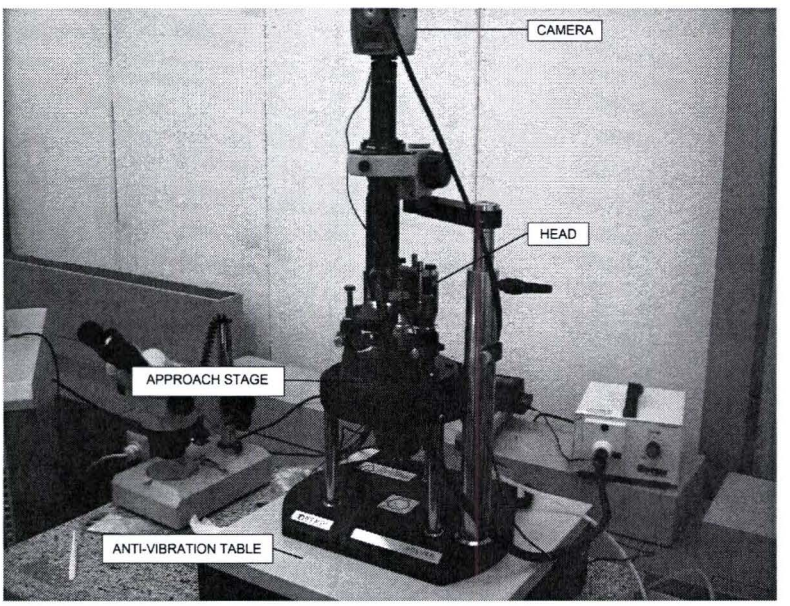

Figure 3.1: *The setup used for the measurements in this thesis. The main component is the scanner head. The sample is placed on the approach stage, which is situated on an anti-vibration table. A camera monitors the tip and sample.*

The experiments in this thesis were performed with a Solver P47H from NT-MDT[1], operated at room-temperature under ambient conditions. The complete setup can be seen in Fig. 3.1. The setup consists of a scanning probe microscope (the head), mounted on an automated approach stage. To reduce external vibrations, the approach stage is placed on an active

[1]Website: http://www.ntmdt.com

anti-vibration table. The microscope is connected to an electronic unit, which itself is connected to a computer, controlling all measurements. In this project, an electromagnet is made to perform measurements in the presence of an external magnetic field. A camera is placed above the setup to monitor the sample and cantilever. The design and operation of atomic force microscopes is well described in literature [44, 45, 46]. The basic components and components relevant for the performed experiments will be discussed here.

3.1 The microscope

The main component of the setup is the scanning probe microscope, more precisely, an atomic force microscope capable of magnetic force microscopy. The microscope used is a Solver P47H from NT-MDT. The Solver P47H is versatile, it is designed for qualitative and quantitative measurements of surface characteristics, for example measurements in controlled gas environment, along with sample heating up to 300 °C.

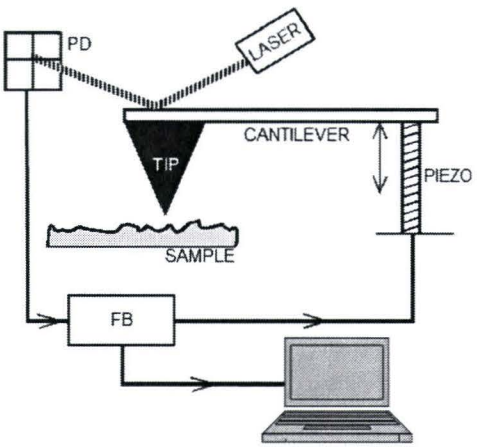

Figure 3.2: *The main components of a scanning probe microscope. The distance between a sharp tip and the sample is measured by the optical detection system (laser and photodetector (PD)). The feedback system (FB) controls this distance by driving a piezo element. The feedback signal is imaged on a PC.*

The core of a scanning force microscope is a flexible cantilever, with a tip mounted on its end, as is schematically represented in Fig. 3.2. During the measurement the deflection signal of this cantilever is used to determine the interaction between the tip and the sample. The AFM uses an optical system to detect the state of the cantilever. A laser is focused at the back of the cantilever and the reflected laser beam is detected with a position

sensitive photodetector (PSD). The photodetector measures the difference in light intensities on its quadrants. The output signal of the photodetector is used as a feedback signal. If the interaction is distance dependent, the feedback signal can be used to measure and control the tip-surface distance by driving a piezo electric element. The feedback system maintains the tip at a constant deflection (to obtain height information) or at a constant height above the sample (to obtain force information). As the tip is raster scanned over the sample, the topography is measured. Except for research of topography of a surface, scanning probe microscopes allow the study of various surface properties: mechanical, electric, magnetic, optical and many others.

3.2 Tip-sample positioning

The used scanning force microscope has the ability to change the relative tip-sample positioning by several means. Two screws are used to change the sample position parallel to the tip, and a driving mechanism moves the sample closer or further away from the tip, with micrometer-scale precision. A piezo-tube scanner is used for positioning of the cantilever with respect to the sample with nanometer-scale precision. During scanning, the non-linearities of the tube scanner are compensated. To simplify the description of the tip-sample positioning, it is assumed that only the tip moves, and the sample is on a fixed position.

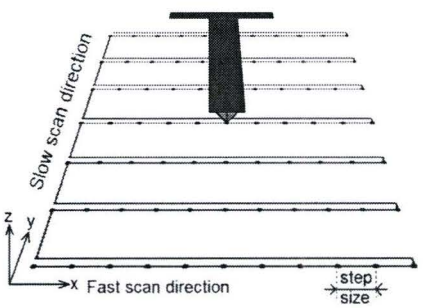

Figure 3.3: *A typical scan pattern. Indicated is the coordinate system and scanner motion during data acquisition. Different step sizes can be selected for the x- and y-direction. The step size and the number of steps determine the scan size.*

Scanning is done in a raster pattern. The tip scans the first line, and moves back. It then steps in the perpendicular (in-plane) direction to the second scan line, scans it and moves back, then to the third line, and so on. (see Fig. 3.3). While the tip is moving across a scan line, the image data is

recorded at equally spaced intervals. The spacing between the data points is called the step size. The step size is determined by the full scan size and the number of data points per line. Data is collected in only one direction, commonly called the fast scan direction. The perpendicular direction, in which the scanner steps from line to line, is called the slow scan direction. A coordinate system can be defined as shown in Fig. 3.3. According to this definition, the fast scan direction in this instrument is usually the x-direction.

The tip-sample distance and movement of the tip in the plane of a sample have to be controlled with high accuracy. This is done with piezo-electric scanning elements. Piezo-electric materials change their sizes in an external electric field. A tubular piezo-electric element as used in most scanning probe microscopes is shown in Fig. 3.4.

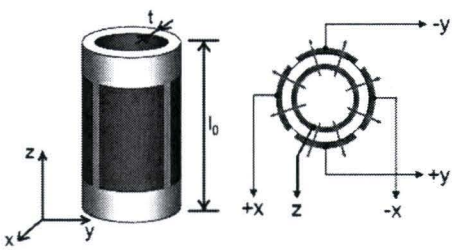

Figure 3.4: *A tubular piezo scanner, consisting of 4 individual outer electrodes and 1 inner electrode. On the right the individual electrodes are shown in top view. Adapted from [47].*

Under the influence of a potential difference V between the inner and outer electrodes, the tube changes its size [47]. The lengthening of the piezo tube is given by:

$$\Delta z = d_{\perp} \frac{l_0}{t} V, \tag{3.1}$$

where $d_{\perp}$ is the perpendicular piezo-electric coefficient, defined by the type of ceramic materials of the tube. The length of the tube in the undeformed state is l_0, and t is the thickness of the tube wall. Thus, at the same applied voltage V, the lengthening of a longer or thinner tube will be more. The external electrode is divided into different sections. Applying a voltage on opposite sections of the x or y electrodes with respect to the internal electrode, reduces or increases the length of that part of the tube. This leads to bending of the tube in the corresponding direction.

The P47H scanner consists of 2 different diameter tubes, one of which is inserted into the other as can be seen in figure 3.5. The lower end of the

large tube is attached to the SPM head, and the upper end attached to the smaller diameter tube. The lower end of the latter is fixed to the cantilever. The smaller diameter piezo-electric tube scans in the plane parallel to the sample surface *(x,y)*, and the larger diameter tube moves the cantilever perpendicular to the surface (z-direction). The maximum scanning area with this setup is 50 micrometer.

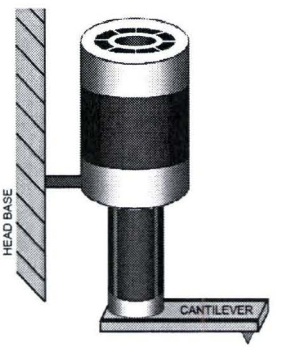

Figure 3.5: *The piezo scanner used in the P47H. The larger diameter tube controls the height of the cantilever, whereas the smaller diameter tube controls the lateral position. The dimensions of the cantilever are exaggerated for clarity.*

3.2.1 Positioning artifacts

Piezo-electric elements are used because they are capable of moving the probe for very small distances. However, the piezo-electric elements move in a nonlinear motion and exhibit hysteresis effects. The shape and position of the piezo-electric scanner relative to the sample can create artifacts in the images.

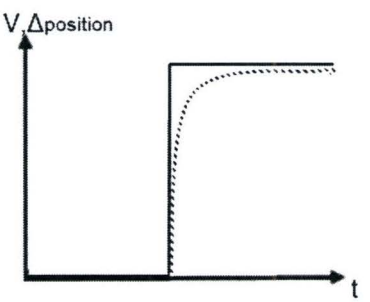

Figure 3.6: *Schematic diagram of voltage change and corresponding shift in scanner position. The solid line corresponds to the applied voltage, and the dashed line shows the reaction of the scanner on the change of the voltage.*

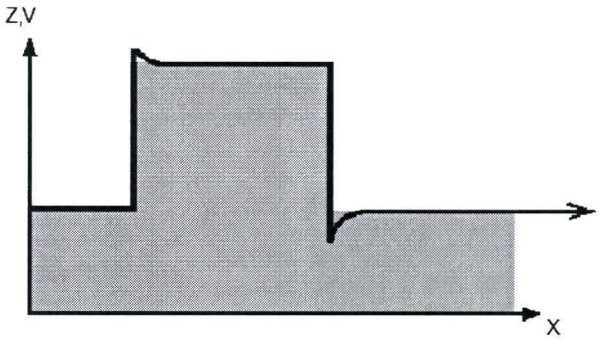

Figure 3.7: *Scan of a step profile, affected by the creep effect. The gray area is the actual step profile. The black line is the voltage that has to be applied to the piezo to keep the tip in contact with the sample.*

A drawback of piezo-elements is the creep delay of a reaction on the change of the control voltage. A time diagram of the voltage change and the corresponding shift in position of the scanner is schematically shown in Fig. 3.6. The response of the scanner (dashed line) is delayed with respect to a step in the voltage (solid line). To examine the effects of creep in the z direction, consider a sample consisting of a step in the z-direction, as shown in Fig. 3.7. As the tip moves up the step (indicated in gray), the scanner contracts immediately with a voltage corresponding to the full step height (the black line). However, the scanner continues to contract slowly due to creep. To keep the tip in contact with the sample, a SPM has to apply a voltage in the other direction, counteracting the creep. When the tip moves down the step, the same process occurs, but in the opposite direction.

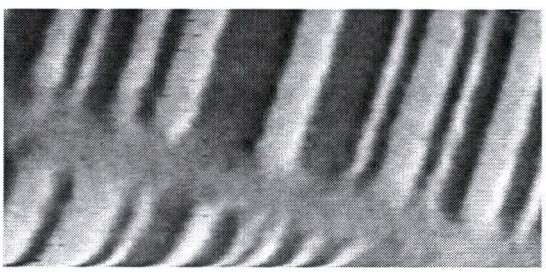

Figure 3.8: *MFM scan of a track pattern from a hard disk sample. The scan size is 11×5 μm. Two rows of bits can be seen, with a spacing in-between. At the beginning of the scan, in the bottom of the image, the creep effect is visible by the distorted bits.*

The creep of the piezo element results in the appearance of geometrical distortions in images due to this effect. This effect is especially noticeable when the scanner is moved to a reference point in the initial stage of the

scanning. Fig. 3.8 shows a MFM measurement of a track pattern from a hard disk sample made with our MFM. To move the scanner to its start position an abrupt change in voltage is applied, and creep will distort the start of the image causing a straight object to appear curved in an image. Usually, this distortion is prevented by restarting the measurement after several scan lines are measured.

Another drawback of piezo elements is hysteresis. Suppose, the voltage is gradually increased to some finite value, and then decreased back to zero. If the length of the piezo is plotted as a function of the applied voltage, the descending curve does not retrace the ascending curve, it follows a different path, as shown in Fig. 3.9. This leads to a situation where the piezo appears

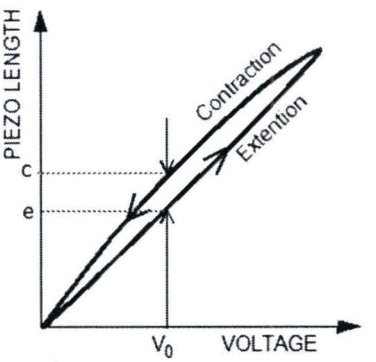

Figure 3.9: *Hysteresis of the piezo-tube. The length of the piezo is different (e and c) at the same voltage V_0, depending on the hysteresis.*

in different positions (e) and (c), with the same voltage V_0, depending on the direction of movement. As mentioned earlier, data are usually collected in one direction to minimize errors caused by scanner hysteresis. Fig. 3.9 shows that data collected in the return direction would be shifted slightly, distorting the measurement grid as shown earlier in Fig. 3.3.

Hysteresis in the direction perpendicular to the plane of the sample (z) causes erroneous step height profiles. It is clear from Fig. 3.9 that if the scanner is going up a step in the z-direction, a certain voltage is required to allow the scanner to contract. But going down the same step will extend the scanner, and extension takes more voltage than contraction for the same displacement as is clear from Fig. 3.9. When the SPM image is represented by the voltage applied to the scanner, a profile of the image would look like Fig. 3.10, where the step in the sample is represented by the gray area, and the applied voltage by the black line. Going up the step requires less voltage ($V_H - V_0$) than going down ($V_H - V_L$).

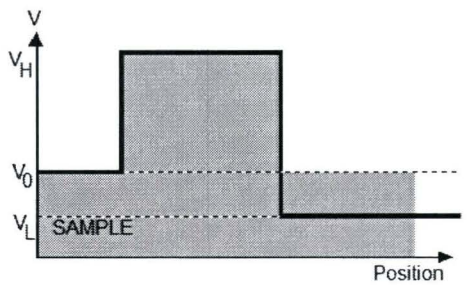

Figure 3.10: *Image of step profile (gray) on a sample. When going up the step the voltage (black line) increases from V_0 to V_H, back down the step the voltage reduces to V_L because of hysteresis.*

The Solver P47H travels a maximum of 50 μm in the x and y directions, as well as 5 μm in the z direction. Note that the end of the scanner, where the cantilever is attached, moves in a curved plane. Non-linear motion of the piezo electric elements causes the probe to move in a curved motion over the surface. Especially for larger scan sizes, deviations from a perfect plane occur, as can be seen in Fig. 3.11, where a calibration sample is imaged with our Solver P47H. This sample consists of equidistant structures of 1.5 μm. This curvature (commonly called bow) can be removed from the image with the aid of computer software.

Figure 3.11: *An AFM scan made with our Solver P47H of a calibration sample consisting of 1.5×1.5 μm squares spaced 1.5 μm apart. The scan size is 14×14 μm. Note that the z-scale is exaggerated, the height of the squares is only 20 nm.*

3.3 Probes

A crucial part of the scanning force microscope is the probe. The probe consists of a sharp tip mounted on a flexible cantilever. Fig. 3.12[2] shows an

[2]The images are made with a Philips XL 30 SEM, located at the multi-scale lab of the Computational and Experimental Mechanics (CEM) group of the department of mechan-

image of a cantilever. One end of the cantilever is fixed on the silicon base, while on the other end the tip is located. On the right side of Fig. 3.12 a zoom at the end of the tip can be seen.

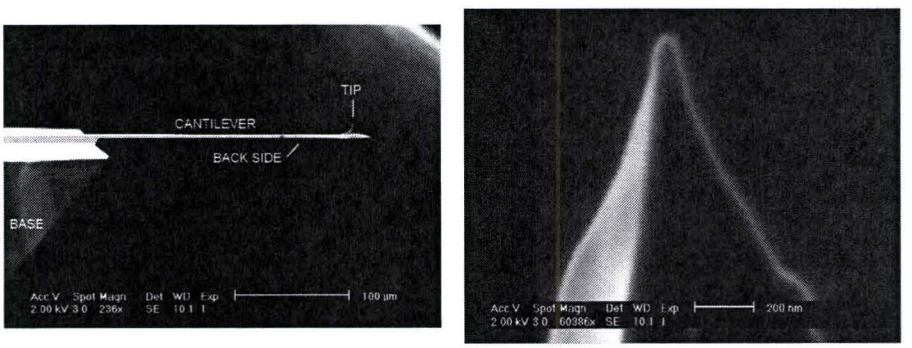

Figure 3.12: *Scanning electron microscopy images of a typical cantilever (left). At the left side of the cantilever, the large base can be seen and on the right side the tip. A zoom of the tip can be seen in the right image.*

Most cantilevers are microfabricated from silicon or silicon-nitride, using lithographic techniques. Batch fabrication ensures that large numbers of almost identical cantilevers are available with the same spring constant and resonant frequency. Usually, the back side of the cantilever is coated with aluminum to obtain sufficient reflection for the deflection detection.

3.3.1 Atomic force microscopy cantilevers

In general, an AFM probe should meet two requirements for optimum performance:

1. The cantilever should be sensitive to small forces i.e. large deflection for a small force. According to Hooke's law (equation (2.3)), it is desirable to have a low spring constant to perform sensitive force measurements. Thus soft cantilevers have better sensitivity, but are more susceptible to being snapped into the sample when the force (gradient) exceeds the cantilever spring constant (see eq. 2.12). For AFM, imaging forces are typically in the range of 0.1 to 100 nN. Therefore, the spring constant k of the cantilever should be small. For example, if $k = 1$ Nm^{-1}, then a force of 0.1 nN will deflect the cantilever by 0.1 nm according to Hooke's law (Eq. 2.3), which can be detected with the optical detection technique (Section 3.4).

ical engineering from the Eindhoven University of Technology.

2. The cantilever should be insensitive to external vibrations. Vibrations such as movements of a building or table generally have low frequencies in the 1-100 Hz range. Coupling to the cantilever is less effective when it has a high resonance frequency, far away from the excitation frequency. A high resonance frequency also results in a fast response during scanning, and therefore, a high imaging speed. A maximum resonance frequency (eq. (2.5)) and minimal vibrational sensitivity (eq. (2.31)) is obtained for a large spring constant.

The spring constant k of a cantilever shaped as a rectangular bar [23] is:

$$k = \frac{Ewd^3}{4l^3}, \tag{3.2}$$

where w, d and l are the width, thickness and length of the cantilever, respectively, and E is Young's modulus of the cantilever material (for Si: $E = 1.25 \cdot 10^{11}$ Nm^{-2}). The free resonance frequency of the same cantilever is:

$$\omega_0 = 0.162\sqrt{\frac{E}{\rho}}\frac{d}{l^2}, \tag{3.3}$$

where ρ is the density of the material (for Si: $\rho = 2.3 \cdot 10^3$ kgm^{-3}). The ratio ω_0/k is:

$$\frac{\omega_0}{k} = 0.648\frac{1}{\sqrt{E\rho}}\frac{l}{wd^2}. \tag{3.4}$$

The two requirements above (small spring constant k, and high resonance frequency ω_0) are achieved at a high ratio ω_0/k. This requirement is fulfilled by minimizing the cantilever dimensions, e.g. by making it relatively long (large l) and slender (small d). For a cantilever with typical length of 100 μm, and thickness of 1 μm, the spring constant is according to eq. (3.2) in the order of 0.1-1 Nm^{-1}. With these dimensions cantilevers with resonant frequencies in the order of 10-100 kHz are obtained.

3.3.2 Magnetic force microscopy cantilevers

The force sensor plays an important role in the quality of MFM measurements. The MFM sensor consists of a magnetic tip, mounted on a cantilever. Previously, sensors have been made from fine, electrochemically etched, ferromagnetic wires, usually of cobalt or nickel [29, 35]. Nowadays, AFM cantilevers with integrated sharp tips are coated with a thin layer of magnetic material. Magnetic thin film tips have the advantage of having a reduced stray field as compared to bulk wire tips [48]. Another advantage of thin

film tips is that their magnetic properties can be controlled by choosing the appropriate coating material [49, 48, 50]. Due to coating of the tips, a pattern of magnetic domains will form, which reduces the effective magnetic moment of the tip. The exact domain structure is not known, and can change during MFM measurements.

In this thesis, probes produced by Nanosensors[3] (type MFMR) were generally used. The specifications are summarized in Table 3.1. Figure 3.13 shows a scanning electron microscope image of a similar type of probe, with indications of the various dimensions. The integrated tips are $10 - 15\mu$m high and have a typical tip radius < 50 nm.

Cantilever thickness d	3 μm
Mean width w	28 μm
Length l	225 μm
Spring constant k	2.8 Nm^{-1}
Resonance frequency ω_0	75 kHz

Table 3.1: *Specifications of MFMR probes, as provided by Nanosensors.*

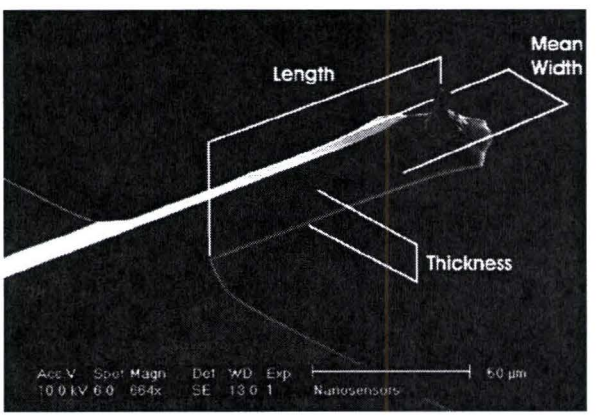

Figure 3.13: *SEM image of a cantilever from Nanosensors, with indications of the various dimensions.*

The force sensors are coated with a thin ferromagnetic film to make them magnetically active. Different coatings are used. Standard Nanosensors cantilevers have an approximately 40 nm thick cobalt alloy coating on the tip side. The coating is characterized by a coercivity of approximately $2.4 \cdot 10^4$ A/m (corresponding to 30 mT) and a magnetic moment of approximately $5 \cdot 10^{-6}$ Am^2. The tips are magnetized, approximately in the

[3] www.nanosensors.com

direction perpendicular to the cantilever axis by placing a permanent magnet near the tip end, before the tip is used.

Some special requirements are needed for the magnetic tip:

1. The spatial resolution is related to the magnetized part of the probe exposed to the sample stray field (Eq. 2.22). Therefore, to improve resolution it is necessary to reduce the effective magnetic volume. Ideally the effective volume would consist of a small single domain ferromagnetic particle located at the tip apex. So-called supertips have been developed based on this idea [34].

2. A strong signal produced by a small effective volume requires the total magnetic moment to be large. Material with high saturation magnetization (like CoFe) should be used to limit the required volume.

3. The magnetic anisotropy and coercivity of the tip should be large to minimize the influence of the stray field of the sample on the tip.

It is clear that not all above requirements can be satisfied together. For example, there is a trade-off between a small magnetic tip volume and a large total moment. Three parameters can be varied in this optimization: the shape of the non-magnetic tip, the material of the magnetic coating, and the thickness of the coating. Imaging in the presence of external magnetic fields requires tips either having coercivity far beyond that of the sample (so that the applied field does not affect the tip), or far below it (so that the tip moment is always aligned with applied field).

To control the magnetic moment of the probe, standard AFM tips from NT-MDT are coated with magnetic material. Sputter deposition of magnetic material on the tip is performed with CARUSO[4]. Different materials at various thicknesses can be used to tune the magnetic moment. Cantilevers are coated by sputter deposition with approximately 40 nm CoFe. A protective layer of 5 nm Ta is applied to protect the magnetic layer from oxidation.

Fig. 3.14 shows two MFM scans of a hard disk sample. The coated AFM tip shows a maximum phase shift of 0.3 degrees, whereas the Nanosensors MFM tip shows a maximum phase shift of 6 degrees. From this result, it seems possible to fabricate MFM tips by coating standard AFM tips, but the signal is much smaller than Nanosensors MFM tips. Possible improvements in signal could be obtained by deposition of a thicker layer of magnetic material to enlarge the total magnetic moment. However, this will possibly

[4]CARUSO is a computer controlled sputter coater available at the group FNA.

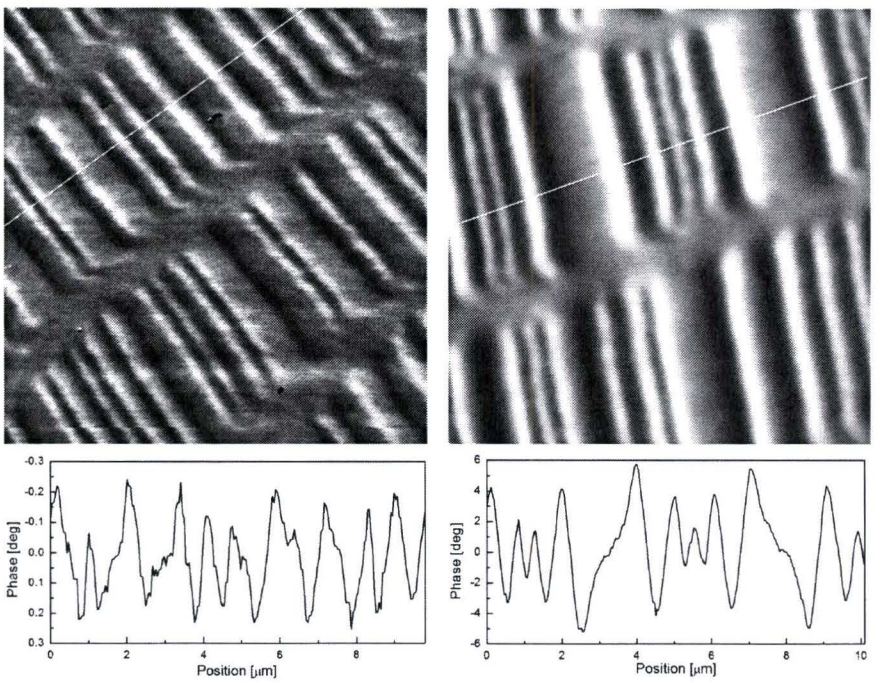

Figure 3.14: *MFM images of Hard disk bits. (a) Tip coated with CoFe at FNA. A maximum phase shift of 0.3 degrees is seen. (b) The Nanosensors tip is coated with Co and has a maximum phase shift of 6 degrees.*

reduce the spatial resolution because the tip radius will increase. The details of the phase shift and spatial resolution of home-made MFM tips, will be further investigated in future experiments. In this thesis, the Nanosensors MFM tips are used to perform the measurements.

3.3.3 Probe artifacts

Images from AFM or MFM measurements are always a convolution of the tip and sample geometry. The size, shape and sharpness of the tip play an important role in image formation. The tip should have a small aspect ratio (ratio of width to length) to resolve small features. The measured size of surface features (e.g. particles) is larger than their real size when the radius of the tip is too large (Fig. 3.15 A). The side of the probe will cause the width (A_0) of an object to look broader (A_m), whereas the height of the feature is usually correct. In the same way, features in the surface (Fig. 3.15

B), like holes (with width w_0) can appear too small (w_m). Moreover, the depth is not correctly measured (Fig. 3.15 C) because, due to the width of the tip with respect to the sample features, the tip reaches a depth h_m from the top of the structures instead of h_0. It is still possible to measure the width of features or the pitch of repeating objects with this tip. Features on the surface much smaller than the tip reflect the shape of the tip rather than their own geometry. If the tip is much smaller then the features to be measured, the probe artifacts will be minimal and the images will be relative accurate.

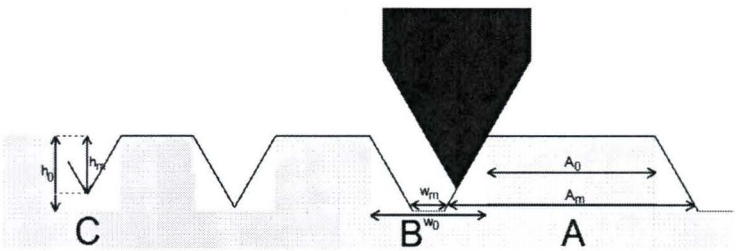

Figure 3.15: *Convolution of tip and sample. (A) The size (A_0) of sample features appears larger (A_m) if scanned with a large tip. (B) Holes with width w_0, appear to have a smaller width w_m. (C) The depth h_0 is not correctly measured (instead h_m is measured).*

A contaminated or broken tip can have its own geometry superimposed on the surface topography. This creates images that do not reflect the sample surface or features correctly. Fig. 3.16 (left) shows a SEM[5] image of a contaminated tip. Comparison of this tip with the tip in Fig. 3.12 clearly shows contamination on the left side of this tip (indicated with the dashed line). Also the tip in Fig. 3.12 is much sharper. On the right an AFM scan can be seen, made with a contaminated tip, of gold particles deposited on sapphire. The inset shows the same sample (but at a different lateral position) imaged with a fresh tip. In the inset the gold particles appear as small round particles. In the main image, the gold particles appear as small spheres with a larger sphere around it.

3.4 Detection system

As the tip scans the sample, the cantilever bends while the tip moves up and down with the topography of the surface. Several different methods for detecting the cantilever deflection can be used.

[5]Philips XL 30 SEM, located at TU/e.

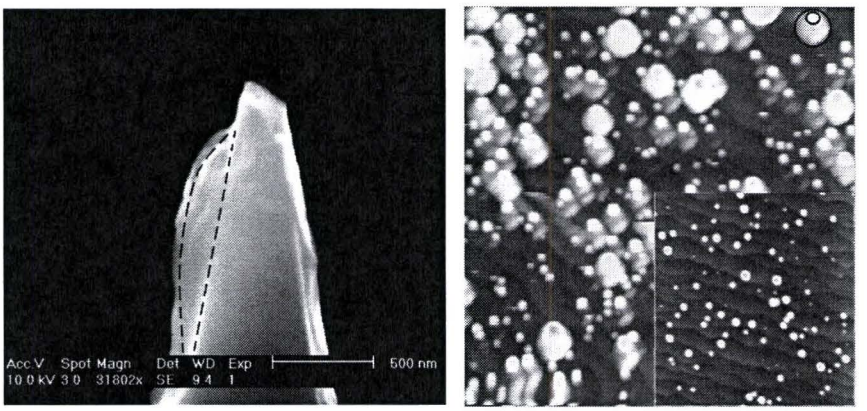

Figure 3.16: *A SEM image of a contaminated tip (left). The dashed line indicates the large contamination. On the right is a measurement with a contaminated tip of a sapphire sample covered with gold particles. The gold particles are not imaged correctly; they appear as small spheres, with a larger sphere around it, but shifted down in position. This is indicated by the dashed circles in the top right corner of the image. The inset shows a measurement with a fresh tip, where the gold particles appear as small spheres. Scan sizes of both images are 3×3 μm.*

In the early scanning force microscopes, electron tunneling between the back of the AFM cantilever and an STM tip located behind the AFM cantilever, was used to detect the cantilever deflection [18]. The disadvantage of using a tunneling sensor is that the cantilever has to be conducting and needs a smooth surface to form a good junction. The tunneling current is extremely sensitive to the surface conditions of the cantilever. The surface roughness on the rear side of the cantilever may influence the measurements when the focus point of the STM tip on the cantilever changes. Cantilever deflection is restricted in tunneling detection, unless a servo system has to be used to follow the cantilever.

Most scanning force microscopes nowadays use an optical detection system to detect the deflection of the cantilever. Optical detection has several advantages over tunneling detection. It is more reliable because the cantilever does not have to be conducting and a good tunnel junction is not needed. The cantilever does not experience a noticeable force from the optical detection system, and the cantilever has a large dynamic range compared to tunneling. With optical detection, a semiconductor laser (in the case of the Solver P47H: $\lambda = 670$nm, $P = 0.9$mW) is focused on the end of the cantilever. The reflected signal is detected with a four-quadrant photodetector (PSD) as can be seen in figure 3.17. As the tip scans the surface of a sample, moving up and down with the surface topography, each angular displacement of the tip is amplified in the movement of the reflected laser

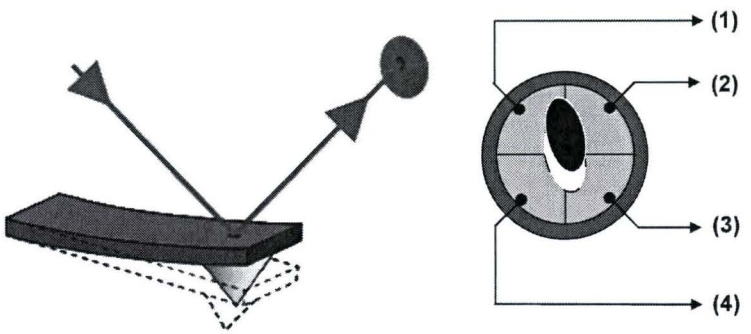

Figure 3.17: *Optical detection of a bend of the cantilever. The reflected laserbeam is detected with a position sensitive photodetector (PSD). Adapted from [47].*

beam. The optical system can detect angular deflection of the cantilever to an accuracy of less than 10^{-4} degree [51], giving a vertical resolution of 0.05 nm.

Deflection of the cantilever results in a shift of the laser spot with respect to the segments (1,2,3,4) of the photodiode, which, in its turn, results in changes of electrical signals arriving from those segments. Signals are pre-processed (amplified, appended and deducted) and three signals arrive at the output of the detection system:

$$\Delta_{VER} = (1+2)-(3+4), \tag{3.5a}$$

$$\Delta_{LAT} = (1+4)-(2+3), \tag{3.5b}$$

$$\Sigma_{LASER} = 1+2+3+4, \tag{3.5c}$$

The Δ_{VER} signal is the difference between the upper and lower halves of the photodiode, and is proportional to the vertical cantilever deviation. The Δ_{LAT} signal is proportional to the lateral cantilever deviation, and the Σ_{LASER} signal is proportional to the total intensity of the laser light falling on the photodiode. The output of the photodetector is used by the feedback system to maintain the probe system at a constant signal. An optical tracking system ensures that the laser spot does not move with respect to the cantilever during scanning.

3.5 External magnetic field

One of the goals of the present study is to perform MFM measurements dependent on an external magnetic field. For this purpose, a new sample stage

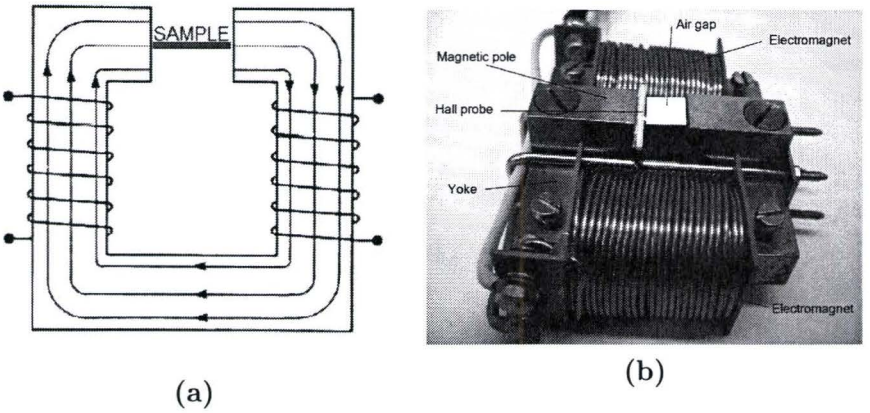

Figure 3.18: *Design of the electromagnet. On the left a schematic overview of the electromagnet is presented. The outer dimensions of the yoke are 5×5 cm, and the gap width is 1 cm. .The right image shows a photo of the electromagnet. The sample is mounted at the center of the air gap.*

is designed for the Solver P47H microscope. Fig. 3.18(a) shows a schematic illustration of the stage. Fig. 3.18(b) provides a photo of the real stage. The magnetic field is generated by a two small cylindrical electromagnets (coils), which are placed on either side of the sample. By using a yoke, which penetrates the coils, the magnetic flux is efficiently guided to the poles, where a gap of 1 cm is used to position the sample. The poles are made removable to change the width of the air gap. The magnetic field is measured with a calibrated hall probe, placed between the poles. The maximum continuous applied field is 120 mT at an air gap of 1 cm. Adjustment of the field strength is performed by changing the voltage from the attached power supply. It is easy to change polarity of the electromagnet i.e. both positive and negative magnetic fields can be applied to a sample. The control of the applied field strength can be improved by controlling and monitoring the applied magnetic field with a computer.

YIG

To illustrate the successful implementation of the new sample stage, measurements on an Yttrium Iron garnet (YIG) are performed. YIG is supposed to be divided into perpendicular magnetized domains, as seen in Fig. 3.19. The transition between two domains, in which the magnetization has different directions, is called a domain wall. Within the wall, the magnetization direction rotates from that in one domain to that in the other domain.

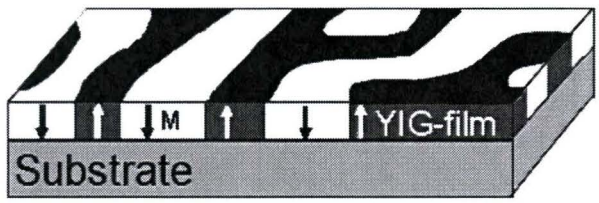

Figure 3.19: *Schematic representation of the domain pattern in a YIG sample. Scan size is 30×30 μm.*

Without applied magnetic field the distribution of the domains is random, but the magnetization of the entire sample is approximately zero. Application of an external magnetic field will change the domain pattern. Fig. 3.20 shows the expected behavior of two oppositely magnetized domains for perpendicular and in-plane applied fields, neglecting interactions of the domain wall with the applied field.

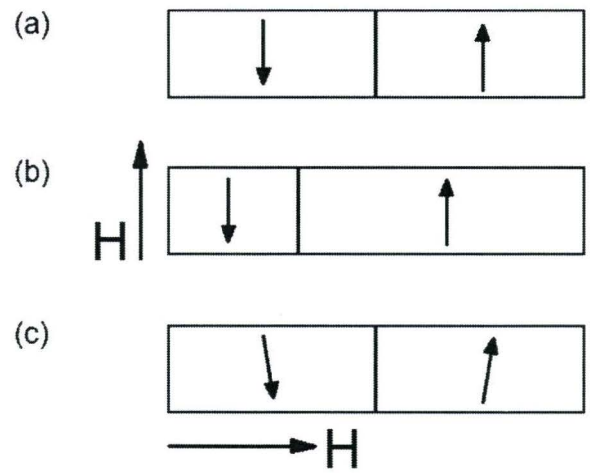

Figure 3.20: *Side view of two magnetic domains. The arrows indicate the magnetization direction of the domains. (a) Situation at zero applied field when the width of both domains is equal. (b) At a perpendicular applied magnetic field the width of the domain with the same magnetization direction as the applied field will increase at the cost of the width of the opposite directed domain. (c) An in-plane magnetic field will cause the magnetization to rotate in the direction of the applied field.*

At zero applied field (Fig. 3.20(a)) the width of both domains is equal, and the magnetization direction is perpendicular to the sample surface. Application of a perpendicular magnetic field (b) will affect the width of the domains. Domains where the magnetization is in the same direction as the applied field are energetically favorable (the width will increase) with re-

spect to domains where the magnetization is opposite to the applied field direction (the width will decrease). A field applied in-plane to the sample surface (c) will influence the directions of the magnetization in the domains (the magnetization will rotate in the direction of the applied field), but the width of the domains will not be affected. This effect is expected to be small and not noticeable with MFM. However, an in-plane applied magnetic field will have effect on the domain walls. Rotation of the magnetization direction in the domain wall, will result in an in-plane magnetization component. The applied magnetic field will induce a torque on the domain wall, which will try to align the domain wall with the applied field direction, as can be seen in Fig. 3.21.

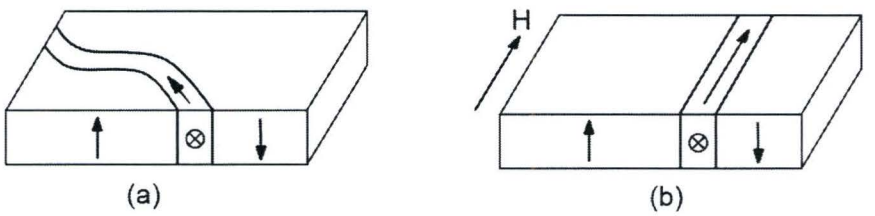

Figure 3.21: *Two magnetic domains, separated by a domain wall. The arrows indicate the magnetization direction. (a) At zero applied field direction of the domain wall is random. (b) An in-plane magnetic field will cause the domain wall align with the direction of the applied field.*

MFM measurements on YIG are shown in Fig. 3.22, (a) shows the topography, and (b)–(f) show MFM images. The surface is relative flat except for some contamination (white spots), which is probably dust. An MFM scan made at zero applied field is shown in (b), where a random orientation of the magnetic domains can be seen. The black/white contrast seen in the vicinity of the domain wall (see the indicated area in Fig. 3.22(b)) is in agreement with the expected contrast discussed in paragraph 2.2.2. Application of an in-plane magnetic field indicated in (c),(e) and (f), show a changed direction of the domains as expected due to the effect of the applied field on the domain wall. The width of the domains is also changed. This can be due to the fact that our applied field is not uniform in-plane of the sample, but also has a small component perpendicular to the sample surface. The width of several domains is indicated in the figure. Defining the width ratio as the width of the wide domain divided by the width of the narrow domain, a ratio of approximately 2.0 is found at a field of -10 mT (e) and a ratio of 3.0 at -20 mT (f). From this, it seems that the ratio depends on the magnitude of the applied field, as expected for the increasing perpendicular component of the magnetic field.

The direction of the domains, at an applied field of $+20$ mT in (c), is not

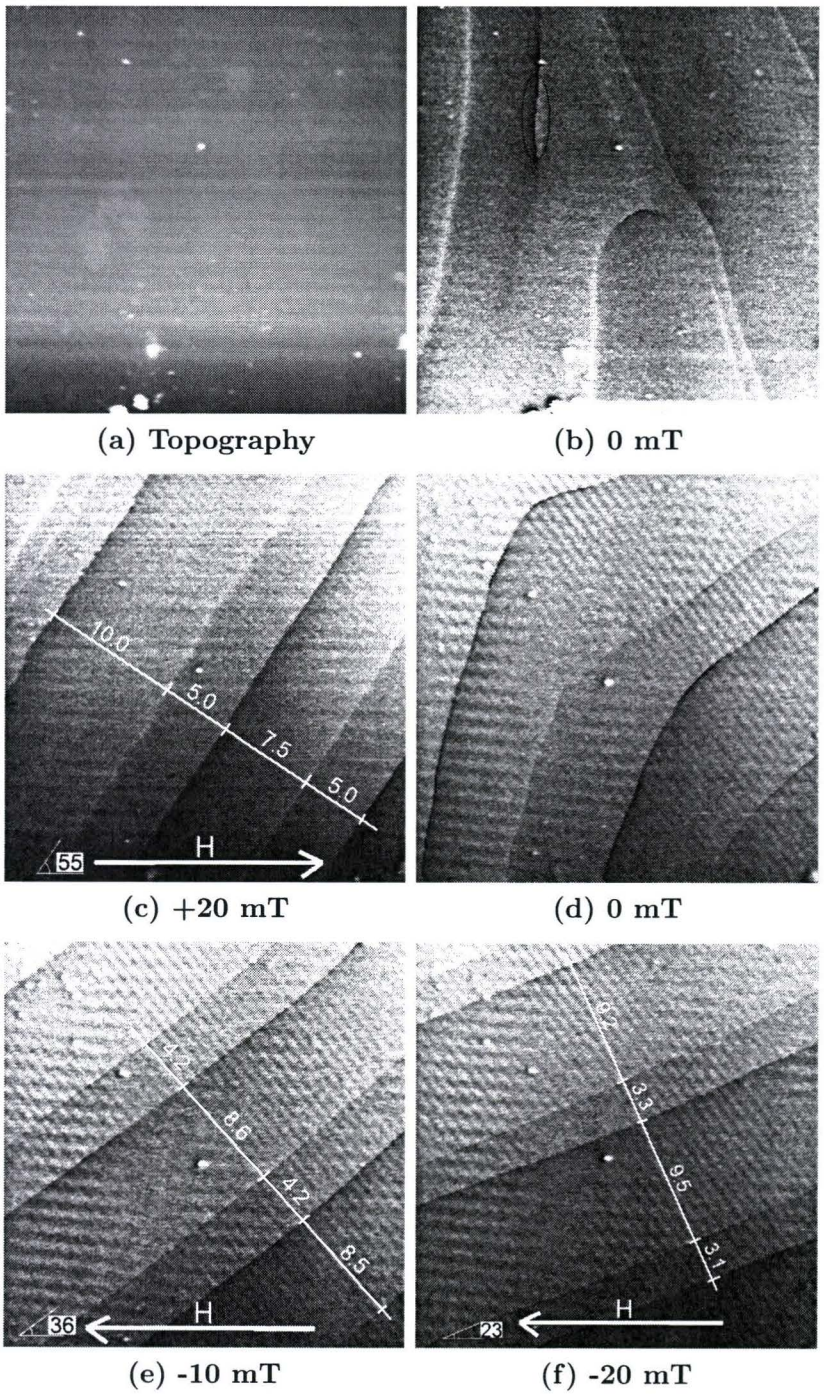

(a) Topography (b) 0 mT

(c) +20 mT (d) 0 mT

(e) -10 mT (f) -20 mT

Figure 3.22: *MFM image of YIG garnet. (a) Topography, and (b) trough (f) MFM scans at applied fields indicated in the figures. Scan sizes are 30×30 μm.*

the same as at an applied field of -20 mT, in (f). The angle between the magnetic field direction and the domain wall direction in (c) is approximately 55°, whereas the angle in (f) is approximately 23°. This can be explained by a n in-plane contribution to the anisotropy of the sample.

Although the interpretation of these first MFM images of YIG is still rather underdeveloped, and probably requires more detailed experiments for a variable field under several angles with the sample, it is clearly demonstrated that the presence of the implemented magnetic field can be monitored in these MFM images. Other results on the field-dependence of MFM will be postponed for the following chapter, focusing on structured samples in the field of spintronics.

Chapter 4

MFM on structured magnetic samples

This chapter will discuss the results of the measurements that have been performed on magnetic samples with the MFM setup described in the previous chapter. The goal of these measurements is to show the usefulness of magnetic force microscopy at studying small magnetic elements. This will be done on the basis of three technologically interesting subjects:

- Magnetic read only memory (MROM),
- Magnetic random access memory (MRAM),
- Spin injection and detection in semiconductors (GaAs).

Measurements are performed on samples containing small structured elements. First, it will be shown that magnetic domain imaging is possible with MFM for these particular structures. Next, MFM imaging in the presence of an external field is used to show the influence of the field on the magnetization. Especially for the spin injection devices, magnetization switching is investigated as a function of the width of the structures. For this study, a theoretical background is required to understand the physics of magnetization reversal in some detail. An introduction to this area follows in section 4.1, followed by the actual experimental results in the subsequent paragraphs.

4.1 Magnetization switching

There are several models that describe switching of magnetization of small magnetic elements. The magnetization can be determined by minimizing the total free energy [52]. Starting from an ellipsoidal particle with *uniaxial* anisotropy, the total free energy density

$$E_t = E_{ex} + E_K + E_d + E_H, \tag{4.1}$$

is composed of exchange, anisotropy, demagnetizing and magnetostatic energy, respectively. In a first order approximation, E_t depends only on the angle ϕ between the magnetization, $\boldsymbol{M}$, and the *easy* axis. The equilibrium position for ϕ follows from a minimization of E_t with respect to ϕ. Above a critical size, the energy can be minimized by forming multiple domains in which the magnetic moments are aligned. Below this critical size the particles remain in a single domain state. In the absence of domain boundaries, changes of magnetization cannot proceed by boundary displacement, but must proceed by rotation of the magnetic moment. The most common magnetization reversal models in the single-domain state are the Stoner-Wohlfarth (SW) model [53] and the curling (C) model [52], as shown in Fig. 4.1. These models will be further explained below.

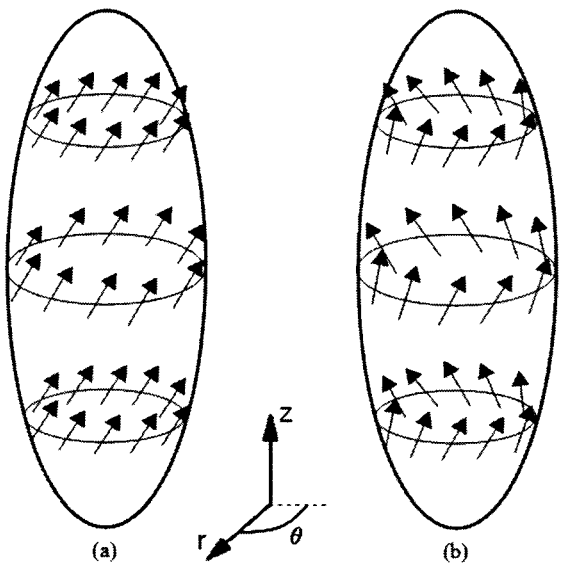

Figure 4.1: *The two different magnetization reversal models for an ellipsoid, defined in cylindrical coordinates (r, θ, z). (a) The SW-model, all magnetic moments remain parallel. (b) The C-model, the magnetic moments reduce the demagnetizing field in the hard axis direction.*

4.1.1 SW-model

In the Stoner-Wohlfarth model, the magnetization is considered constant in magnitude, and all the magnetic moments remain parallel to each other (see Fig. 4.1). Therefore, the SW-model is characterized by a constant exchange energy.

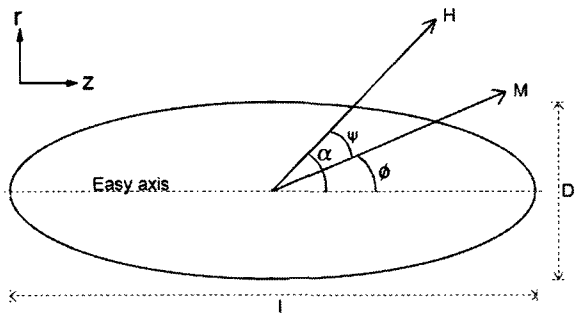

Figure 4.2: *Definition of the geometry in the switching models. Elliptical particle (with length l and diameter D) with easy axis as the z-axis of a Cartesian coordinate system. The applied magnetic field is at an angle α with the easy axis, and the magnetization vector with an angle ϕ.*

Consider an ellipsoid particle with easy axis taken as the z-axis in a cylindrical coordinate system. The rotation takes place in the (r, z)-plane, and is described by the rotation angle ϕ (see Fig. 4.2). In the absence of an applied field, the magnetic moments tend to align along the easy axis. During the reversal process, the demagnetization energy increases, because the magnetic moments rotate away from the easy axis, thereby increasing the magnetization component along the hard axis. In the SW-model, the demagnetizing field components are

$$H_{d,x} = -N_\perp M_s \sin\phi, \qquad H_{d,z} = -N_\parallel M_s \cos\phi, \tag{4.2}$$

with the demagnetization factors $N_\perp$ and $N_\parallel$ for magnetization perpendicular and parallel to the easy axis. The demagnetization factors depend only on the geometry of the ellipsoid, and are defined in Appendix A. The total energy density (apart from constant terms) is now given by:

$$E_t = K\sin^2\phi + \frac{1}{2}\mu_0 N_\perp M_s^2 \sin^2\phi + \frac{1}{2}\mu_0 N_\parallel M_s^2 \cos^2\phi - \mu_0 H M_s \cos(\alpha - \phi), \tag{4.3}$$

where α is the angle between the easy axis and the applied field $\boldsymbol{H}$, and K the crystallographic anisotropy (here assumed to be of uniaxial nature). Starting in the situation where the magnetization is saturated along the easy axis, $\phi = 0$, the field $\boldsymbol{H}$ is applied parallel to the easy axis with angle $\alpha = \pi$

(opposite to $\boldsymbol{M}$). Variation of the energy leads to the following equilibrium condition:

$$K \sin 2\phi + \frac{1}{2}\mu_0 M_s^2 (N_\perp - N_\parallel) \sin 2\phi - \mu_0 H M_s \sin \phi = 0. \tag{4.4}$$

Equation 4.4 has a trivial solution $\phi = 0$ for $|H| < H_s$, as indicated in Fig. 4.3, where H_s is given by:

$$H_s = \frac{2K}{\mu_0 M_s} + (N_\perp - N_\parallel) M_s. \tag{4.5}$$

The switch field, H_s, increases linear with increasing crystallographic anisotropy, K, and depends on the geometry by the demagnetization factors $N_\perp$ and $N_\parallel$. At $|H| = H_s$ the magnetization switches to the opposite direction, $\phi = \pi$, see Fig. 4.3.

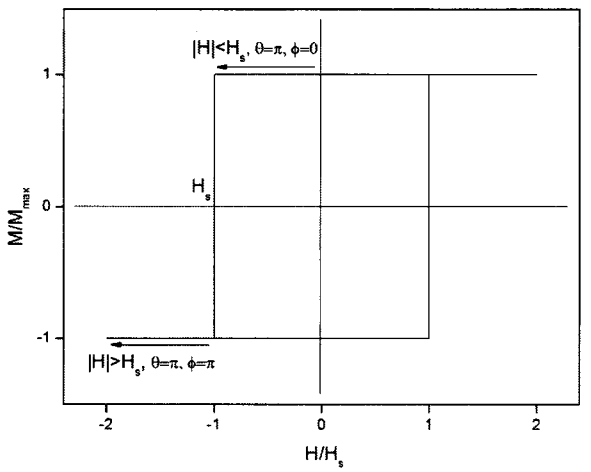

Figure 4.3: *SW magnetization curve. At $|H| = H_s$ the magnetization switches from $\phi = 0$ to $\phi = \pi$.*

4.1.2 C-model

In the ideal curling model, neighboring moments are not necessarily aligned. This allows for configurations with a vanishing demagnetizing field along the hard axis, as in Fig. 4.1(b). For an ellipsoid defined in cylindrical coordinates (r, θ, z), the angle between the spin direction and the easy axis is independent of z and θ, and is a function of r alone [52]. In the curling mode only exchange, crystallographic and magnetostatic energies have to be considered. The switching field is found to be [54]:

$$H_s = \frac{2K}{\mu_0 M_s} - N_\parallel M_s + \frac{8Aq^2}{\mu_0 M_s} \frac{1}{D^2}, \tag{4.6}$$

where A is the exchange stiffness constant, and D is the diameter of the ellipsoid (see Fig. 4.2). The parameter q^2 is a monotonically decreasing function of the aspect ratio, $m = l/D$. The function q is plotted in [55] in the form $k = q^2/\pi$. For aspect ratios of $m = 20$ (which is typical for the structures used in this thesis), the value of $k = 1.1$ ($q = 1.84$). The last term in eq. 4.6 results from the exchange energy of the inhomogeneous magnetization which decreases with $1/D^2$. Equation 4.6 is only valid for positive values of H_s. Negative values of H_s have no physical significance as the switch field is zero in this case [52].

At small diameters the switch field of the C-model exceeds that of the SW-model due to the $1/D^2$ term. Since the smallest switching field always governs the reversal, the SW-model determines the magnetization reversal at small diameters. Above a critical diameter, D_{crit}, the SW-model is replaced with the C-model. Comparison of eq. (4.5) and eq. (4.6) then gives

$$D_{\text{crit}} = \frac{2q}{M_s}\sqrt{\frac{2A}{\mu_0 N_\perp}}. \tag{4.7}$$

For typical material parameters for Co ($M_s = 1.4 \cdot 10^6$ A/m, and $A = 30 \cdot 10^{-12}$ J/m), and a structure with $m = l/D \approx 20$, which gives $N_\perp \approx \frac{1}{2}$, and $q = 1.84$, the critical diameter is found to be $D_{\text{crit}} \approx 26$ nm, above which the C model is dominant.

4.1.3 Domain formation

The single domain state as discussed in the previous paragraph is stable up to a critical diameter, D_{SD}. As the size of the particle increases, the demagnetizing energy E_d also increases (which depends on the width of the particle, see eq. 4.2). Formation of multiple domains (see Fig. 4.4) effectively decreases this width with a factor α, where α is roughly $1/N$, and N is the number of domains formed. Therefore, the energy also reduces by a factor α. On the other hand, domain formation introduces an extra energy term due to the formation of a domain wall. Comparison of the energies of the single domain and the multi-domain magnetization states results in a critical diameter [54]:

$$D_{SD} = \frac{12\sqrt{AK}}{N_{\|}(1-\alpha)\mu_0 M_s^2}. \tag{4.8}$$

To estimate the minimal critical diameter, two domains ($\alpha = 1/2$) are assumed, $N_{\|} = 10^{-2}$ ($m = l/D \approx 20$), and for Co: $K = 4 \cdot 10^5$ J/m^3, and the other parameters as above. The critical diameter for the single domain state $D_{SD} \approx 3\mu$m.

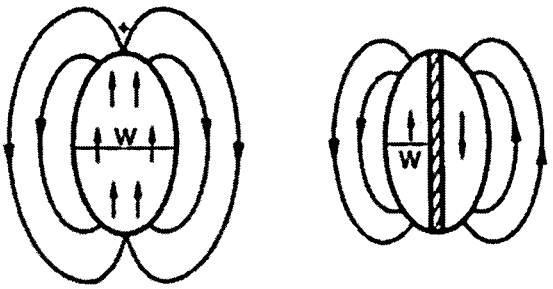

Figure 4.4: *Domain formation in a ellips. The effective width w, and the stray field, is reduced by forming multiple domains. Adapted from [54].*

In multi-domain systems, domain wall displacement will govern the magnetization switching. The simplest case is nucleation of a domain wall (DW) at one end of the sample and its propagation along the sample. Once a domain wall is formed, its propagation through the sample is energetically favorable (it lowers the magnetostatic energy), as long as there are no strong pinning centers. Recent MFM studies of 1 μm wide iron and permalloy (NiFe) wires seem to indicate that in these wires a complex multi-domain structure is formed during switching [56, 57]. Generally, it is very difficult to predict the switching field, but as can be seen in Fig. 4.5, the switching field of multi-domain configurations is generally lower than in the single domain state.

Figure 4.5 reviews H_s for different models. Starting at very small particle diameters, the switch field breaks down because the magnetization becomes unstable when the thermal energy is larger than the anisotropy energy (proportional to the volume of the sample). This is called the superparamagnetic state, where the magnetic moment behaves paramagnetic, strongly fluctuating in time. In the single domain state, for diameters large enough to suppress superparamagnetism, the SW model determines switching up to a critical diameter, D_{crit}. According to eq. 4.5, the magnitude of the SW field is $2K/\mu_0 M_s + (N_\perp - N_\parallel)M_s$. In this example $N_\perp$ and $N_\parallel$ are presumed constant (not dependent on the diameter). Above the critical diameter, D_{crit}, the C model dominates. For increasing particle diameter, the switch field approaches $2K/\mu_0 M_s - N_\parallel M_s$ according to eq. 4.6. In the multi-domain state, when the diameter becomes larger than D_{SD} (eq. 4.8), the switching field is lower than in the single domain state, due to magnetization switching by domain wall displacement.

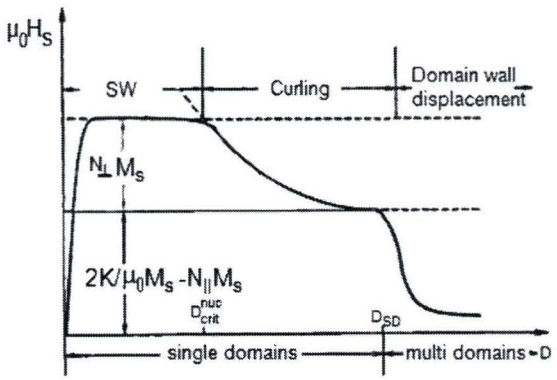

Figure 4.5: *Review of the switch field, H_s, as a function of the width of the particles. Adapted from [54].*

Micromagnetic simulations

To gain more insight into magnetization switching of small magnetic objects, micromagnetic simulations can be used. The Object Oriented Micro Magnetic Framework (OOMMF) is a public domain micromagnetics package, developed at NIST[1]. Inputs such as the material geometry, the initial magnetization, and the time evolution of the external magnetic field have to be supplied. It is also necessary to specify material parameters such as saturation magnetization, the exchange stiffness, and anisotropy constant.

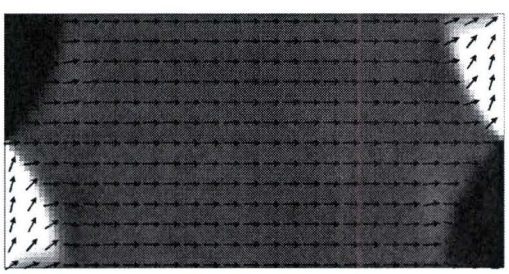

Figure 4.6: *Simulation of a 1×2 μm permalloy rectangle, the arrows and gray scale indicate the magnetization direction.*

The sample is divided into a number of small cells. The behavior of the magnetization is then calculated based on the response of the magnetization in each cell to the local field, consisting of the applied field, exchange interactions with the magnetization in neighboring cells, local anisotropy, and dipolar interactions. For calculations of quasi-static behavior the low-

[1]Website: http://math.nist.gov/oommf/

est energy configuration of the magnetization in a given applied field, or field range, is calculated. Fig. 4.6 shows an example of an OOMMF simulation. The magnetization of a 1×2 μm permalloy rectangle (20 nm thick) is simulated at remanence, after saturation in the long direction. The sample is divided into cells with dimensions of 20×20×20 nm. It can be seen that the sample is almost uniformly magnetized to the right (indicated by the arrows), except for the regions at the edges, here domains are formed where the magnetization is rotated.

4.2 MROM

Magnetic read only memory (MROM) combines the advantages of optical and solid-state storage [58, 59]. Optical storage has the advantage that the read mechanism and the data carrier are separate devices (e.g. CD or DVD). The expensive read mechanism can be combined with many cheap data carriers. Solid-state storage is robust and has high data rates. By separating the solid-state reader from the information carrier, MROM is robust, has a high data rate, low power consumption, and a removable data carrier. In MROM, the data is stored on a (read-only) data carrier, in a

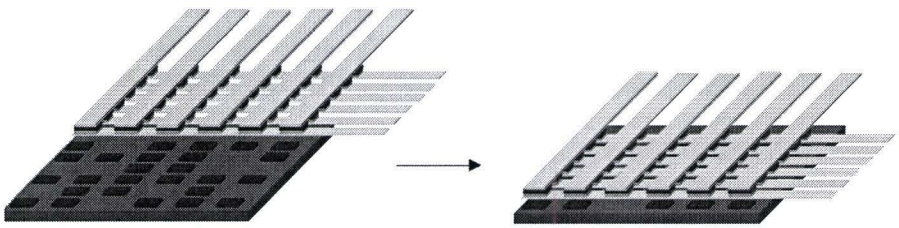

Figure 4.7: *Basic concept of MROM. On the left, the data carrier (bottom) and sensor array (top) are separated. On the right the data carrier and sensor array are aligned, and close together. The data can be read out by measuring the resistance of the MTJ sensors. Adapted from [58].*

2 dimensional array of bits. The read-out is performed by a reader. This reader consists of an array of magnetic tunnel junction (MTJ) elements. The data carrier and reader are placed close together, and aligned, so that each sensor can read one bit, as can be seen in Fig. 4.7. The magnetization of the bits on the data carrier determines the resistance of the MTJ sensor. By measuring the resistance of the MTJ sensor, the data is read out.

In this study, MFM measurements are performed on the data carrier, to see whether a magnetic field is present above the magnetic bits. This is not trivial for the data carrier used, since a continuous layer of magnetic material is deposited on the actual bit pattern (see also 4.2.1). The magnetic stray field of the bits is crucially important because it determines the resistance measured by the MTJ sensor. Finally, the effect of an external magnetic field is studied, for which the magnetization behavior of individual bits has been estimated. magnetization of the bits is also estimated, and influenced by applying an external magnetic field.

4.2.1 Sample properties

The data carrier consists of a glass substrate. Individual bits of 5×1 μm (length × width) are created in a 1 μm thick resist layer, on top of the glass substrate. A schematic representation of a bit can be seen in Fig. 4.8. With sputter deposition a CoFe ($Co_{90}Fe_{10}$) layer of 200 nm thick is deposited on the medium. As a result, a continuous CoFe layer is covering the bits as well as the substrate. During deposition a field is applied parallel along the long direction of the bits to create a field-induced uniaxial anisotropy.

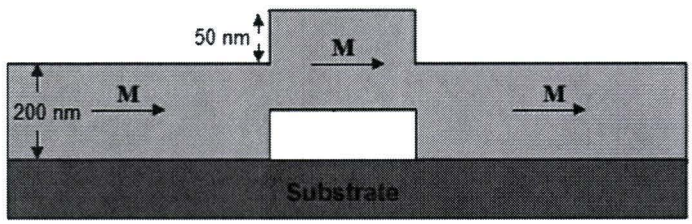

Figure 4.8: *Schematic representation of a bit. A ferromagnetic layer of approximately 200 nm is deposited onto a structured substrate. The height according to AFM measurements is approximately 50 nm. Dimensions are not drawn to scale.*

In Fig. 4.9, an AFM scan of 6 bits can be seen. The bits are patterned in a closely packed array with spacings between the bits of 2 μm in the long direction, and 3 μm in the short direction of the bits. The height according to the line profile in Fig. 4.9(b) is approximately 50 nm. A lot of artifacts are present in Fig. 4.9, which is mostly due to dust, by the exposure of the sample to air. This is of no influence to the MFM measurements because dust gives, in principle, no magnetic contrast. Why the dust concentrates around the bits is unknown at present. The dark area around the bits (and the dip in the line profile at 6.5 μm) indicate that the deposited layer is thinner around the bits; this is probably caused by a shadowing effect during deposition.

The magnetic moment of the entire medium is measured with a SQUID magnetometer. The measured magnetization as a function of the applied field is displayed in Fig. 4.10. The measurement is done with the magnetic field applied along the long direction of the bits. From the hysteresis loop follows a switch field, H_s, between 0 and 5 mT. The increasing magnetization at larger fields may be due to a misalignment of the applied magnetic field and the easy axis of the bits. If the magnetic field is at an angle with the easy axis, the magnetization of the bits will rotate away from the easy axis after switching.

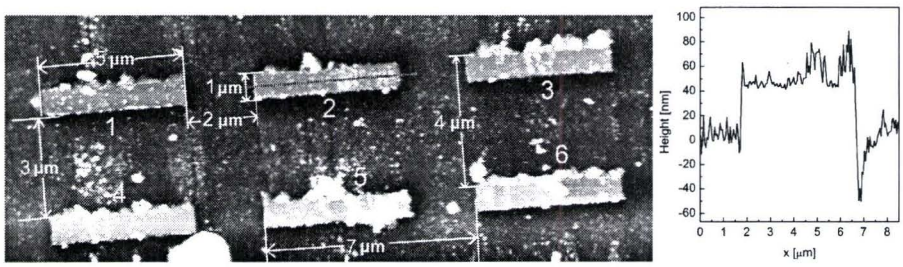

(a) (b)

Figure 4.9: *AFM image of a MROM sample. The image area is 22×8 µm. The sample consists of a structured resist layer on top of a glass substrate, with a CoFe layer deposited on top of it. (a) The image shows 6 bits with dimensions 5×1 µmn and a pitch of 7×4 µm. In the image the dimensions and spacings are also indicated. From the image it is clear that the sample is rather dirty; a lot of artifacts are present, like the large white spot at the bottom. (b) Line profile at the position indicated by the dashed line in bit 2. The height is approximately 50 nm.*

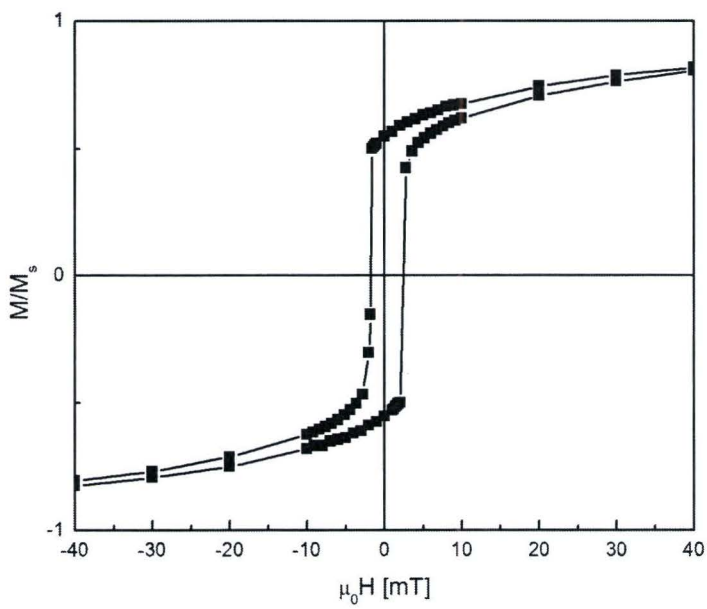

Figure 4.10: *Hysteresis loop of magnetization of the medium. The measurement is done with a SQUID magnetometer at room temperature. Only a relevant portion of the measured field range is shown. The field direction is parallel to the long axis of the bits.*

4.2.2 Results and discussion

First, an MFM scan at remanence (zero external field) is made of the bits, to investigate the magnetic signal emanating from the bits. An MFM image of 6 bits measured at remanence is shown in Fig. 4.11. No magnetic contrast can be seen on the bits in the image, which is in contrast with an expected strong black/white contrast between the two ends of the bit when it is uniformly magnetized. However, as indicated with the line profile, there is a small phase difference present. The markers indicate the maximum and minimum phase over two of the bits. The phase difference is 2.0±0.5 degrees. The distance between the markers of one bit is 5.2 μm, which corresponds quite well with the actual lateral dimensions of the bit. From Fig. 4.11 a complicated domain structure in the continuous film between the bits can also be seen. It can be concluded that a small magnetic stray field is present above the bits. However, the continuous film also shows magnetic contrast, with a phase shift in the same order of magnitude as the signal of the bits.

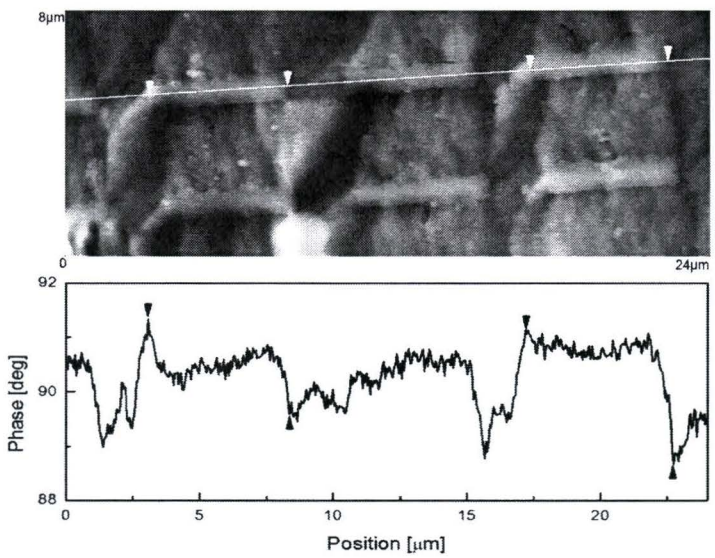

Figure 4.11: *(a) MFM image of 6 bits measured at remanence, the scan size is 24×8 μm. The white line indicates the place of the line profile in (b). The markers indicate the maximum and minimum phase signal of 2 bits. The horizontal distance between the markers is 5.2 μm.*

From this measurement it cannot be concluded that the magnetic field of the bits can be straightforwardly measured in an MROM device. To further investigate this, a large area is scanned, which results in the MFM image

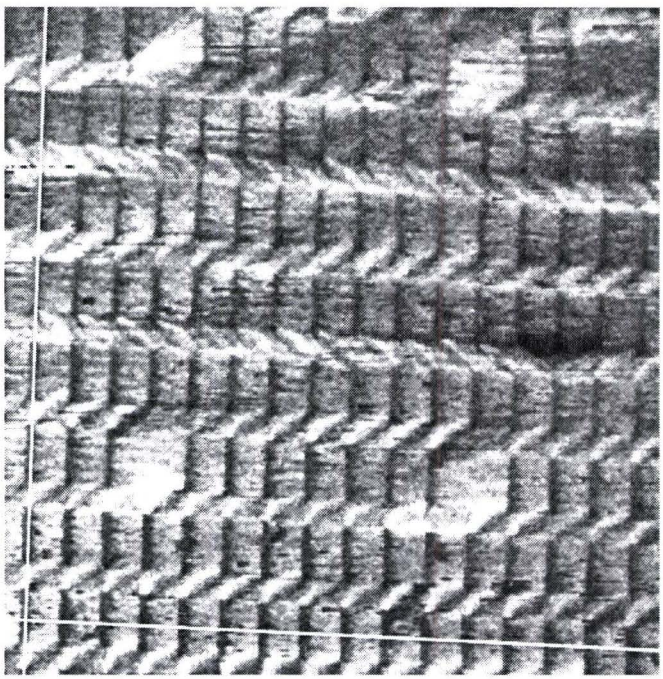

Figure 4.12: *MFM scan of a 65×58 μm bit area at zero magnetic field. The dark areas are the bits. The 4 white spots indicate missing bits.*

shown in Fig. 4.12. It shows a 65×58 μm MFM image of the bit pattern. The bits are visible as the dark contrast areas, as opposed to white contrast of the bits in Fig. 4.11. This is probably related to the magnetization direction of the tip. From Fig. 4.12 it becomes clear that 4 bits are missing. These bits are omitted intentionally from the substrate, to test the resolution of the MTJ sensor array [58]. Generally, it is seen (as in Fig. 4.11) that the magnetic contrast is not located within the bits, but rather in the surrounding area. To additionally quantify the magnetic contrast seen in this image two line profiles are made. The vertical profile in Fig. 4.13(a) is measured from the bottom to the top of the vertical line in Fig. 4.12. The width of the hills is approximately 2 μm wide, and the valleys are approximately 5 μm wide. A pitch between the hills of approximately 7 μm is measured. The horizontal line profile in Fig. 4.13(b) shows a pitch between the valleys of approximately 4 μm, consisting of a valley width of 1 μm, and a hill width of 3 μm. All dimensions mentioned here correspond to the dimensions of the bits as can be seen in Fig. 4.9.

In Fig. 4.14 a cross-section of the magnetic field measured (in the long direction of the bits) with MTJ elements from [58] is shown for comparison. Note that the magnetic field is negative, this relates to the calibration of the MTJ resistance. Measurements are performed at 2 μm intervals with

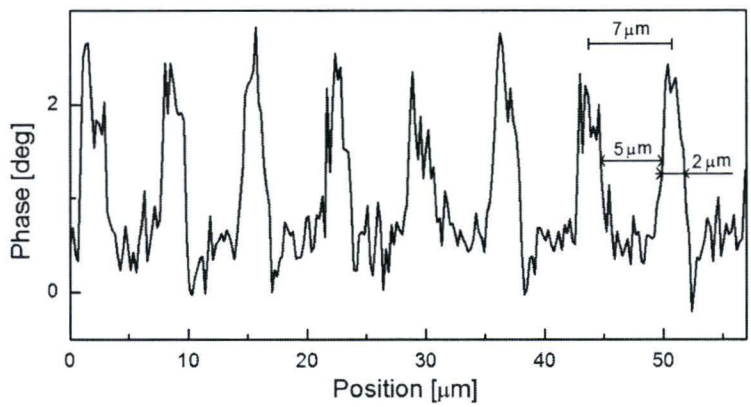

(a) Vertical line profile.

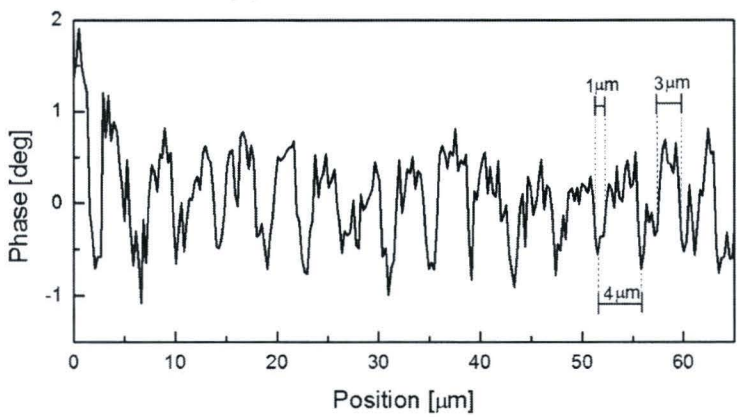

(b) Horizontal line profile.

Figure 4.13: *Line profiles at the white lines indicated in Fig. 4.12. (a) The direction of the vertical profile is from the bottom to the top of Fig. 4.12. The hills have a pitch of approximately 7 µm, and are approximately 2 µm wide. The valleys are approximately 5 µm wide. (b) The horizontal profile is taken from left to right. The valleys have a pitch of approximately 4 µ.*

a sensor moving in vertical direction. The magnetic field oscillates with a period of 7 μm, and although hardly visible, it can be seen that the valleys are slightly wider than the hills. This is the same result as found by the line profile of the MFM measurement in Fig. 4.12. The limited resolution in the data obtained with the MTJ sensor is due to the horizontal width (5 μm) of the sensor. Therefore the measured signal is integrated over a 5 μm wide area. To more directly compare this to a line scan measured with MFM, an average line profile in the vertical direction (integrated over the width of the entire image) is shown in Fig. 4.15. The area of maximum phase signal in the average line profile are separated by approximately 7 μm, which corresponds to the oscillation period of the magnetic field in Fig. 4.14. So

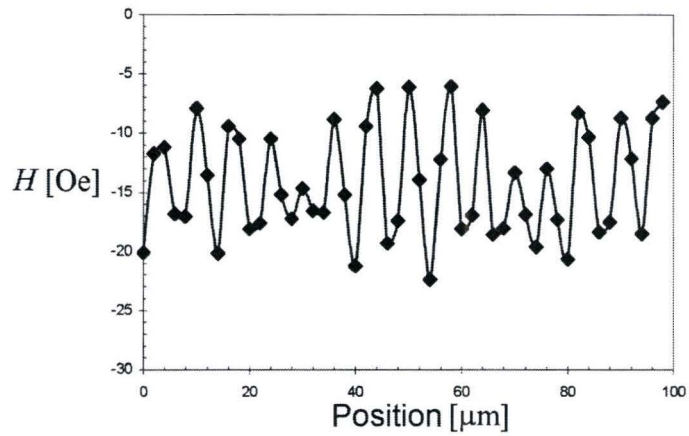

Figure 4.14: *Cross section of the magnetic field measured with an array of MTJ sensors. The oscillation of the magnetic field has a period of 7 μm. Adapted from [58].*

probably the MTJ array does not measure the individual bit magnetization, but an averaged oscillating signal, which is determined mostly by the pitch of the bits.

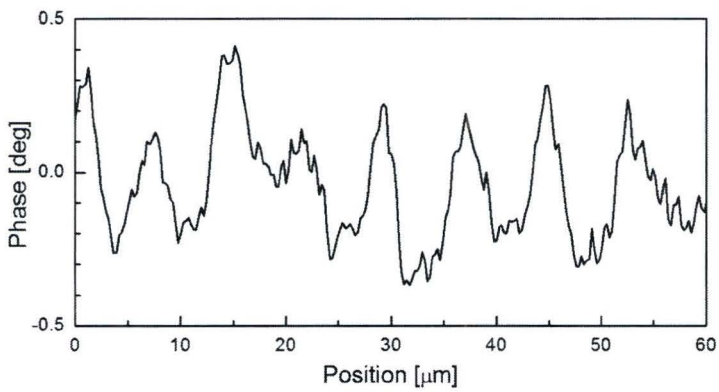

Figure 4.15: *Average line profile in the vertical direction of Fig. 4.12, integrated over the width of the entire image.*

Next, a magnetic field of +20 mT is applied approximately parallel to the long direction of the bits. Fig. 4.16 shows an MFM scan of 6 bits, and the line profile across 3 bits. It is clear that there is a large black/white contrast between the left and right side of two bits. The phase shift at the ends of the bits is 5.6±0.5 degrees (averaged over all 6 bits). The phase difference is measured at the markers as indicated for two bits in Fig. 4.16. Also the domain structure of the film changed. It seems that the complex structure

observed in Fig. 4.11 has changed to a rather uniform image without magnetic contrast, reflecting a continuous magnetization in the region between the CoFe bits. This becomes especially clear from the top of the image in Fig. 4.16, far away from the bits. Fig. 4.17 shows the magnetization of the bits with an applied magnetic field of -20 mT parallel to the long direction of the bits. The magnetization of the bits is opposite in direction to the situation at $+20$ mT.

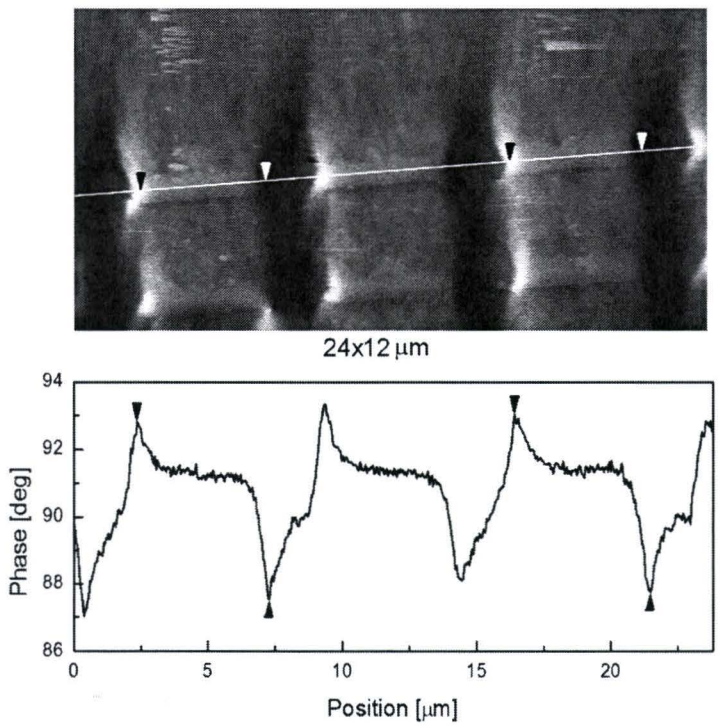

Figure 4.16: *(a) MFM image of 6 bits measured at an applied field of 20 mT. From the line profile follows a maximum phase difference of 5 degrees at a distance between the markers of 5 µm.*

In Fig. 4.18, the field was applied perpendicular to the long direction of the bits. The magnetization of the bits is now perpendicular to the long axis, even in the situation at zero applied field, although the sharp black/white contrast is now partially lost. The remanence at zero field is not to be expected, because from the shape of the bits the magnetization is likely to be parallel to the long axis. It could be that this is due to the influence of the continuous film, where a domain structure forms, as can be seen at an applied field of 0 mT.

Next, a further quantification of the information contained in these MFM im-

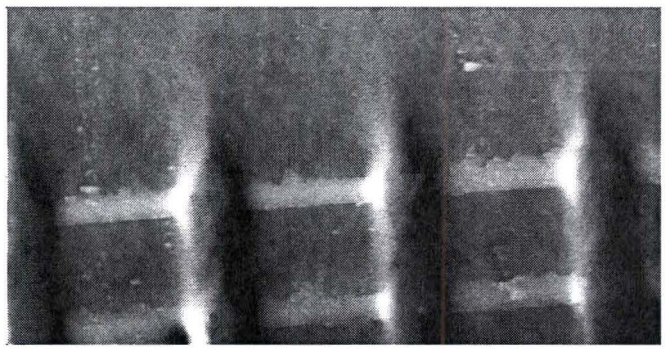

Figure 4.17: *MFM Measurements at an applied magnetic field of* -20 *mT, applied approximately parallel to the long direction of the bits.*

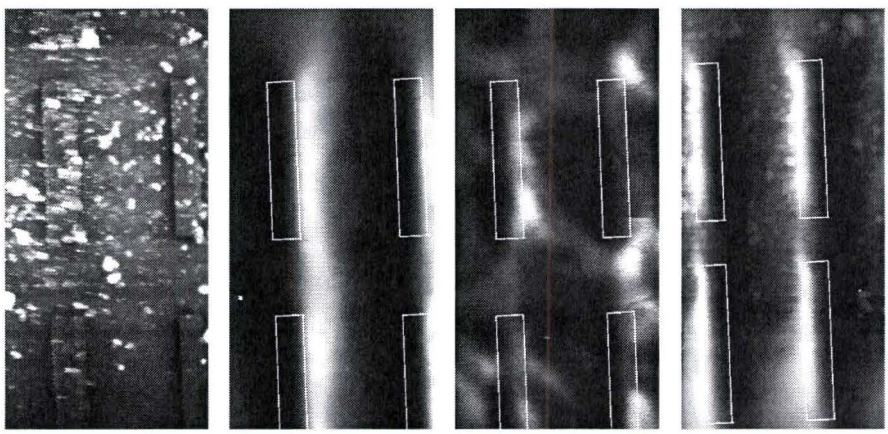

Figure 4.18: *MFM Measurements, the field is applied perpendicular to the long direction of the bits. The magnitude of the field is indicated. The images are* 8×16 μm. *More results are presented in Appendix B.*

ages is obtained. According to eq. 2.30, the observed phase shifts are proportional to the second derivative of the sample stray field ($\Delta\phi \propto \partial^2 H_z/\partial z^2$), where the tip is assumed to be magnetized in the z-direction (perpendicular to the sample surface). The stray field $\boldsymbol{H}$ can be expressed as the gradient of a scalar potential, $\boldsymbol{H} = -\nabla\phi_m$ (eq. 2.23), where the magnetic scalar potential is given by eq 2.24. Far from the bit the potential reduces to

$$\phi_m \approx \frac{\boldsymbol{m}\cdot\boldsymbol{r}}{4\pi r^3}, \tag{4.9}$$

where $\boldsymbol{m} = \int \boldsymbol{M} dr^3$ is the total magnetic moment of the bits. Therefore, the phase shift is proportional to the magnetization, i.e. $\Delta\phi \propto \boldsymbol{M}$.

To determine a measure for the magnetization, a line profile at the center of the bits is made. The maximum of the phase signal at one end of the bit and the minimum value at the other are subtracted, which gives a qualitative estimate for the magnetization. The distance between the measurement points (max-min) is 5 μm, this is the length of the bits. In Fig. 4.19 the magnetization of 6 individual bits is determined according to this method. The measurements are made at an applied field from +20 to −20 mT. Each symbol represents one particular bit numbered in Fig. 4.9, and the solid line represents a fit to the average value of the phase difference. The found phase difference is scaled to 1 by dividing all the measurements by the largest found phase difference of 6.8 degrees. This is the phase difference of bit 4 at −20 mT. No measurements are performed in the field range between 0

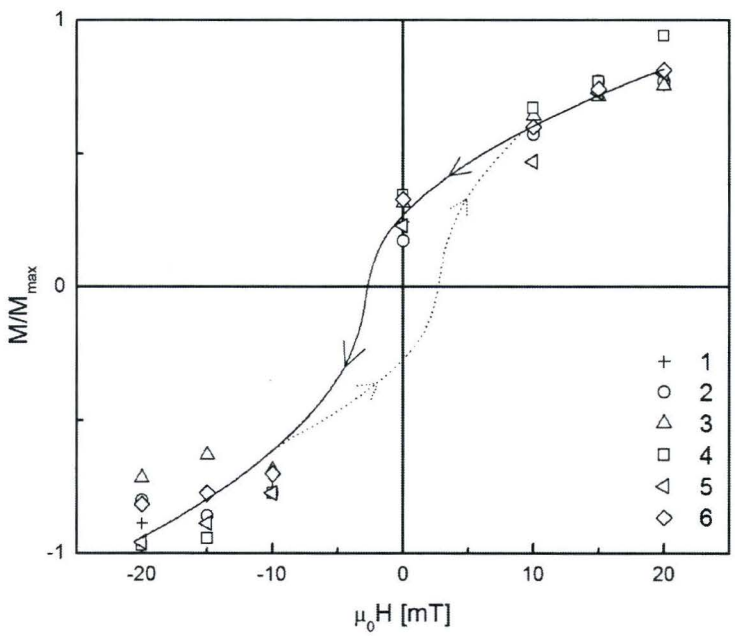

Figure 4.19: *The determined magnetization of a MROM bit as a function of the applied field. The applied field was parallel to the long axis of the bit. (1)-(6) are the measurements for individual bits. The solid line is a guide to the eye only for decreasing field, the dotted line for increasing fields.*

and −10 mT, so the actual switch field is between 0 and −10 mT. This is in the same range as the switch field found with the SQUID magnetometer. However, it should be realized that with SQUID the full magnetic layer is measured, whereas here the magnetic behavior of an individual bit is probed. From Fig. 4.19 it is clear that at $\mu_0 H = 20$ mT, the magnetization is not yet saturated. In the field range from 10 to 20 mT an increase in magnetization is observed, which is in agreement with the fact that the magnetization is not saturated at $\mu_0 H = 20$ mT (Fig. 4.10).

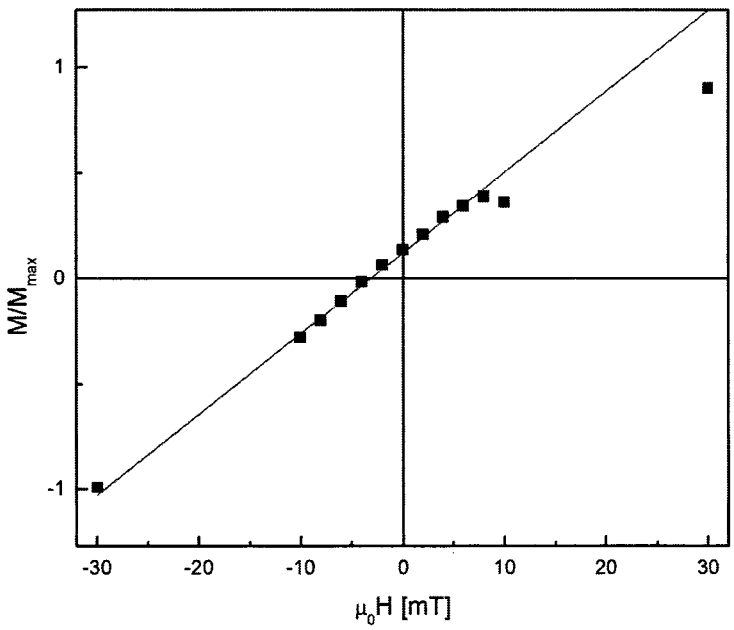

Figure 4.20: *The magnetization of a bit as a function of the applied field. The applied field was perpendicular to the long axis.*

Figure 4.20 shows the magnetization of one bit determined by MFM, where the applied field is perpendicular to the long axis as in Fig. 4.18. This indeed resembles a hard-axis loop, where the magnetization linearly increases with increasing field. A small remanence is visible in Fig. 4.20, which is not expected for this configuration. This remanence can also be seen in the MFM images in Fig. 4.18 and appendix B. The reason for a somewhat lower magnetic moment at +10 mT and +30 mT is not clear from the measurements, and would require more data points taken at higher fields.

4.2.3 Conclusions

It is shown that the stray field of individual bits can be qualitatively measured with MFM. At remanence only a small signal is observed, corresponding to a non-zero magnetic field experienced by the tip. The line profile of a large scan indicates contrast with a period of 7 μm. This is similar to the actual magnetic field that is detected with an MTJ in an MROM [58, 59].

At a non-zero applied magnetic field, the measured phase shift (which is proportional to the magnetization) significantly increases. In this way, the magnetization can be determined qualitatively with MFM by measuring the

maximum phase difference of individual elements. The magnetization of the bits for the applied field parallel to the long axis resembles the magnetization of an easy axis loop, as measured by SQUID for the full magnetic medium. However, MFM data at intermediate fields are required to further test the hysteresis of individual bits. The situation with the applied magnetic field perpendicular to the long axis has a hard-axis behavior with a small remanence.

4.3 MRAM

MRAM (magnetic random access memory) technology, based on the use of magnetic tunnel junctions (MTJs) as memory elements, is a potentially fast nonvolatile memory technology. In recent years the MRAM technology is based on arrays of patterned magnetic bits where each bit contains a magnetic tunnel junction (MTJ) [6, 60]. In Fig 4.21 a typical MRAM bit can be seen. It consists of a MTJ sandwiched between a word and a bit line. The MTJ consists of two ferromagnetic (FM) layers separated by a thin insulating tunnel barrier. The lower layer is "pinned", implying that its magnetic orientation cannot be changed during normal operation, whereas the magnetic orientation of the upper "free" layer can be changed by the application of a sufficiently large magnetic field. The magnetic state of the free layer is defined as parallel or anti parallel with respect to the magnetically pinned layer. Challenges for MRAM development include the reduction of magnetic switching fields, eliminating bit instabilities and scaling down the lateral dimensions.

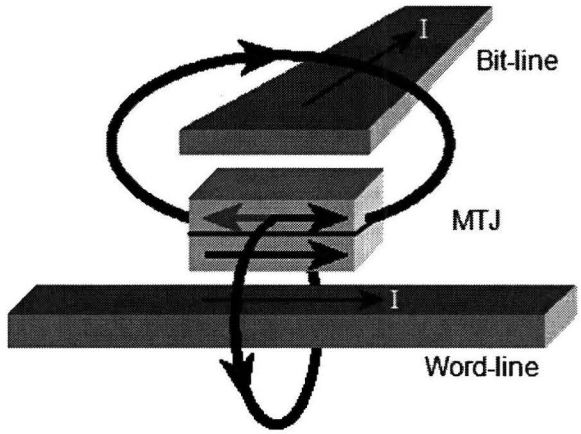

Figure 4.21: *In magnetic random access memory (MRAM) technology an MTJ is used to store data. Data can be written to the MTJ by sending an electric current through the word and bit line. The magnetic field produced by the two currents (indicated by the black circles) triggers the magnetic moment of the free layer to move to a particular orientation. The stored data can then be read electronically by measuring the resistance of the cell.*

In this section, the magnetic behavior of structured MTJ stacks as observed by MFM, is described. Also, the change of magnetization with the application of external magnetic fields is demonstrated.

4.3.1 Sample properties

Square MRAM bits (without electrical contacts) are fabricated. This is done by sputter deposition of the layers onto a substrate. The multilayer consists of a Si substrate with the following layers grown on top: 5 nm Ta/ 5 nm CoFe/ 10 nm FeMn/ 3.5 nm CoFe (pinned layer)/ 0.9 nm AlOx/ 15 nm CoFe (free layer)/ 5 nm Ta. These are then covered with a resist layer, and successively patterned by electron beam lithography. The sample is then etched, by which structures with sizes of 1×1 μm are formed. The resulting MRAM structure is schematically shown in Fig. 4.22.

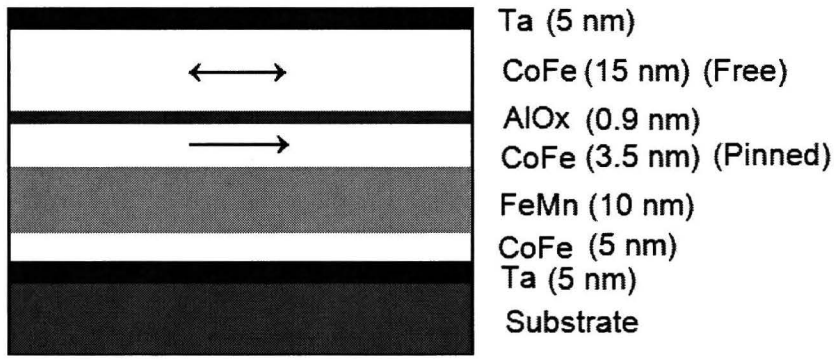

Figure 4.22: *Schematic representation of a MRAM bit. The different layers are indicated in the picture. The arrows indicate the free and pinned magnetic layer.*

In Fig. 4.23(a) a scanning electron microscope (SEM[2]) image of several bits can be seen. The bits are 1 μm square, and have a pitch of 2 μm. The height of the bits is approximately 41 ± 5 nm, as can be seen by the line profile of the AFM image in Fig. 4.23(b). This height is consistent with the nominal height of 44 nm of the total stack. In the AFM image, some distortions can be seen as bright white spots, in particular at the edges of some elements. This is probably due to the processing of the sample, some residual resist is left at the edges of the bits.

4.3.2 Results and discussion

In Fig. 4.24(b–d) MFM measurements of 10×10 μm can be seen. The topography is shown in Fig. 4.24(a) for clarity. The white spots probably originates from dust on the sample, or redeposited material as a result from the etching process. In the absence of a magnetic field an MFM image

[2]Philips XL 30 SEM, located at TU/e.

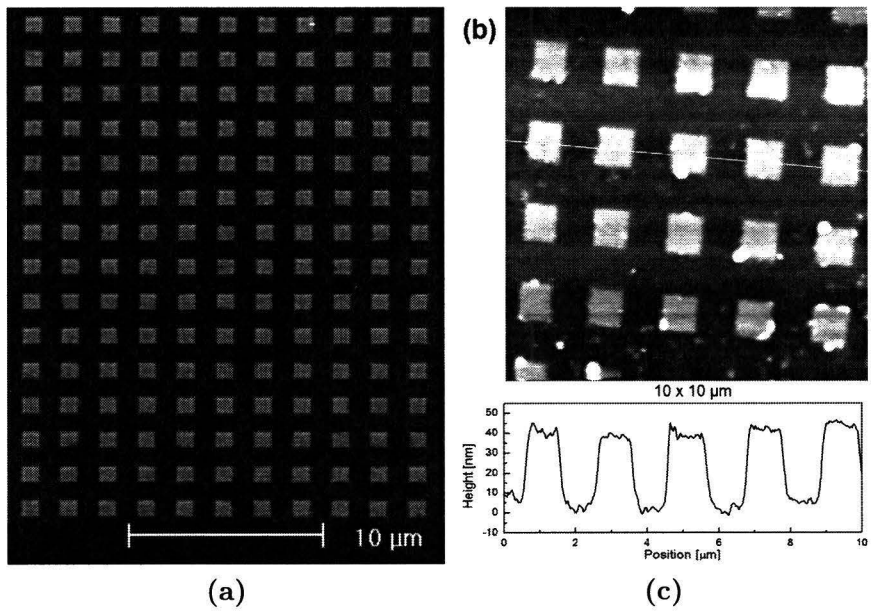

Figure 4.23: *(a) Scanning electron image of a sample with MRAM bits measured at TU/e. The bits are 1×1 µm, and have a pitch of 2 µm. (b) AFM image of the same sample. According to the line profile in (c) the height of the bits is approximately 41 nm.*

(b) clearly shows the non-uniform magnetization distribution in the MRAM bits by the complex contrast. Also the magnetization reversal induced by scanning with a magnetic tip, indicated by the horizontal lines on the bits can be seen. This will be addressed later. All bits are switched to a rather uniform magnetic state by application of a magnetic field (c) in the horizontal direction. This indicates that the free layer of the bits is rotated, and the direction of the magnetization of all the bits is parallel to the applied field. Subsequently, application of a negative magnetic field (d) shows again that the bits have changed their magnetization direction. However, in this case the bit indicated by the circle is not switched at -30 mT. Probably pinning of the magnetization at imperfections requires a larger applied field for this bit to switch. The bit indicated with the square switches under the influence of the stray field of the tip during scanning. Contrast in Fig. 4.24(c) and Fig. 4.24(d) is different due to the scanning errors in the top of Fig. 4.24(c) which suppresses the magnetic contrast. Comparing the line profiles in Fig. 4.24(e) and (f) shows approximately the same phase shift for both measurements.

In Fig. 4.25 the magnetization of the entire sample is measured as a function of the applied field with a SQUID magnetometer at room temperature. Two

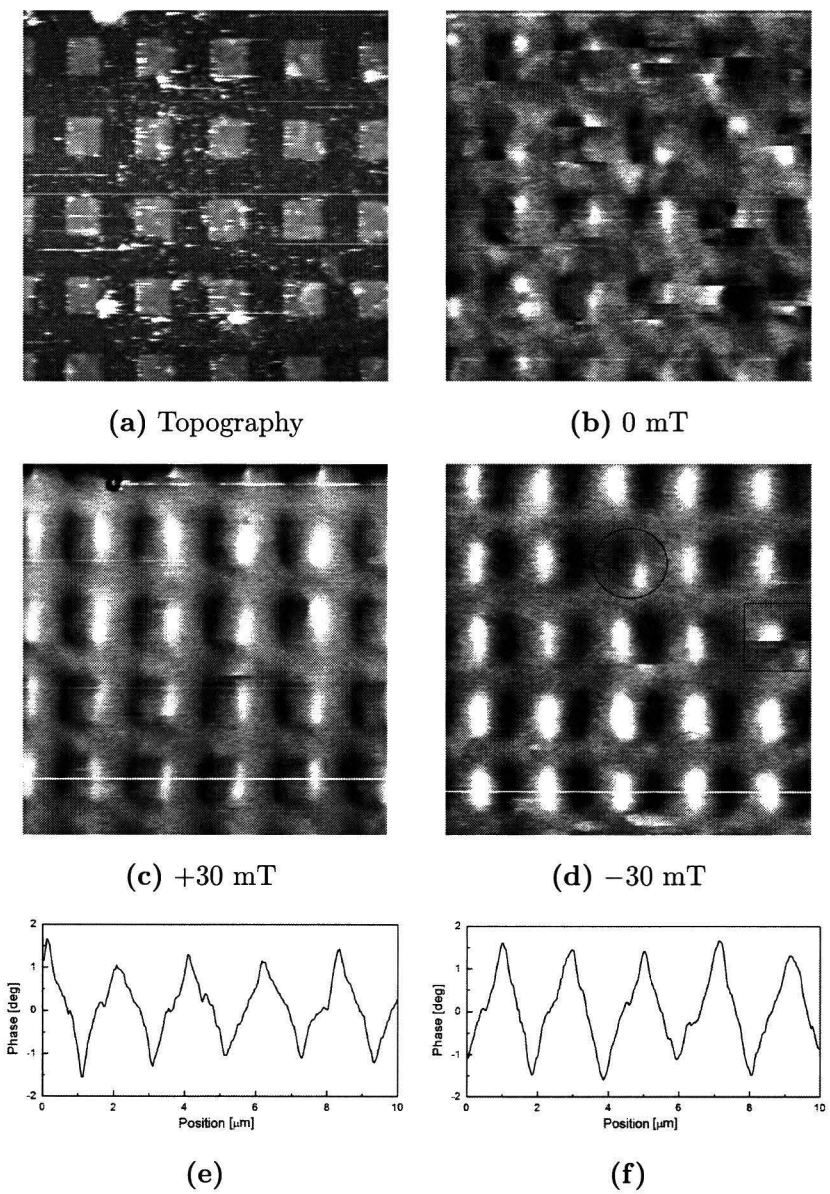

Figure 4.24: *A 10×10 µm scan of MRAM bits. (a) Topography. MFM scans at (b) 0 mT, (c) +30 mT and (d)-30 mT. The circle indicates a bit that is not changed after applying a negative field. The square indicates a tip-induced switching of a bit. In (e) and (f) line profiles of the line indicated in (c) and (d) can be seen.*

switches can be seen, at an applied field range of approximately 0–30 mT, and at a field range of approximately 100–150 mT. Comparison with the MFM measurement above indicates that the switch of the free magnetic layer is indeed observed with MFM. However, at zero applied field the MFM measurements show a complex structure with random orientation of the magnetization, which cannot be correlated easily with SQUID for a large collection of bits measured simultaneously.

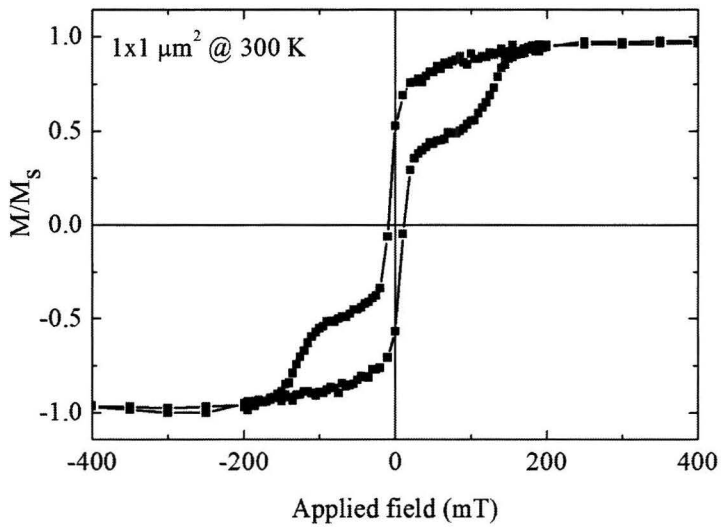

Figure 4.25: *SQUID measurement at 300 K of the magnetization as a function of the applied field.*

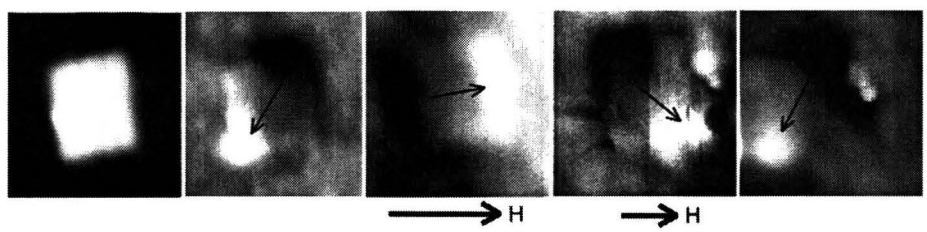

(a) AFM **(b)** 0 mT **(c)** 100 mT **(d)** 30 mT **(e)** 0 mT

Figure 4.26: *(a) AFM image of an MRAM bit, the image is 1.7×1.7 μm. MFM image of the same MRAM bit can be seen at an applied field of (b) 0 mT, (c) 100 mT, (d) 30 mT, and (e) 0 mT. The direction of the applied field is indicated below the images. The arrows in the bit indicate the magnetization direction.*

In Fig. 4.26 an individual MRAM bit is shown. In (a), the AFM image of the 1×1 μm bit can be seen, and (b) through (e) show MFM images of the same bit at applied fields of 0, 100, 30, 0 mT, respectively. The measurements are performed in this order. The arrow in the bit indicate the magnetization direction as suggested by the contrast in the image. In figure (b) and (e) the

magnetization at remanence can be seen, where we like to add that the history of applied magnetic fields in (b) is not known. By applying a magnetic field of 100 mT (c), the magnetization of the bit changes its direction, as indicated by the changed black-white direction of the contrast. Measuring the magnetization after application of the external magnetic field, as seen in (e), gives approximately the same magnetization direction as in (b). According to the SQUID measurement, the magnetization direction was expected to remain approximately in the same direction as in Fig. 4.26(c). The change in direction can be due to the presence of redeposited magnetic material on the structure leading to a preferred direction of the magnetization. Fig. 4.27 shows (a) a zoom of the topography, and (b) a 3D representation of the bit seen in Fig. 4.26(a). The front left corner is clearly higher than the rest of the bit, which could indicate the presence of redeposited magnetic material at that corner, and a subsequent preferential direction of the magnetization. However, it cannot be excluded that the contrast in the AFM image is partially obscured by magnetic tip-sample interactions (see, for example, also Fig. 2.13). An alternative explanation is related to possible fluctuations in the Al_2O_3 barrier thickness. When, at the location of the bit, the Al_2O_3 is very thin, this could lead to direct coupling to the underlying magnetic layer that is exchange biased to FeMn. Due to this, the magnetization could be pinned in a specific direction.

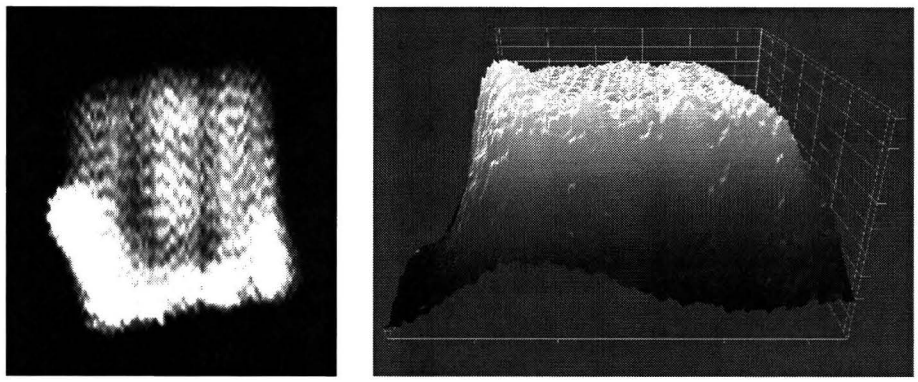

(a) (b)

Figure 4.27: *Zoom of the topography of the bit in Fig. 4.26. The front (bottom) left corner is clearly higher than the rest of the bit. (a) The contrast is focused on the top of the bit, all the surrounding area appears black. (b) 3D image of the same area.*

At an intermediate field of 30 mT (Fig. 4.26(d)) the magnetization is changed *during* the measurement. As the MFM tip was scanned over the bit, the

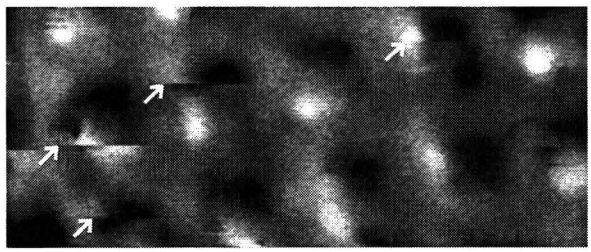

Figure 4.28: *MFM scan of 10×4 μm, measured at an applied field of 0 mT. Several bits switch their magnetization under the influence of the stray field of the tip, indicated with the white arrows.*

magnetization suddenly changed. This can be seen by the vertical line in the center of the bit in. As mentioned, the magnetic state of a bit at remanence is influenced by the stray field of the MFM tip. In Fig. 4.28 an MFM scan of several bits can be seen, measured at 0 mT. The white arrows indicate switching of the magnetization of the bits under the influence of the stray field of the MFM tip. Fig. 4.29 shows a zoom of a bit, in (a) the magnetization switches indicated by the horizontal line. Scanning the same bit again (b) results in the same magnetic state as in (a) after the switch. Apparently, the magnetic state of the bit after switching is more stable than the state before the switch. In follow-up experiments, this can be prevented by using tips with a smaller magnetic stray field, although in that case, application of an external field may influence the state of the tip.

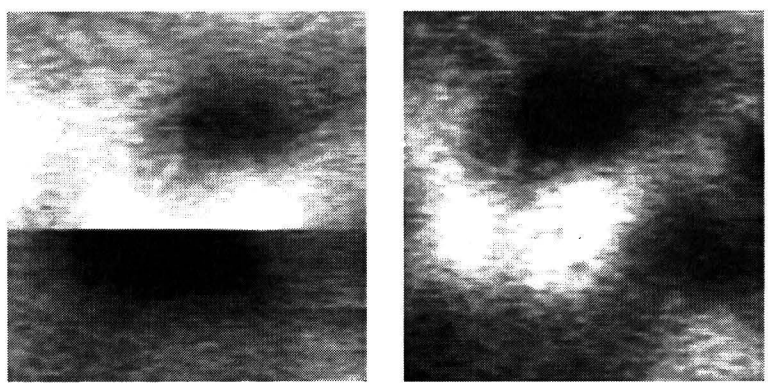

(a) (b)

Figure 4.29: *Zoom of a bit. (a) The bit switches magnetization direction due to the influence of the tip. (b) Subsequent scan shows the tip in the same state as after the switch. Note that the resolution of the images is poor due to the fact that they are zoomed from a larger scan. Image size is 2.5×2.5 μm.*

4.3.3 Conclusions

The magnetic microstructure of fabricated MRAM bits is analyzed by MFM. The magnetic state of the individual bits can be visualized with MFM, and influenced by application of an external magnetic field. It is seen that individual bits do not always behave like expected by macroscopic measurements. For example, this can be caused by the influence of redeposited magnetic material, during the etching process, or coupling with the underlying pinned layer. At low field, the magnetic stray field of the tip is large enough to change the magnetization and a non-uniform distribution of the magnetic domains is observed. In contrast, MRAM bits reveal an almost uniform magnetization at applied fields of 30 mT.

4.4 Structures for spin injection in semiconductors

Traditional semiconductor devices operate by using electron charge to carry information. Recently, semiconductor devices based on the control and manipulation of electron spin were proposed [61, 62, 63]. For such devices it is necessary to inject a non-equilibrium spin population into the semiconductor. Spin injection can be achieved from a ferromagnetic metal (FM) into the semiconductor (SC) by using a tunnel barrier (TB) [64].

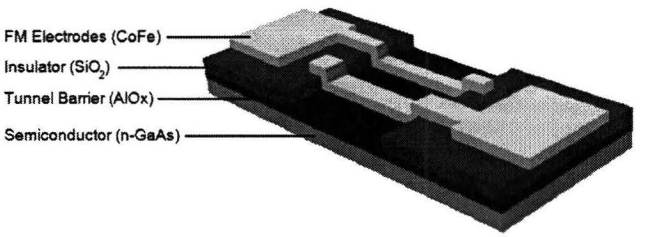

Figure 4.30: *A schematic representation of a semiconductor based spin valve. Two CoFe electrodes are placed on a n-GaAs semiconductor, separated by an Al_2O_3 tunnel barrier. Adapted from [65].*

The lateral FM/TB/SC/TB/FM structure, as seen in Fig. 4.30, acts as a spin-valve, since the two ferromagnetic layers can be oriented in a parallel orientation, as well as in an anti-parallel orientation (see also section 1.2). Application of a bias voltage over the FM electrodes leads to a spin-dependent current. By designing the FM electrodes to have different switching fields, their magnetization directions can have either a parallel or anti-parallel alignment configuration, depending on the external magnetic field. The switch field can be controlled via shape anisotropy as seen, e.g. in eq. 4.5 for the SW-model. Electrodes of different width will therefore switch their magnetization direction at different applied fields. To investigate the magnetization reversal of the electrodes, the switch field of CoFe strips as a function of the width is determined in a traineeship project [66]. In this section, the most important results of that study will be discussed. First, some properties of the sample are discussed, and the measurements are explained. Then, the switch field of the CoFe strips is determined using MFM, and investigated as a function of the width of the strips. A comparison is made with theoretical models and the results of micromagnetic simulations are also included.

4.4.1 Sample properties

The width dependence of the switch field H_s is tested with structured CoFe strips. Strips of approximately 20 μm long are patterned by e-beam lithography in a resist layer on a GaAs substrate. Next, CoFe ($Co_{90}Fe_{10}$) is deposited, and the resist is removed. The resulting strips are capped with a thin layer of Ta to prevent oxidation. The width of the strips is varied between 0.5 and 1.5 μm, and the thickness of different strips varies between 50-100 nm, depending on the width of the strip. The variation in thickness is a result of the sample preparation. In Fig. 4.31 an AFM image of a strip with a width of approximately 1 μm can be seen. The edges of the strip are rough as a result of the fabrication process.

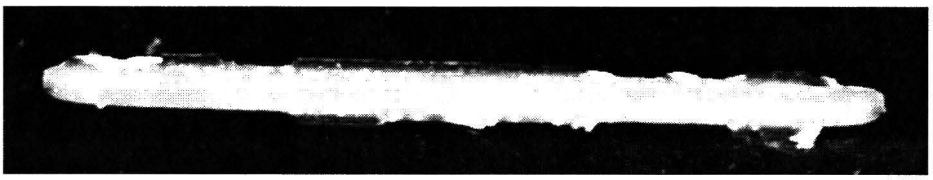

Figure 4.31: *AFM image of a CoFe strip with length 20 μm, and width 1 μm. The edges of the strip are rough due to the sample preparation. The image is 22×4 μm.*

4.4.2 Measurement principle

In Fig. 4.32 a magnetization curve is shown to explain the measurement principle. At a large applied field, the strip will be saturated as in (A). The corresponding MFM image (A) indicates the magnetic state of the strip, which, in this case, is single domain as seen by the large black and white contrast between the strip ends. This situation will be maintained until a field $|H| > H_s$ in the direction opposite to $\boldsymbol{M}$ is applied, and the magnetization switches to situation (B). In this case, again a sharp contrast is observed, although now in opposite direction. The switch field, H_s, is found in an iterative way:

- A large positive field is applied (1), and an MFM scan (all measurements are done in remanence) reveals that the strip is in situation (A). After each step this large positive field is applied again.
- Application of a negative field and subsequent measurement at zero field, will show that the strip is switched (2) in situation (B), or remains unswitched (3) and is still in situation (A).

- If the strip was switched, approximately half of the field (2) is applied (3), and situation (A) is found back. If the strip was unswitched, a larger field (2) is applied until situation (B) is found.
- A field between (2) and (3) is applied, and again a MFM scan is performed to check the state of the strip.
- This process continues, with decreasing step sizes, until the switch field (4) is found.

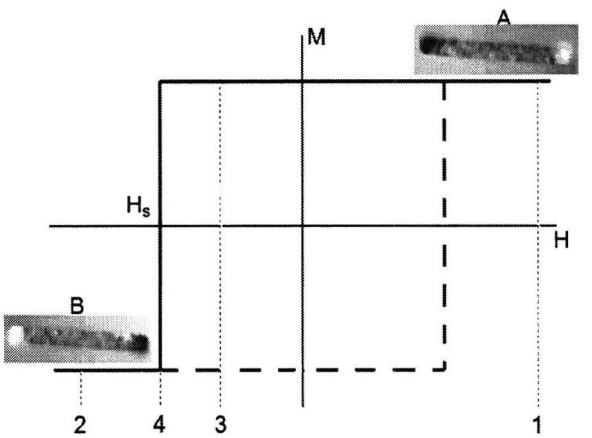

Figure 4.32: *Visualization of the measurement principle on the basis of a standard hysteresis loop. The switch field H_s is found in an iterative way (1)-(4); further explanation of the measurement principle is given in the text.*

To show magnetization switching of the CoFe strips with MFM, Fig. 4.33 shows typical MFM images of the end of a CoFe strip. The images are zoomed in at the end of a strip to focus on the magnetization switching. The strip has a width of 1.5 μm. The measurements are not performed in the order shown in the image, but according to the iterative way above (see the number in the upper right corner of each image). Note that not all images have the same size. As long as the contrast at the end is dark, the strip is not switched, bright contrast means that the strip is switched. From Fig. 4.33 it is clear that the magnetization of the strip switches between -11.1 and -11.2 mT.

MFM images, such as those in Fig. 4.33, show that magnetic contrast is concentrated at the ends of the strips, with white contrast at one end and dark at the other. The polarity of the magnetization depends on whether the previously applied field is larger than the switch field ($|H| > H_s$). Although this suggest a single domain state as mentioned before. A special case can be seen in Fig. 4.34. The two entire strips show a detailed internal structure probably related to a non-uniform magnetization. Additionally,

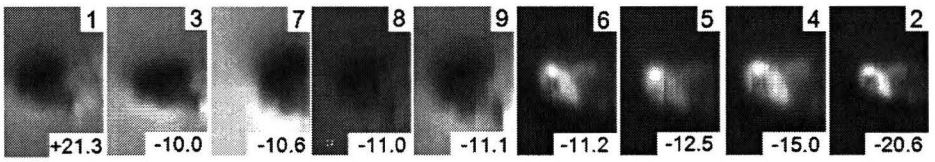

Figure 4.33: *MFM images of a 1.5 μm wide CoFe strip, showing switching of the magnetization between -11.1 and -11.2 mT. The images are zoomed around the end of the strip, but are not all of the same size. The measurement order is indicated in the top right corner of each image.*

the bottom strip clearly shows a domain wall. This may indicate a more complex domain structure, which in turn may greatly affect the mechanics for magnetic switching, including the actual switching field.

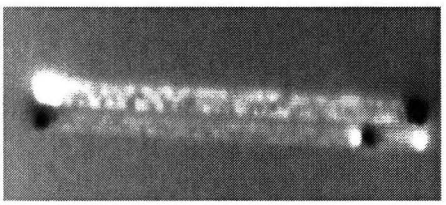

Figure 4.34: *MFM scan of two strips. The scan size is 23×10 μm. The top strip has a width of 1.5 μm, and the bottom strip is 1.0 μm wide. The magnetization of both strips is opposite, although the field history is not known. It is clear that the ends of the strips show magnetic contrast, but also an internal structure is visible. The bottom strip clearly shows a domain wall.*

4.4.3 Results and discussion

As indicated above, strips of different width switch at different applied magnetic fields. By measuring strips of different widths, the magnetic switch field H_s is found as a function of the width of the strips. Fig. 4.35 shows H_s versus the width, for an external field along the long axis of the strips. These measurements are performed according to the described method in section 4.4.2. Two series of measurements are shown. The open squares are performed on as-deposited samples, the full squares are measured after cleaning of the sample. The sample is cleaned because of dust contamination with acetone and ethanol in an ultrasonic bath. The magnitude of H_s after additional cleaning is significally higher than before, although the amount of data for the uncleaned sample is too limited too draw definite conclusions. The enhanced H_s is probably due to the formation of oxides during the cleaning process, which reduced the amount of CoFe in the strips, and therefore suppresses the effective width. In order to determine the mecha-

nisms of magnetization switching in CoFe strips, the different magnetization switching models, as discussed in section 4.1, are now applied.

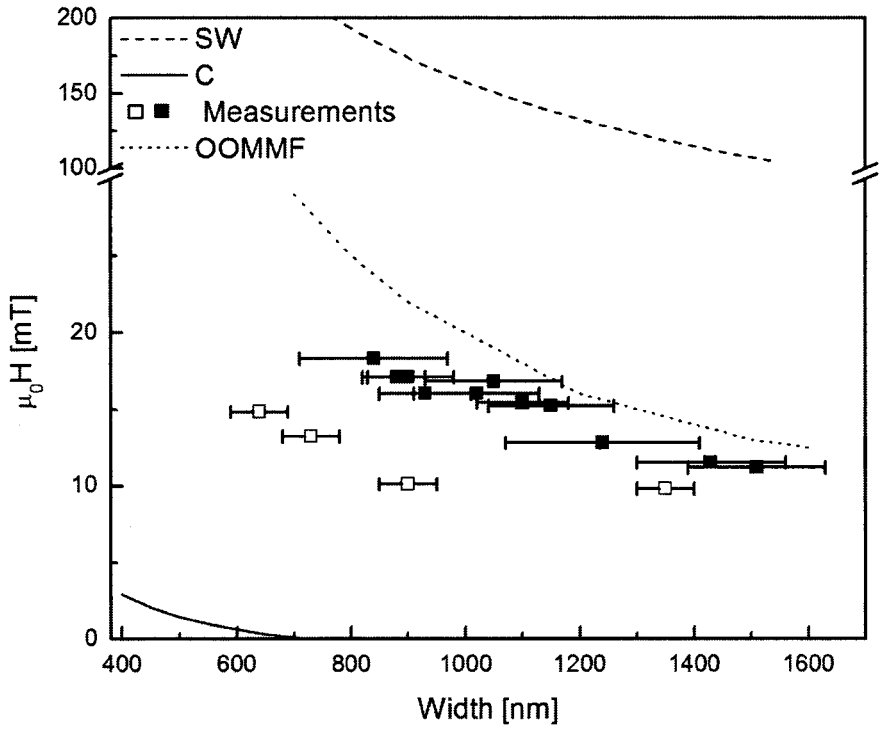

Figure 4.35: *The switch field of the CoFe strips as a function of* D*, the width of the strip. The open squares are from the measurement of the sample before cleaning and the solid squares are obtained after cleaning. Above the vertical break, the SW curve is presented for comparison. The solid line represents the curling model, and the dotted line represents the switch field according to micromagnetic simulations performed with OOMMF. For more details see the text.*

The Stoner-Wohlfarth (SW) model (see section 4.1.1) is applied first. Different switch fields of strips with different widths caused by their different shape anisotropies can be calculated by approximating the strips with ellipsoids with known demagnetizing factors, $N_\perp$ and $N_\parallel$ (see Appendix A). The demagnetization factors are approximated by those of a slender ellipsoid, because the length of the strips is larger than the width, which is again larger than the height. The crystalline anisotropy constant K is assumed to be negligible, because of the polycrystalline structure of the deposited CoFe layer. Easy axes are pointing in random directions, which means that there should be effectively no magnetocrystalline anisotropy in the plane of the strips.

Substituting the calculated demagnetization coefficients into eq. 4.5 gives

the switch field according to the SW model:

$$H_s = (N_\perp - N_\parallel)M_s, \tag{4.10}$$

as indicated with the dashed line in Fig. 4.35. Calculated switch fields for strips with different widths were between 10 mT for 1.5 μm wide strips and 250 T for 0.6 μm strips. Since the observed fields were all in the range of 10–20 mT, it follows that the reversal of magnetization directions for CoFe strips does not take place according to the SW model.

Magnetization reversal according to the C model can be determined with eq. 4.6. With the crystalline anisotropy constant K assumed to be negligible, the switch field is given by

$$H_s = -N_\parallel M_s + \frac{8Aq^2}{\mu_0 M_s}\frac{1}{D^2}. \tag{4.11}$$

Using the appropriate parameters for CoFe: $A = 3 \cdot 10^{-11}$ J/m and $M_s = 1.4 \cdot 10^6$ A/m, H_s is calculated and plotted as the solid curve in Fig. 4.35.

All experimental data points are substantially higher than the C curve. However, it could be that a serious error is made in estimating the constants in eq. 4.6. To test the $1/D^2$ dependence, a plot of the data together with eq. 4.6 is shown in Fig. 4.36. The constants K and A are varied to find the best fit. The other parameters are: $N_\perp = 0$, q=1.84, and $M_s = 1.4{\cdot}10^6$ A/m. The parameters found for the best fit are: $A = 4 \cdot 10^{-10}$ J/m, and $K = 5.6 \cdot 10^3$ J/m^3. From Fig. 4.36 it can be concluded that the switching of the CoFe strips is qualitatively following the Curling model, although at present no evidence is available to substantiate the large values required for A and K.

On the basis of micromagnetic simulations (OOMMF), the switch field is simulated using the appropriate material parameters. The particle is approximated as an ellipsoid with a length of 20 μm, and variable width. With OOMMF, the energy minimum is calculated for every step in a specific field range, leading, as an example, to the magnetization curve of Fig. 4.37 for a particle with a width of 1400 nm. From these magnetization curves the switch field is determined for strips of different widths. This leads to the dotted curve in Fig. 4.35. The switch field found with the simulations is higher than the switch field found with the measurements, which, given the uncertainty in the material parameters as well as in the data, is a rather satisfactory agreement.

As mentioned earlier, the models used above are only valid in a specific width range. For widths larger than the single domain diameter D_{SD}, which

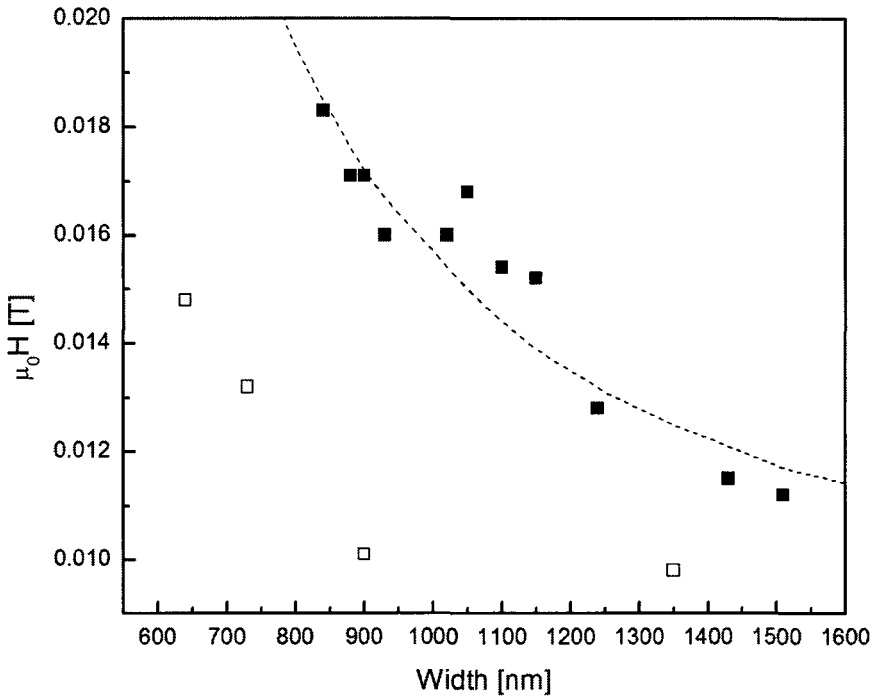

Figure 4.36: *The measurements are fitted with eq. 4.6, where $N_\perp = 0$, q=1.84, and $M_s = 1.4 \cdot 10^6$ A/m. K and A are varied to find the best fit, which results in $A = 4 \cdot 10^{-10}$ J/m, and $K = 5.6 \cdot 10^3$ J/m^3. Only the solid squares are fitted.*

is ≈ 3 μm for Co (see section 4.1.3), the strip is expected to be in a multi-domain state, and switching will occur by domain wall displacement. For widths smaller than D_{SD}, the strip is single domain, and switching occurs by the SW mode or the C mode. The SW mode is dominant for widths smaller than the critical diameter, D_{crit}, which is estimated as $\approx$ 26 nm for Co (see section 4.1.2). For the strips used here ($600 < D < 1500$ nm), magnetization reversal according to the C model should be expected from the large difference in the width of the strips compared to the critical diameter (eq. 4.7) of $\approx$ 26 nm. However, as seen in Fig. 4.34, we have found strong evidence that the switching takes place via domain wall displacement, and moreover, a detailed internal magnetic configuration is observed also suggesting a multi-domain situation. Nucleation of domain walls can decrease the magnetic switch field, but pinning at imperfections in the strip can increase the switch field. The switch field found with micromagnetic simulations is higher than the measured switch field. This is probably due to the fact that the simulations are performed on perfect structures (especially at the corrugated edges), whereas the real strips all have imperfections in the structure, where pinning of domain walls can occur.

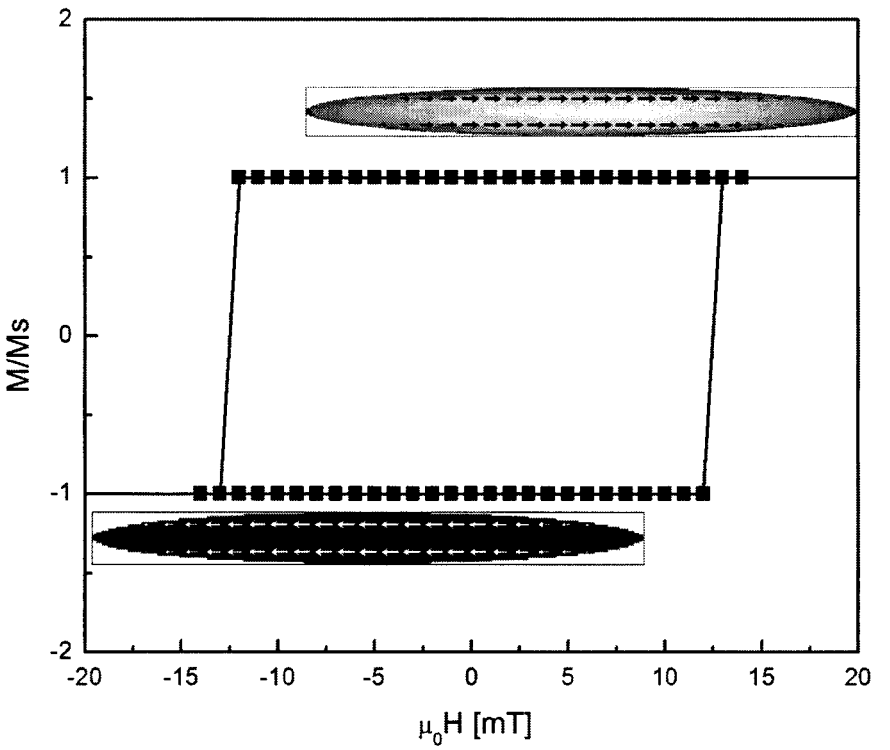

Figure 4.37: *Magnetization curve of a 20 μm long and 1.4 μm wide strip, simulated with OOMMF. The two simulations shown are representing the positive and negative saturation magnetization.*

4.4.4 Conclusions

Magnetic force microscopy is successfully used to visualize the magnetic state of structured CoFe strips. The magnetic switch field of the strips can be determined for individual strips, and it is determined that the switch field depends on the width of the strips. The measurements are compared to different models.

Assuming magnetization reversal by SW, a switch field $\mu_0 H_{sw}$=100 mT for 1.5 μm wide strips is found, which exceeds the measured values by a factor of 10. This indicates that magnetization reversal does not follow the SW model. The curling model has an $1/D^2$ dependence of the switch field according to eq. 4.6. This $1/D^2$ dependence is also found in the measurements (Fig. 4.36). It can be concluded that the switching of the CoFe strips is qualitatively following the Curling model. The results for micromagnetic simulations of the reversal in ellipsoids are in reasonable quantitative agreement with experimental data on CoFe strips. For strips

where the width is approximately 0.5-1.5 μm, the simulation show that the found switching fields are higher than the measurements. However, it should be noted that the internal magnetic structure seen in th MFM images (probably related to defects and irregularities at the sample boundaries) is not included in these simulations, which may in general drastically affect the magnetization reversal. The correspondence of the simulations with the data could therefore be fortuitous.

Chapter 5

Conclusions and outlook

Magnetic force microscopy is a useful tool for observing the magnetic domain structure of structured magnetic samples. The theory behind MFM is presented, and the magnetization of several samples is investigated. A magnetic stage has been designed to perform MFM measurements in the presence of an external applied field up to 120 mT. It is possible to visualize magnetic domains and domain walls of structures with a typical size of 1 μm by MFM and to manipulate them with an external magnetic field. Experiments have been performed on magnetic nanostructured devices to image magnetic properties on a sub-micrometer scale. The results of these investigations are summarized here.

- The magnetization of a data carrier intended for the development of MROM is qualitatively determined. The sample consists of a substrate, structured with bits of 5×1 μm. The full substrate is coated with a continuous magnetic CoFe film. The height of the bits, measured with AFM, is found to be approximately 50 nm. It is shown with MFM that in the remanent state a small magnetic field is present above the bits. A larger scan area reveals an oscillating signal with a period of 7 μm, corresponding to the measured signal measured with an MTJ array. By determining the measured phase shift as a function of the applied field, the magnetic state of individual bits can be determined. A switch field in the range of 0–10 mT is found in agreement with a SQUID measurement performed on the full magnetic layer. The magnetic signal above the bits can be improved by increasing the magnetic stray field emanating from the bits. This can be done by increasing the height of the bits, or deposition of the CoFe layer under oblique angles to prevent the formation of a continuous magnetic layer.

- Structured magnetic multilayers (bits) are investigated for their relevance in the development of MRAM. The bits consists of a substrate with a 5 nm Ta/ 5 nm CoFe/ 10 nm FeMn/ 3.5 nm CoFe (pinned layer)/ 0.9 nm AlOx/ 15 nm CoFe (free layer)/ 5 nm Ta stack. With MFM the top CoFe layer is investigated. At remanence, the magnetic microstructure is determined. MFM proves to be a valuable tool to investigate the local properties of single bits, as they do not always behave like (SQUID) measurements predict. The magnetic state of several bits is changed during scanning by the influence of the stray field of the tip. At applied fields of 30 mT, the magnetization is found to be almost uniform and in the plane of the magnetic layer.

- For spin injection into semiconductors, the magnetic field direction of two ferromagnetic strip-like electrodes needs to be individually controlled. MFM is used to determine the width dependence of the magnetic switch field of these magnetic (CoFe) strips. The switch field of strips with length 20 μm and width between 500–1500 nm is found to be in the range of 10–20 mT, which enables the magnetic control of a spin-injection device by choosing 2 strips of different width. The measurements do not correspond to models describing switching in single domain particles using realistic material parameters. Micromagnetic simulations with OOMMF are made, and show a similar width dependence of the switch field as the measurements. In future studies, the simulations can be improved by using the realistic shape of the strips. To enter the regime of single domain models, the lateral dimensions of the strips should be reduced, or magnetic material with a smaller saturation magnetization should be used.

Bibliography

[1] P. Grünberg, R. Schreiber, Y. Pang, M.B. Brodsky, and H. Sowers. *Layered Magnetic Structures: Evidence for Antiferromagnetic Coupling of Fe Layers across Cr Interlayers.* Phys. Rev. Lett. **57**, 2442 (1986).

[2] S.S.P. Parkin, N. More, and K.P. Roche. *Oscillations in Exchange Coupling and Magnetoresistance in Metallic Superlattice Structures: Co/Ru, Co/Cr, and Fe/Cr.* Phys. Rev. Lett. **64**, 2304 (1990).

[3] M.N. Baibich, J.M. Broto, A. Fert, F. Nguyen Van Dau, F. Petroff, P. Etienne, G. Creuzet, A. Friederich, and J. Chazelas. *Giant Magnetoresistance of (001)Fe/(001)Cr Magnetic Superlattices.* Phys. Rev. Lett. **61**, 2472 (1988).

[4] H. Sato, P.A. Schroeder, J. Slaughter, W.P. Pratt Jr., and W. Abdul-Razzaq. *Galvanometric Properties of Ag/M (M=Fe, Ni, Co) Layered Metallic Films.* Superlattices and Microstructures **4**, 45 (1988).

[5] G. Binasch, P. Grünberg, F. Saurenbach, and W. Zinn. *Enhanced magnetoresistance in layered magnetic structures with antiferromagnetic interlayer exchange.* Phys. Rev. B **39**, 4828 (1988).

[6] J.S. Moodera, L.R. Kinder, T.M. Wong, and R. Meservey. *Large Magnetoresistance at Room Temperature in Ferromagnetic Thin Film Tunnel Junctions.* Phys. Rev. Lett. **74**, 3273 (1995).

[7] T. Miyazaki and N. Tezuka. *Giant magnetic tunneling effect in $Fe/Al_2O_3/Fe$ junction.* J. Magn. Magn. Mater. **139**, L231 (1995).

[8] J. Daughton, J. Brown, E. Chen, R. Beech, A. Pohm, and W. Kude. *Magnetic Field Sensors Using GMR Multilayer.* IEEE Trans. Mag. **30**, 4608 (1994).

[9] C. Tsang, R.E. Fontana, T. Lin, D.E. Heim, V.S. Speriosu, B.A. Gurney, and M.L. Williams. *Design, Fabrication & Testing of Spin-Valve Read Heads for High Density Recording.* IEEE Trans. Mag. **30**, 3801 (1994).

[10] S. Tehrani, B. Engel, J.M. Slaughter, E. Chen, M. DeHerrera, M. Durlam, P. Naji, R. Whig, J. Janesky, and J. Calder. *Recent Developments in Magnetic Tunnel Junction MRAM.* IEEE Trans. Mag. **36**, 2752 (2000).

[11] S. Tehrani, J.M. Slaughter, M. Deherrera, B.N. Engel, N.D. Rizzo, J. Salter, M. Durlam, R.W. Dave, J. Janesky, B. Butcher, K. Smith, and G. Grynkewich. *Magnetoresistive Random Access Memory Using Magnetic Tunnel Junctions.* Proc. IEEE **91**, 703 (2003).

[12] J.Das. *Magnetic Random Access Memories. Technology assessment and tunnel barrier reliability study.* PhD thesis, KU Leuven, (2003).

[13] M.R. Scheinfein, J. Unguris, M.H. Kelley, D.T. Pierce, and R.J. Celotta. *Scanning electron microscopy with polarization analysis (SEMPA).* Rev. Sci. Instrum. **61**, 2501 October (1990).

[14] M. Julliere. *Tunneling between ferromagnetic films.* Phys. Lett. A **54**, 225 (1975).

[15] W. Wulfhekel and J. Kirschner. *Spin-polarized scanning tunneling microscopy on ferromagnets.* Appl. Phys. Lett. **75**, 1944 (1999).

[16] P. Grütter, H.J. Mamin, and D. Rugar. *Magnetic Force Microscopy (MFM).* In "Scanning Tunneling Microscopy II", ed. by R. Wiesendanger and H.-J. Güntherodt, volume 28 of *Springer Series in Surface Science*, pages 151–207. Springer-Verlag, Berlin, (1992).

[17] G. Binnig, H. Rohrer, Ch. Gerber, and E. Weibel. *Surface Studies by Scanning Tunneling Microscopy.* Phys. Rev. Lett. **49**, 57 (1982).

[18] G. Binnig, C.F. Quate, and Ch. Gerber. *Atomic Force Microscope.* Phys. Rev. Lett. **56**, 930 (1986).

[19] Y. Martin, C.C. Williams, and H.K. Wickramasinghe. *Atomic force microscope - force mapping and profiling on a sub 100-Å scale.* J. Appl. Phys. **61**, 4723 (1987).

[20] J.E. Stern, B.D. Terris, H.J. Mamin, and D. Rugar. *Deposition and imaging of localized charge on insulator surfaces using a force microscope.* Appl. Phys. Lett. **53**, 2717 (1988).

[21] B.D. Terris, J.E. Stern, D. Rugar, and H.J. Mamin. *Contact Electrification Using Force Microscopy.* Phys. Rev. Lett. **63**, 2669 (1989).

[22] Y. Martin, D.W. Abraham, and H.K. Wickramasinghe. *High-resolution capacitance measurement and potentiometry by force microscopy.* Appl. Phys. Lett. **52**, 1103 (1988).

[23] E. Meyer and H. Heinzelmann. *Scanning Force Microscopy.* In "Scanning Tunneling Microscopy II", ed. by R. Wiesendanger and H.J. Güntherodt, volume 28 of *Springer Series in Surface Science*, pages 99–149. Springer-Verlag, Berlin, (1992).

[24] S. Porthun, L. Abelmann, and C. Lodder. *Magnetic force microscopy of thin film media for high density magnetic recording.* J. Magn. Magn. Mater. **182**, 238 (1998).

[25] Technische Universiteit Eindhoven. *Natuurkunde praktikum : geavanceerde meetmethoden*, juli 2005 edition, (2005).

[26] E. Meyer, H.J. Hug, and R. Bennewitz. *Scanning Probe Microscopy: The Lab on a Tip.* Springer-Verlag, Berlin, (2004).

[27] H. C. Hamaker. *The London-Van der Waals attraction between spherical particles.* Physica **4**, 1058 (1937).

[28] T.R. Albrecht, P. Grütter, D. Horne, and D. Rugar. *Frequency modulation detection using high-Q cantilevers for enhanced force microscope sensitivity.* J. Appl. Phys. **69**, 668 (1991).

[29] Y. Martin and H.K. Wickramasinghe. *Magnetic imaging by "force microscopy" with 1000 Å resolution.* Appl. Phys. Lett. **50**, 1455 (1987).

[30] J.J. Sáenz, N. Garcia, P. Grütter, E. Meyer, H. Heinzelmann, R. Wiesendanger, L. Rosenthaler, H.R. Hidber, and H.-J. Güntherodt. *Observation of magnetic forces by the atomic force microscope.* J. Appl. Phys. **62**, 4293 (1987).

[31] R. Allenspach, H. Salemink, A. Bishof, and E. Weibel. *Tunneling Experiments Involving Magnetic Tip and Magnetic Sample.* Z. Phys. B **67**, 125 (1987).

[32] Y. Martin, D. Rugar, and H.K. Wickramasinghe. *High-resolution magnetic imaging of domains in TbFe by force microscopy.* Appl. Phys. Lett. **52**, 244 (1988).

[33] J.D. Jackson. *Classical Electrodynamics.* John Wiley, New York, (1999).

[34] U. Hartmann. *Magnetic force microscopy.* Ann. Rev. Mater. Sci. **29**, 53 (1999).

[35] D. Rugar, H.J. Mamin, P. Guethner, S.E. Lambert, J.E. Stern, I. McFadyen, and T. Yogi. *Magnetic force microscopy: General principles and application to longitudinal recording media.* J. Appl. Phys. **68**, 1169 (1990).

[36] J.C. Mallison. *On the Properties of Two-Dimensional Dipoles and Magnetized Bodies.* IEEE Trans. Mag. **17**, 2453 (1981).

[37] I.R. Beardsley. *Reconstruction of the Magnetization in a Thin Film by a Combination of Lorentz Microscopy and External Field Measurements.* IEEE Trans. Mag. **25**, 671 (1989).

[38] C.V. Heer. *Statistical mechanics, kinetic theory and stochastic processes.* Academic Press, London, (1972).

[39] T.R. Albrecht and C.F. Quate. *Atomic resolution imaging of a nonconductor by atomic force microscopy.* J. Appl. Phys. **62**, 2599 (1987).

[40] O. Marti, B. Drake, and P.K. Hansma. *Atomic force microscopy of liquid-covered surfaces: Atomic resolution images.* Appl. Phys. Lett. **51**, 484 (1987).

[41] C. Schönenberger and S.F. Alvarado. *Understanding magnetic force microscopy.* Z. Phys. B **80**, 373 (1990).

[42] P.C.D. Hobbs, D.W. Abraham, and H.K. Wickramasinghe. *Magnetic force microscopy with 25 nm resolution.* Appl. Phys. Lett. **55**, 2357 (1989).

[43] P. Grütter, Th. Jung, H. Heinzelmann, A. Wadas, E. Meyerand H.-R. Hidber, and H.-J. Güntherodt. *10-nm resolution by magnetic force microscopy on FeNdB.* J. Appl. Phys. **67**, 1437 (1990).

[44] C.Chen. *Introduction to Scanning Tunneling Microscopy.* Oxford University Press, New York, (1993).

[45] R.Wiesendanger and H.-J.Güntherodt. *Scanning Tunneling Microscopy III: Theory of STM and Related Scanning Probe Methods.* Springer-Verlag, Berlin, (1993).

[46] D.Bonnel. *Scanning Probe Microscopy and Spectroscopy: Theory, Techniques and Applications.* John Wiley, New York, (2000).

[47] V.L. Mironov. *Fundamentals of the scanning probe microscopy.* The Russian Academy of Sciences Institute of Physics of Microstructures, (2004).

[48] P. Grütter, D. Rugar, H.J. Mamin, G. Castillo, C.-J. Lin, I.R. McFadyen, R.M. Valletta, O. Wolter, T. Bayer, and J. Greschner. *Magnetic force microscopy With batch-fabricated force sensors.* J. Appl. Phys. **69**, 5883 (1998).

[49] P. Grütter, D. Rugar, H.J. Mamin, G. Castillo, S.E. Lambert, C.-J. Lin, R.M. Valletta, O. Wolter, T. Bayer, and J. Greschner. *Batch fabricated sensors for magnetic force microscopy.* Appl. Phys. Lett. **57**, 1820 (1990).

[50] K. Sueoka, K. Okuda, N. Matsubara, and F. Sai. *Study of tip magnetization behavior in magnetic force microscope.* J. Vac. Sci. Technol. B. **9**, 1313 (1991).

[51] NT-MDT. *Solver p47H Reference Manual,* version 845 edition.

[52] E.H. Frei, S. Shtrikman, and D. Treves. *Critical Size and Nucleation Field of Ideal Ferromagnetic Particles.* Phys. Rev. **106**, 446 (1957).

[53] E.C. Stoner and E.P. Wohlfarth. *A Mechanism of Magnetic Hysteresis in Heterogeneous Alloys.* Philos. Trans. R. Soc. London **240**, 599 (1948).

[54] H. Kronmüller and M. Fähnle. *Micromagnetism and the microstructure of ferromagnetic solids.* Cambridge University Press, (2003).

[55] A. Aharoni. *Perfect and imperfect particles.* IEEE Trans. Mag. **22**, 2453 (1986).

[56] J. Yu, U. Rudiger, A.D. Kent, L. Thomas, and S.S.P. Parkin. *Micromagnetism and magnetization reversal of micron-scale (110) Fe thin-film magnetic elements.* Phys. Rev. B **60**, 7352 (1999).

[57] J. Nitta, T. Schapers, H.B. Heersche, T. Koga, Y. Sato, and H. Takayanagi. *Investigation of Ferromagnetic Microstructures by Local Hall Effect and Magnetic Force Microscopy.* Jpn. J. Appl. Phys. **41**, 2497 (2002).

[58] W.P.E.M. Op t Root. Magnetic read only memory. Master's thesis, Eindhoven University of Technology, (2005).

[59] W.P.E.M. Op t Root, H.J.M. Swagten, F.J. Jedema, and A.E.T. Kuiper. *Magnetic read-only memory with removable medium.* Appl. Phys. Lett. **87**, 203501 (2005).

[60] S. Tehrani, E. Chen, M. Durlam, M. DeHerrera, J.M. Slaughter, J. Shi, and G. Kerszykowski. *High density submicron magnetoresistive random access memory.* J. Appl. Phys. **85**, 5822 (1999).

[61] S. Datta and B. Das. *Electronic analog of the electro-optic modulator.* Appl. Phys. Lett. **56**, 665 (1990).

[62] S. Gardelis, C.G. Smith, C.H.W. Barnes, E.H. Linfield, and D.A. Ritchie. *Spin-valve effects in a semiconductor field-effect transistor: A spintronic device.* Phys. Rev. B **60**, 7764 (1999).

[63] G.A. Prinz. *Magnetoelectronics.* Science **282**, 1660 (1998).

[64] V.F. Motsnyi, J. De Boeck, J. Das, W. Van Roy, G. Borghs, E. Goovaerts, and V.I. Safarov. *Electrical spin injection in a ferromagnet/tunnel barrier/semiconductor heterostructure.* Appl. Phys. Lett. **81**, 265 (2002).

[65] J.J.H.M. Schoonus. Towards all electrical spin injection and detection in GaAs in a lateral geometry. Master's thesis, Eindhoven University of Technology, (2004).

[66] K.C. Kuiper. Coercive fields of shape anisotropy dominated CoFe strips. Traineeship Report, Eindhoven University of Technology, (2006).

Appendix A

Demagnetization Factors

The magnetic field inside a magnetized sample tends to demagnetize the sample and is known as the demagnetizing field $\boldsymbol{H}_d$. In general the demagnetizing field acts opposite to the magnetization $\boldsymbol{M}$ which creates it:

$$\boldsymbol{H}_d = -N_d \boldsymbol{M}, \tag{A.1}$$

where N_d is the demagnetizing factor, and depends strongly on the geometry of the sample, but can only be calculated exactly for an ellipsoid where the magnetization is uniform throughout the sample. For a general ellipsoid with semi-axis $c \geq b \geq a$, the demagnetization factors are N_c, N_b, and N_a, respectively. The demagnetization factors are related by:

$$N_a + N_b + N_c = 1. \tag{A.2}$$

The demagnetization factors are given for three different ellipsoids:

- Prolate sphereoid ($c > a = b$). The aspect ratio m, is defined as $m = c/a$.

$$N_{a,b} = N_\perp = \frac{m}{2(m^2-1)} \left(m - \frac{\ln\left(\frac{m+\sqrt{m^2-1}}{m-\sqrt{m^2-1}}\right)}{2\sqrt{m^2-1}} \right), \tag{A.3}$$

$$N_c = N_\parallel = \frac{1}{m^2-1} \left(\frac{m \ln\left(\frac{m+\sqrt{m^2-1}}{m-\sqrt{m^2-1}}\right)}{2\sqrt{m^2-1}} - 1 \right). \tag{A.4}$$

- Slender ellipsoid ($c >> a > b$).

$$N_a = \frac{b}{a+b} - \frac{ab}{2c^2}\ln\left(\frac{4c}{a+b}\right) + \frac{ab(3a+b)}{4c^2(a+b)}, \quad \text{(A.5)}$$

$$N_b = \frac{a}{a+b} - \frac{ab}{2c^2}\ln\left(\frac{4c}{a+b}\right) + \frac{ab(a+3b)}{4c^2(a+b)}, \quad \text{(A.6)}$$

$$N_c = \frac{ab}{c^2}\left(\ln\left(\frac{4c}{a+b}\right) - 1\right). \quad \text{(A.7)}$$

- Oblate sphereoid ($c = b > a$). The aspect ratio m, is defined as $m = c/a$.

$$N_a = \frac{m^2}{m^2-1}\left(1 - \frac{\arcsin\left(\frac{\sqrt{m^2-1}}{m}\right)}{\sqrt{m^2-1}}\right), \quad \text{(A.8)}$$

$$N_{b,c} = \frac{1}{2(m^2-1)}\left(\frac{m^2\arcsin\left(\frac{\sqrt{m^2-1}}{m}\right)}{\sqrt{m^2-1}} - 1\right). \quad \text{(A.9)}$$

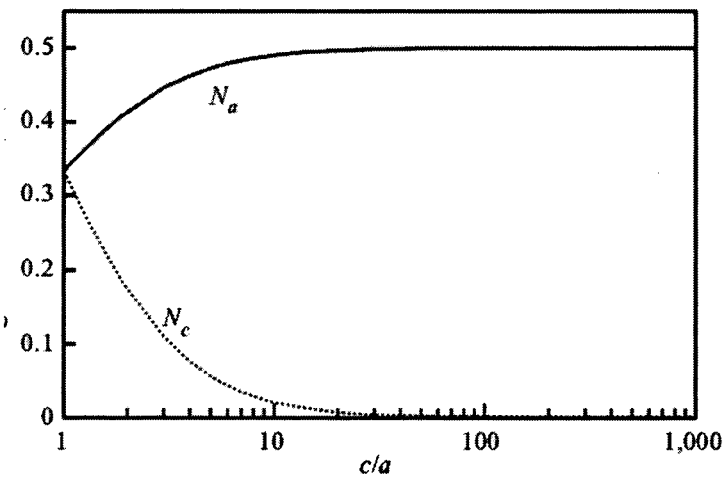

Figure A.1: *Calculated dependence of the demagnetization factors of a prolate spheroid on its aspect ratio c/a. For $c/a > 10$, $N_a \approx 0.5$.*

Figure A.1 shows the demagnetization factors of a prolate spheroid on its aspect ratio (c/a). In the case of a high aspect ratio, the demagnetization factor along the hard axis is equal to 0.5, and the demagnetization factor along the easy axis is 0.

Appendix B

MFM Measurements on MROM sample

All the images in the series explained in section MROM are presented here.

In Fig. B.1, approximately 4 bits can be seen, indicated by the topography. An external magnetic field was applied parallel to the short direction of the bits, the magnitude of the field (in mT) is indicated below the images. The magnetization of the bits is perpendicular to the long axis, even in the situation at zero applied field.

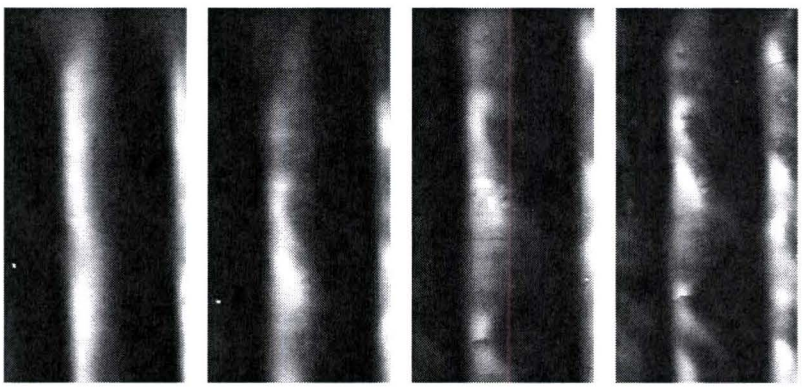

(30) **(10)** **(8)** **(6)**

Figure B.1: *Continued at the next page.*

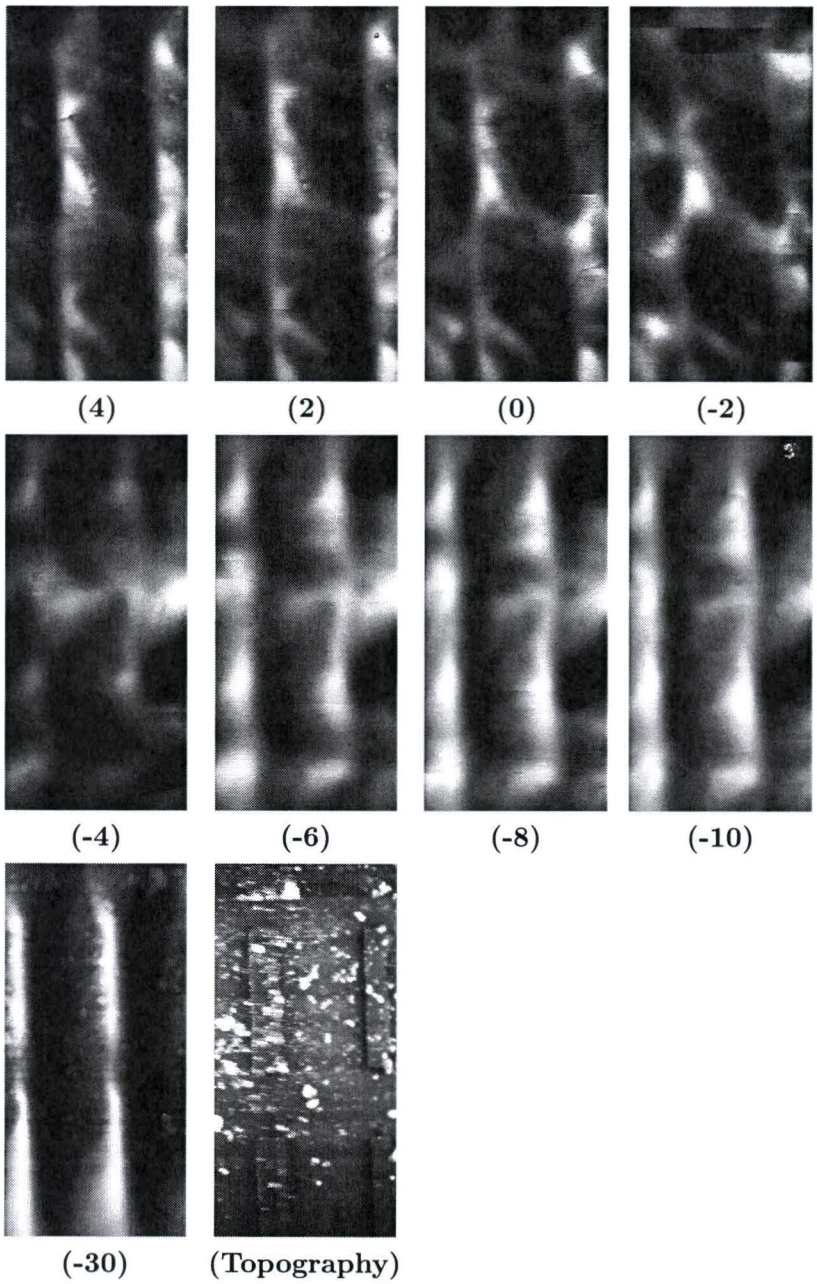

Figure B.1: *MFM with the field applied in the short direction of the bits. The size of the images is 6.5× 13 μm.*

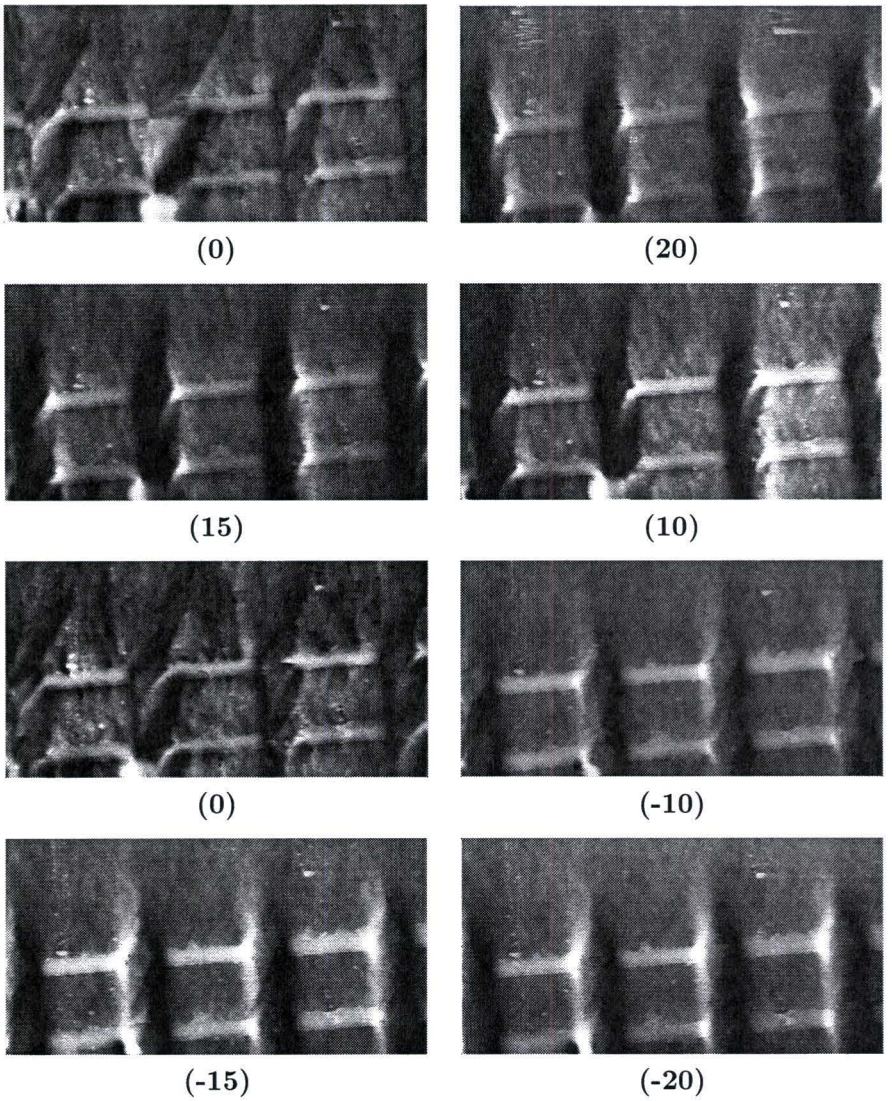

Figure B.2: *MFM Measurements of a structured CoFe sample. The external field is applied in the long direction of the bits. All images are 24×12 μm.*

Fig. B.2 shows 6 bits where the applied field is parallel to the long direction of the bits, the magnitude of the applied field (in mT) is indicated below the images. The magnetization of the bits is uniform in-plane and parallel to the long axis, except for the situation at zero applied field, where almost no signal can be seen on the bits.

Appendix C

AFM/MFM User Guide

In this section, a guide is given to perform AFM or MFM measurements. In this guide step by step instructions are presented. To do the measurements the user simply has to follow these steps. At the end of this appendix a quick guide is given for the advanced AFM/MFM user.

C.1 Initial preparations

Before measurements can start, the microscope and sample have to be prepared. These preparations apply to all measuring modes. The sample preparation, cantilever installation and the general setup is described.

C.1.1 Sample preparation

Choose a sampleholder (figure C.1a) suitable for your measurements and attach it to the holder stage. Depending on the measurement you are preparing you can choose between different sizes and materials for the sample holder. To mount the sample on the sample holder a screw or glue can be used. For measurements in the presence of an external magnetic field, place the appropriate coils and yoke on the holder stage, and connect the wires. After that, place the holder stage onto the sample approach module (figure C.1b).

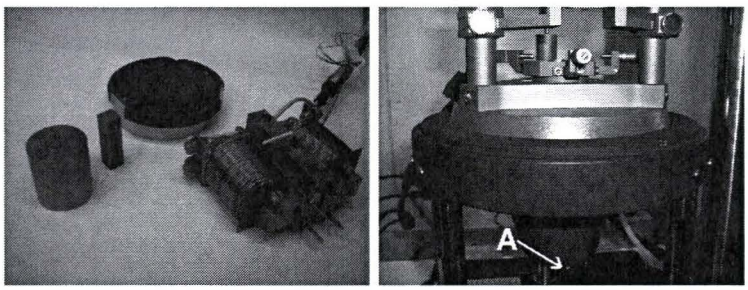

Figure C.1: *a) Different sample holders, the holder stage and a magnetic coil/yoke setup. b) The sample approach module, The 'manual approach knob' is indicated by 'A'.*

C.1.2 Cantilever installation

Put the scanner head upside down on the table and set the switch on the left hand side of the head in the close position (indicated by the arrow in figure C.2) to install a cantilever in the scanner head. The spring holding the cantilever is released. If a cantilever is present in the head, make sure you have a storage container nearby, take a pair of tweezers and remove the cantilever. Select a cantilever suited for your measurements (Contact, Non-contact or Magnetic). Place the cantilever on the right side of the working area (dotted line in the right zoom of figure C.2), and shift it under the spring. With the cantilever in the correct place, set the switch on the left hand side back in the open position.

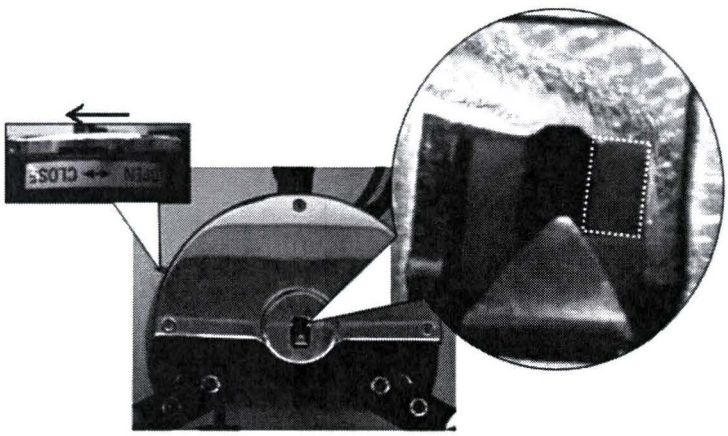

Figure C.2: *The scanner head, on the left the switch, the arrow indicates the direction in which the spring is released. On the right side a zoom of the cantilever, the working area is indicated by the dotted region.*

When a magnetic cantilever is installed, hold a small magnet just above the cantilever to magnetize it.

Place the scanner head back on the approach module, but make sure the cantilever does not touch the sample. Turn the 'manual approach knob' (A in figure C.1) under the sample approach module counterclockwise, if there is not enough space between the sample and the cantilever.

C.1.3 General setup

Turn on the anti-vibration table, the camera and the TV. Log in on the computer and start the software with the 'smena' icon on the desktop. Turn on the electronics with the red switch on the front of the unit. Move the camera above the mirror so that the end of the cantilever can be seen on the TV.

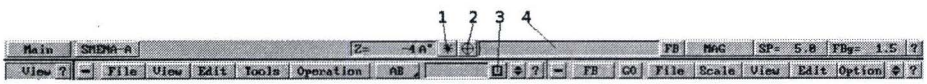

Figure C.3: *The top row of buttons in the smena program. 1: the laser on/off button. 2: the photodiode button. 3: SPM control block diagram. 4: piëzo-extension indicator bar.*

Turn on the laser of the scanner head by pressing button 1 in the top row buttons of the software (figure C.3). View the photodiode signal by pressing button 2. With the two 'laser' knobs on top of the head (figure C.4) move the laser so it is pointing on the end of the cantilever, as seen on the TV screen, and maximize the 'LASER' signal from the photodiode. Preferably the laser signal should be larger then 10. Bear in mind that the laser has to stay at the end of the cantilever, if it is turned too far from the end the laser signal will increase, but the measured deflection will decrease. With the two 'photodiode' knobs center the signal on the photodiode. If the photodiode signal is maximized and centered, close the window by pressing the 'ESC' key on the keyboard.

Turn the micrometer screws on the sample approach stage to position the sample under the cantilever. Depending on the sample and the reflectivity, the sample position can be seen on the monitor if the camera is positioned above the mirror. Turn the manual approach knob clockwise, while observing the sample-cantilever distance by eye, until

the distance from the sample to the cantilever is about 1 mm.

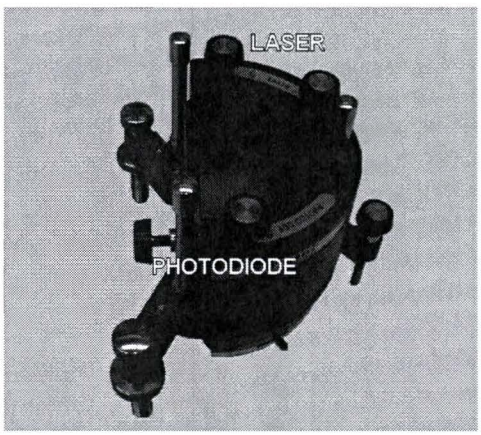

Figure C.4: *The top of the head. The top two knobs are the laser alignment knobs and the bottom two are the photodiode adjustments knobs.*

C.2 Measuring modes

Make sure the initial preparations from paragraph C.1 are done. This means that the program must be running and the electronics are turned on, the cantilever and sample are installed, the preliminary approach is performed and the laser and photodiode adjustment are completed. There are two basic measurement modes: Contact Atomic Force Microscopy (Contact mode) and Semi Contact Atomic Force Microscopy (Tapping mode). Contact mode is also known as DC-mode, because the cantilever is not vibrating in contrast to tapping mode, which is known as AC-mode. Generally tapping mode is used. A special case is Magnetic Force Microscopy (MFM-mode). MFM-mode will not be treated separately, but included in contact and semi contact mode.

C.2.1 Contact Atomic Force Microscopy

In Contact mode the tip is in constant contact with the surface so there is a chance of damaging soft samples. Contact mode is the basis of other scanning techniques where the tip is in contact with the sample.

Preparation of 'SPM Control block diagram'

To set the parameters used during scanning open the 'SPM control block diagram' by pressing button 3 in figure C.3. The 'SPM control block diagram' is divided into three sections, the top section displays the scan-settings, the middle section the lock-in amplifier settings and the bottom section is a small oscilloscope (figure C.5).

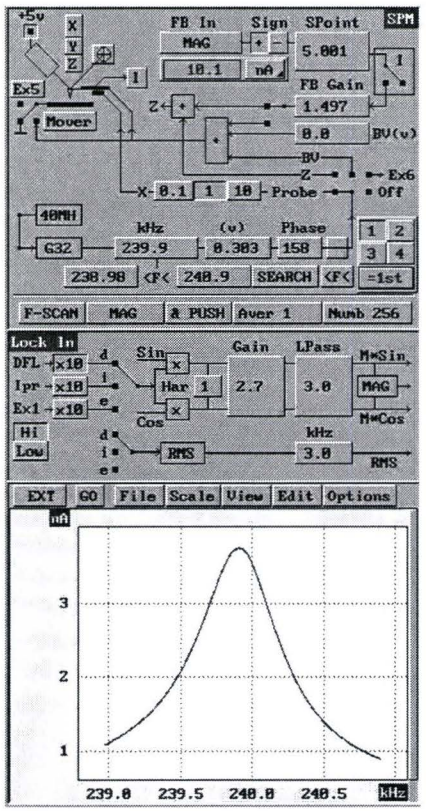

Figure C.5: *SPM control block diagram. The diagram is divided into 3 parts. In the top part the scan settings are displayed, the middle part displays the lock-in amplifier settings and the bottom part is an oscilloscope.*

In the top section apply the DFL signal to 'FB in' by clicking on the 'MAG' button under 'FB in' and selecting 'DFL'. To set the initial DFL signal to 1.5 nA turn the vertical adjustment knob of the photodiode (figure C.4). Set 'Spoint' to zero by clicking on the value and adjusting the slider and make sure the 'FB gain' value is larger than 1.

MFM: In order to do DC Magnetic Force Microscopy no additional settings are required. When all these settings have been applied continue with section 'C.3 Approaching the sample' on page 113.

C.2.2 Semi Contact Atomic Force Microscopy

Operation in Semi contact or Tapping mode is the most commonly used mode and is the basis of other techniques using modulation modes. In Tapping mode the cantilever is oscillated at the resonant frequency. The tip end is just a brief moment of the vibration period in contact with the surface, in this way there is less chance of damaging the sample during scanning.

Preparation of SPM Control block diagram

To set the parameters used during scanning open the SPM control block diagram by pressing button 3 in figure C.3. The SPM control block diagram is divided into three sections, the scan-settings in the top section, the lock-in amplifier settings in the middle section and a small oscilloscope in the bottom section. All settings in this diagram can be changed by pressing the button or the value and shifting the slider to the correct value, or by selecting the correct signal.

In the top section make sure the 'FB in' signal is set to 'MAG' and the feedback is turned off (Open circuit 'I'). The lock-in signal must be 'd' as indicated in figure C.5. The preliminary amplifier input must be set to 'high' or 'low' frequency depending on the used cantilever. High frequency is used for frequencies higher than 80 kHz.

Set the cantilever resonant frequency by pressing the 'search' button in the top section, the resulting signal-frequency curve is shown on the oscilloscope and the working frequency will be set to the frequency with the maximum signal. If there is now resonant frequency found, check the preliminary amplifier input for 'high' or 'low' frequency input. If the signal-frequency curve is broadened (no nice gauss curve), the voltage is probably too high, lower it by reducing the voltage 'v' or by lowering the multiplication value (0.1,1,10). The initial value of the 'MAG' signal should be around 10, if the 'MAG' signal is too low increase the 'gain' of the lock-in amplifier until the desired value is reached.

In the top section the initial 'SPoint' value should be set at approximately 50% of the initial 'MAG' value. Make sure the initial 'FB gain' value is larger than 1.

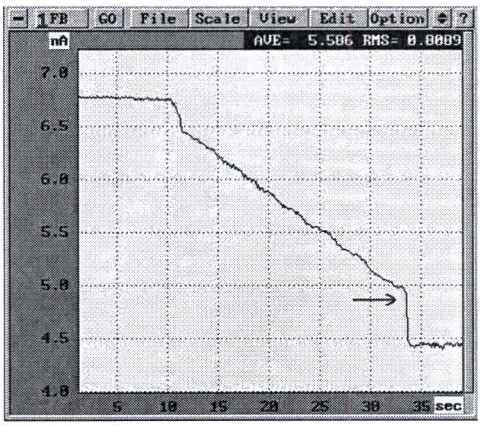

Figure C.6: *The top oscilloscope. The displayed signal is a typical approach signal. Setpoint should be set to approximately the level of the arrow. Button 1 can be used to changed the displayed channel.*

MFM: To do AC Magnetic force microscopy, the phase signal has to be set to 90°. Apply the channel B to the bottom right oscilloscope, figure C.6, by pressing button 1 and selecting '->B', and pressing the 'GO' button. Go back to the SPM Control Block Diagram, and change the 'Phase' value so the scope readout is approximately 90°.

C.3 Approaching the sample

After all the parameters for the used measuring mode are set, the approach of the sample to the tip can be performed. The method is the same for all measuring modes.

Make sure the 'FB' signal is displayed on the top right oscilloscope, figure C.6. If not change the signal by pressing button 1 and select the 'FB' signal. Pressing the GO button will start the oscilloscope. Using the mouse left button (and the shift key) will change the axis dimensions by moving the mouse.

Press the 'mover' button located in the top left corner of the SPM control block diagram, to open the approach window, alternatively press the 'Apr' button in the quick access toolbar on the left of the screen. Move the approach window off the oscilloscopes or the scope will not display a signal. Make sure the fine button is pressed on the 'Mover' or 'Probe' tab. Put the 'Landing' rate on 19 (contact mode:18)

by pressing the 'Rate 20' button. Pressing the Landing button will

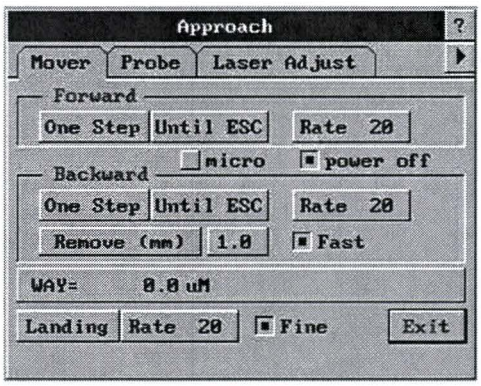

Figure C.7: *The approach window. Landing will start the automatic approach procedure. Forward moves the sample closer to the tip, and backward will remove the sample from the tip*

start the automatic approach to the sample. The automatic approach is ended with an 'ok' signal. The indicator bar at the top of the screen (4 in figure C.3) should be approximately half extended. In the rare case that the indicator bar is fully extended or retracted you have to manually adjust this. See the manual [51] for more information. In Tapping mode you can check the correct approach by increasing the FB gain until generation starts as in figure C.8. The correct FB gain value should be half of this. If no generation occurs the tip is not reaching the sample.

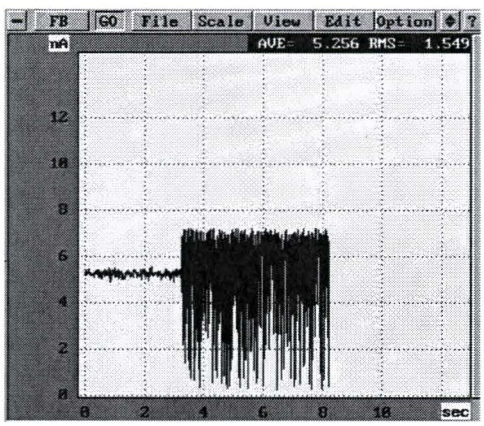

Figure C.8: *A scope window. At three seconds generation starts. Make sure to measure without generation.*

C.4 Scanning parameters and scanning

After the approach procedure is completed, scanning can begin. The settings for the scan speed, scan size and scan direction have to be set, and the signal to be measured has to be selected. If MFM is used, split the SPM window in two by pressing the '◀▶' button in the left bottom of the screen.

C.4.1 Scan settings

To change the settings used during scanning, open the Scanning parameters control window by pressing the folder button in the quick access menu on the left under 'Scan', that is the one just under the *red* 'RUN' button.

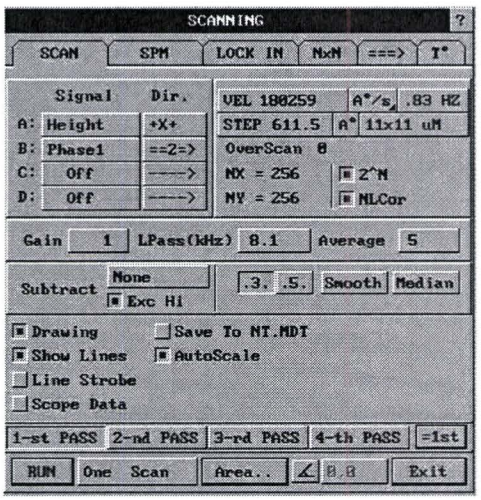

Figure C.9: *The scanning window. The scan tab displays the scanning parameters. The spm tab displays the top part of the spm control block diagram and the lock in tab the middle part. The ===> tab contains settings for the second pass scan.*

In the tab 'SCAN' make sure the signal 'A' is set to 'Height' and choose the scanning direction:

`[+Y+]` : Quick scan upward, Slow scan from left to right,
`[+X+]` : Quick scan from left to right, Slow scan upward,
`[-Y+]` : Quick scan downward, Slow scan from left to right,

[-X+] : Quick scan from right to left, Slow scan upward,
[+Y-] : Quick scan upward, Slow scan from right to left,
[+X-] : Quick scan from left to right, Slow scan downward,
[-Y-] : Quick scan downward, Slow scan from right to left,
[-X-] : Quick scan from right to left, Slow scan downward.

To do DC MFM, set the signal of channel B to 'DFL' and to do AC MFM set the signal of channel B to 'Phase1'. Set the direction of channel B to ==2=>. Put channel B in the 'off' position when performing AFM. Put channels C and D in the 'off' position. Select the number of scan points per scan line (i.e 256 or 512) and change the scan size by changing the 'step' value. If the height of the sample is unknown begin with a small scan size and gradually make it bigger. Select the velocity 'VEL', so that the frequency is about 1Hz with a scan size of approximately 5μm. Set the 'Exc Hi' button in the on position.

To do MFM select the '2-nd PASS' button and then press '=1st'. Change to the ===> tab and set ΔZ to 2000. In the 'SPM' tab disable the feedback by opening the 'I' circuit. Go back to the '1-st PASS' and change to the 'SCAN' tab.

C.4.2 Scanning

To start scanning, press the Run button on the bottom of the Scanning parameters control window. During scanning the velocity, FBgain, Setpoint and the scan size area can be adjusted. Increasing the FBgain can result in better images because the feedback can better track the system, but too high FBgain can cause the system to become unstable and generate noise and thus distorted images. In AC mode, decreasing the Setpoint will cause the tip to tap harder on the sample, but a too high Setpoint will make the tip loose contact with the surface. In DC mode, lowering the Setpoint will decrease the force on the sample.

The mouse is not working during scanning but with the cursor left and right keys highlight the appropriate button and with the up and down keys change the value, or use the enter key to change the scan area, restart the scan from the beginning or pause at the current line (this line will be scanned until you press pause again). The selected channel output shown on the scope can be changed by switching between channel A,B,C,D. The 'SUBPL-1' button calculates the tilt of

the sample and subtracts this from the scanning area, this uses quite some calculating power and can result in image distortion, which cannot be undone, so use it at your own risk. 'redraw' and 'gamma' can be used if the image colors are out of range.

C.5 Saving Data and shutting down the program

After all the scanning is done it is time to save your measurements and shutdown the equipment. First remove the tip from the sample by opening the approach window and the 'Mover' tab. Before pressing 'remove' set the remove distance to at least 1mm. To save your data, go to the File menu and select 'Save,enter the correct name and path and press enter. To save images of your measurements choose File, Export to, PCX/BMP. In the opened window you can change the type of the image. You can choose to save only the current SPM window, the entire window or a user defined region.

Shutdown the program by disabling the feedback (press the FB button in the top row in figure C.3) and turn off the laser with button 1 in figure C.3. Turn off the electronics (Red switch) and exit the program by selecting Main, Exit.
PROGRAM BUG: After exiting the software you are stuck with a blank screen with only a mouse cursor, press ALT-TAB to switch to windows and close the program manually.

Turn off the rest of the equipment like the TV, camera, anti-vibration table and everything else used. Don't forget to update the AFM/MFM logbook before you leave.

C.6 A quick guide

A quick guide, for the more experienced AFM users, is presented. The steps below are to be followed in order to do the measurements.

- Choose a sample holder, fix the sample on it and put it on the sample approach stage.
- If necessary, place the appropriate coils and yoke on the holder stage, and connect the wires.
- Install the right cantilever and if it is a magnetic cantilever, magnetize it.
- Start the software, turn on the anti-vibration table, the camera, TV and electronics.
- Maximize laser signal and align the photodiode.
- Align the sample under the cantilever.
- Reduce the distance from the sample to the cantilever to about 1 mm.
- Open the SPM control block diagram.
- *Contact Mode:* Apply the DFL signal to the FB input, set the initial DFL signal to 1.5 nA set the setpoint to zero. Make sure the FB gain value is larger than 1.
- *Tapping Mode:* Make sure the Mag signal is applied to the FB input, set the working frequency and set the setpoint to 50% of the MAG value. Make sure the FB gain value is larger than 1.
- Open the Scanning parameters control window and make sure the signal A is set to Height. Choose the scanning direction and turn off channel B,C,D.
- Select the scan size and the velocity.
- *MFM:* Set channel B to DFL or Phase1 and Direction to ==2=>. Select the '2-nd PASS' button and then press '=1st'. Set ΔZ to 2000 and disable the feedback. Select the '1-st PASS' button and go back to the 'SCAN' tab.
- Press 'Run' to start scanning.
- Optimize the scanning parameters.
- After scanning, remove the tip from the sample.
- Save and export your data and images.
- Disable the feedback, turn off the laser and electronics and exit the program.
- Turn off the TV, camera and anti-vibration table
- Update the AFM/MFM logbook.